Faculty of Science and Engineering

School of Civil and Mechanical Engineering

First-Principles Study on the Mechanical Properties of Lithiated Sn Anode Materials for Li-Ion Batteries

Panpan Zhang

This thesis is presented for the Degree of

Doctor of Philosophy

of

Curtin University

June 2019

Declaration

To the best of my knowledge and belief this thesis contains no material previously published by any other person except where due acknowledgement has been made. This thesis contains no material which has been accepted for the award of any other degree or diploma in any university.

Signature: _Panpan Zhang_ (Panpan Zhang)

Date: June, 2019

Acknowledgements

Time flies, and in a twinkling of an eye, my doctoral study is coming to an end. Looking back over four years, I would like to express my sincere gratitude to my two mentors.

First, I would like to express my heartiest gratitude to my principal supervisor, A/Prof. Chunsheng Lu. A/Prof. Lu is a gracious, knowledgeable, and illuminative mentor. He always shows excitement and encouragement for discussion with me on my research and confusions. To tell me some trivial knowledge, he always looks up books to let me see. He is the most meticulous scholar I have ever met. He always guided and helped me revise my papers several times. His rigorous attitude on research has a great impact on me. In my research career, A/Prof. Lu sets the model and target for me. In my work and life, A/Prof. Lu gave me a lot of concern. Many times, when I encountered problems, I was not comprehensive enough to consider the problems, he always gave timely reminds and provided some advice. Most importantly, I am grateful to A/Prof. Lu for his help, which gave me the opportunity to study in Australia. During the period in Australia, my vision and thinking have been greatly improved. This study experience will have a profound impact on my future life.

Second, I wish to express my deep gratitude to my co-supervisor Prof. Zengsheng Ma. In my research, from the topic of the thesis to the calculations, the revision of papers and the final revision of the thesis, he has given a lot of valuable guidance. Prof. Ma is quick in thinking, humorous in character and easy-going with others. He is a good teacher and friend of our students. In the past few years, Prof. Ma has also given me a lot of care and help in my life, I would like to express my heartfelt thanks to him.

At the same time, I am grateful to Prof. Changqing Sun, Prof. Yan Wang, A/Prof. Yongli Huang, Dr. Weixin Lei, Dr. Wenjuan, Dr. Yonghui Liu, Dr. Maolin Bo, for all the kind help and suggestions for my research and career.

Abstract

Li-ion batteries are widely used in portable electronic gadgets, electric vehicles, aerospace and other fields because of their high capacities, excellent cycle performance and little environmental pollution. With the rapid advance of consumer electronic products and new energy vehicles, the current technology cannot meet the increasing energy demand. Therefore, the development of high-capacity and fast charge-discharge batteries has become the focus of scientific research. Tin (Sn) with high theoretical capacity makes it a promising anode material for Li-ion batteries. However, Sn experiences huge volume deformation during lithiation and delithiation, which results in cracking and disintegration of active materials, exfoliation of active materials from current collectors, and repeated formation and fracture of the solid electrolyte membrane. This directly leads to capacity attenuation and the decay of cycle performance.

To deeply understand the macroscopic failure behaviour of Sn anode materials and further make an optimization to electrode materials, it is imperative to investigate the evolution of mechanical properties upon lithiation. However, it is difficult to measure the variation of mechanical properties by using experimental methods, the reasons are that (1) the Li_xSn phases and solid electrolyte film formed during lithiation are metastable phases and they can easily react with oxygen and water when they are exposed in the air. Therefore, there are high requirements for the preparation of samples, experimental operations and equipment; (2) experimental results are easily affected by structures of electrode materials (such as, composite and thin film electrodes, different porosities, shapes and sizes of active particles) and humidity (such as, liquid and solid electrolyte). These make electrode materials show varied lithiation kinetics (e.g. different Li-ion diffusion rate), volume deformation and stress evolution, which directly results in marked variations of experimental results.

Considering the difficulty of experimental measurement, by using first-principles

calculation, this thesis systematically investigates the evolution of mechanical properties of active materials and interfacial mechanical properties of electrode-collector interfaces during the charge and discharge processes. The micromechanical failure mechanism of Sn anodes is given. Based on the obtained interface failure mechanism, we further perform optimization to interface properties of electrode-collector interface by using dopants. The main research contents of this thesis are as follows:

(1) on the evolution of mechanical properties (such as bulk, shear and Young's moduli, Poisson's ratio, brittleness and ductility, anisotropy and ideal tensile strength) of Sn anodes during lithiation. Based on chemical bonding analysis, the microphysical mechanism of the change of mechanical properties during lithiation is provided. It is shown that the bulk moduli of $Li_x Sn$ alloys decrease almost linearly with Li content. While the shear and Young's moduli, Poisson's ratios and ideal tensile strengths of alloys fluctuate during the lithiation processes. The softened bulk moduli, large anisotropy and brittleness of alloys at high Li content make the surface of electrode materials prone to microcracks at the late stage of lithiation. Furthermore, due to large differences in crystal structures and mechanical properties of alloy phases during lithiation, high mismatch-induced internal stress is created in the lattices which would lead to microcracks and voids in electrode materials.

(2) based on the study of mechanical properties of active materials, the effect of lithiation on interfacial mechanical properties of electrode-collector is further explored. According to the surface energy tests of alloys and lattice mismatches between alloys and the current collector, stable electrode-collector interfaces are established. Then, the effects of lithiation on the interface strength are studied. Combining the analysis of interfacial chemical bonds, the microscale mechanism of interface failure is given. The results show that upon lithiation, the work of separation (W_{sep}) decreases from 1.59 J m^{-2} before lithiation to 0.45 J m^{-2} at the Li content of 0.78, showing a reduction of about 70%. Besides, the interfacial failure behaviour of electrode-collector interface

is unravelled by using tensile simulation. Finally, based on first-principles calculations and linear elastic fracture mechanics, there is a relationship between the critical core and shell sizes and the state of charge for determining fracture and debonding of a Sn−Cu hollow core-shell structure.

(3) on the influence of Cu_xSn alloys on interfacial mechanical properties of electrode-collector interface. The focus of this research is the influence of Cu_xSn alloys on the interface strength, interfacial chemical bonds and stress-strain behaviour of electrode-collector interface. The results show that Cu_xSn alloys can improve the interface strength of electrode-collector interface. The W_{sep} of Cu_6Sn_5/Cu and Cu_3Sn/Cu interfaces are 1.73 and 1.74 J m^{-2}, respectively, which are about 9% higher than that of Sn/Cu interface. In addition, Cu_xSn alloys enhance the deformation resistance of electrode materials at large strain. The fracture strain of Li_2CuSn/Cu interface is much larger than that (0.16) of LiSn/Cu interface. The ductility of Cu_xSn alloys makes Cu_xSn/Cu interface display ductile fracture, which is different from the brittle fracture of Li_xSn/Cu interface. Through comparing the interfacial mechanical properties of the Li_xSn/Cu and Cu_xSn/Cu interfaces, the mechanical properties of the real electrode-collector interface are given.

(4) based on the obtained interfacial failure mechanism, Co doping has been used to improve interfacial properties of Sn electrode-collector. The effects of different interfacial doping sites on the structures, thermodynamic and electronic stabilities and interface strength of electrode-collector interface are investigated. It is shown that Co doping in the interface region can improve the interface strength of electrode-collector to different extents while Co doping in active materials and current collector decreases interface strength. Interfacial site is the best doping site, where Co atom tends to move to the first Sn layer near the interface region and forms strong chemical bonds with interfacial Sn, Cu and Li atoms. This reduces the accumulation of charges at interface and alleviates the attenuation of interface strength induced by lithiation. The W_{sep} of Sn/Cu and LiSn/Cu interfaces are increased by 9.4% and 17.7%, respectively. In

addition, Co doping enhances the electronic stability of electrode-collector interface. According to the change of W_{sep}, electronic stability and formation heat with Li content, the optimum Co doping content is given.

These findings are instructive to our understanding of the failure mechanism of Sn anodes and are also of great significance for clarifying their macroscopic fracture behaviours upon lithiation. It is expected that the results are helpful to the determination of a potential function in molecular dynamics and to the simulation of deformation and stress fields of electrodes at the mesoscopic scale. In addition, the study of doping modification of electrode-collector interface is helpful to improve capacity retention and cycle performance of batteries, which reduces the waste of materials and time caused by tedious experimental attempts and provides a theoretical basis for the further optimization of mechanical properties of Sn anode materials.

Keywords: Lithium-ion batteries; Sn anodes; mechanical properties; interfacial delamination; first-principles calculations

Publications by the author

Refereed journal papers

[1]   **Zhang PP**, Ma ZS, Wang Y, Zou YL, Lei WX, Pan Y, Lu CS. A first principles study of the mechanical properties of Li–Sn alloys. RSC Advances. 2015;5(45):36022–36029.

[2]   **Zhang PP**, Ma ZS, Jiang WJ, Wang Y, Pan Y, Lu CS. Mechanical properties of Li–Sn alloys for Li-ion battery anodes: a first-principles perspective. AIP Advances. 2016;6(1):015107.

[3]   **Zhang PP**, Yang YY, Ma ZS, Wang Y, Pan Y, Lu CS. A facile method to prepare electrode materials for pseudocapacitors with superior capacitive performance. Materials Letters. 2016;164:421–424.

[4]   **Zhang PP**, Ma ZS, Wang Y, Zou YL, Sun LZ, Lu CS. Lithiation-induced interfacial failure of electrode-collector: a first-principles study. Materials Chemistry and Physics. 2018;222:193–199.

[5]   **Zhang PP**, Jia ML, Ma ZS. Elastic properties of crystalline Li–Ge phases with increasing Li concentration: a first-principles study. AIP Advances. 2018;8:075331.

[6]   **Zhang PP**, Wang Y, Lei WX, Zou YL, Jiang WJ, Ma ZS, Lu CS. Enhancement effects of Co doping on interface properties of Sn electrode-collector: a first-principles study. ACS Applied Materials & Interfaces. 2019, accepted.

[7]   Ma ZS, Xie ZC, Wang Y, **Zhang PP**, Pan Y, Zhou YC, Lu CS. Failure modes of hollow core–shell structural active materials during the lithiation–delithiation process. Journal of Power Sources. 2015;290:114–122.

[8]   Gao X, Ma ZS, Jiang WJ, **Zhang PP**, Wang Y, Pan Y, Lu CS. Stress–strain relationships of Li_xSn alloys for lithium ion batteries. Journal of Power Sources. 2016;311:21–28.

[9] Liu YH, Bo ML, Yang XX, **Zhang PP**, Sun CQ, Huang YL. Size modulation electronic and optical properties of phosphorene nanoribbons: DFT–BOLS approximation. Physical Chemistry Chemical Physics. 2017;19(7):5304–5309.

[10] Wu H, Xie ZC, Wang Y, **Zhang PP**, Sun LZ, Lu CS, Ma ZS. A constitutive model coupling irradiation with two-phase lithiation for lithium-ion battery electrodes. Philosophical Magazine. 2019;99(8):992–1013.

Attended conference

Zhang PP, Ma ZS, Wang Y, Zou YL, Sun LZ, Lu CS. Lithiation-induced interfacial failure of electrode-collector: a first-principles study. The 3rd International Conference on Carbon Materials and Material Sciences, 20–22 November, 2018, Sydney, Australia (**Oral presentation**).

Contents

List of tables

List of figures

Chapter 1

Introduction

1.1 Background of rapid development of Li-ion batteries

With the gradual depletion of traditional non-renewable energies (such as natural gas, oil and coal) and the increasingly serious environmental pollution, the new environment-friendly clean energy has become the focus of global research. All countries in the world regard the development of new energy industries as an important measure to improve the national economic, scientific and technological levels. At present, the new energy industries have been widely developed in the world and a complete industrial chain and industrial agglomeration have been formed. Among many new energy industries, new energy vehicles have developed rapidly in the past decade. Countries and regions represented by China, Japan, the United States and the European Union have issued a series of policies to vigorously support the research and marketing of new energy vehicles. Their fast development has further led to the global research of its core component—power battery [1].

The commonly used power batteries are mainly Ni–H, lead-acid and Ni–Cd batteries, fuel cells and Li-ion batteries (LIBs). Lead-acid and Ni–Cd batteries have low energy density and working voltage and contain heavy metal pollution, which limit their promotion in electric vehicles and energy storage market. Ni–H batteries are mainly applied in hybrid electric vehicles, but their low working voltage cannot meet the performance requirements of pure electric vehicles and plug-in hybrid electric vehicles. Hydrogen fuel cells have advantages of no pollution, high energy conversion efficiency, diversification of fuel sources, and so on, but their manufacturing and use costs are relatively high, which make it difficult to achieve large-scale mass production and application. Compared with other power batteries, LIBs have higher gravimetric and volumetric specific capacities (see Figure 1.1), longer cycle life, lower self-

discharge rate, no memory effect and pollution. These merits make LIBs become the most potential new energy in the 21st century [2].

Up to now, LIBs are widely used in mobile power supplies, laptops, iPads, mobile phones, digital cameras, and other consumer electronic gadgets. Their application in electric vehicles, aerospace and power supply of mobile base station are also rising. In 2017, global shipments of LIBs reached 143.5 GWh and the usage of LIBs in electric vehicles, energy storage and other traditional fields are respectively 58.1, 11.0 and 74.4 GWh. The global shipments are expected to exceed 400 GWh by 2022 [1]. The widespread popularization of LIBs also puts forward higher requirements for battery performance. The current development of LIBs focuses on the optimizations in performance, cost and safety [3].
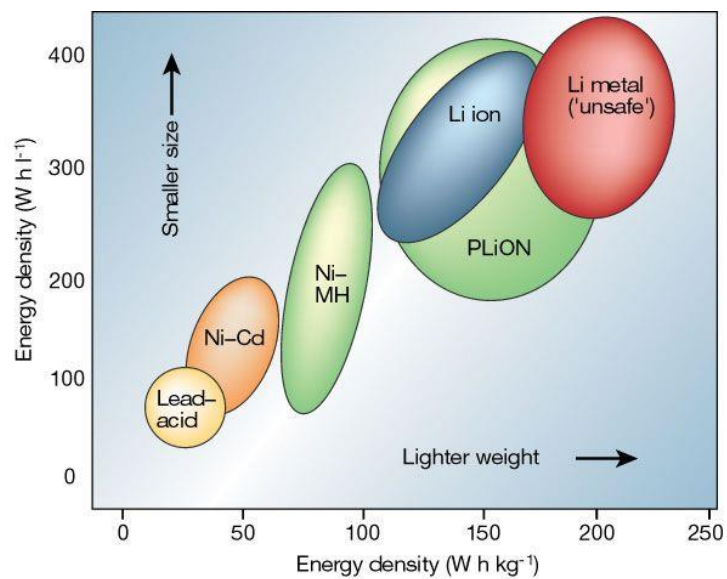
Figure 1.1 Volumetric and gravimetric energy densities of main power batteries [2].

1.2   Research objectives

As an important part of batteries, the anode plays a decisive role in the capacity and cycle performance of cells. At present, Carbon is the dominant commercial anode material. However, its theoretical specific capacity is not high (372 mAh g^{-1}) and the current actual specific capacity has basically reached its theoretical specific capacity.

Therefore, to further increase the energy density of batteries, the research of high-capacity anode materials has become an urgent problem to be solved.

Sn is a promising anode material for LIBs because of its high theoretical specific capacity, abundant reserves, low cost, environmentally friendly, and so on. However, Sn anodes go through large volume deformations in the processes of lithiation and delithiation, which causes the fracture and fragmentation of electrode materials, the delamination between active materials and current collector or conductive matrix, and the repeated fracture and reformation of solid-electrolyte interphase (SEI) film. This directly results in the rapid attenuation of capacity and cycle performance of batteries. In experiments, nanosized electrode materials with various shapes and sizes have been prepared to alleviate the damage caused by volume change, but this method can only improve the capacity and cycling performance to a certain extent, and the performance of LIBs is still far from meeting the commercial needs.

To fully use the high-capacity of Sn anodes and realize its optimization, it is imperative to have an in-depth understanding of the failure mechanism during charge-discharge processes. Currently, there is still lack of clear understanding of the evolution of mechanical properties of active materials (such as elastic constants, anisotropy, ductility and brittleness, etc.) and the electrode-collector interface (such as interfacial strength and interfacial fracture) during the lithiation of Sn anodes. Moreover, it is difficult to test the mechanical properties of electrode materials upon lithiation through experimental methods, because (1) some components of SEI film, such as LiOH and RCHOLi, have high chemical activity. A chemical reaction will occur when they encounter oxygen and steam; (2) Li_xSn alloys formed during lithiation-delithiation are thermodynamically metastable phases, which can be easily oxidized when they are exposed to air after electrochemical cycle. Therefore, there are high requirements for experimental operations and conditions; (3) influenced by the porosity of electrode materials, different electrode structures (e.g., composite and thin film electrodes) and humidity conditions (for example, liquid and solid electrolytes)

will largely affect the obtained mechanical properties; (4) different in shapes and sizes of active particles, electrode materials show varied volume deformation and stress evolution, which will change the lithiation kinetics (e.g., diffusion rate of Li-ions). This makes it difficult to obtain uniform results from different experiments.

Considering the difficulty of experimental measurements, by using first-principles calculations. This study aims to conduct a comprehensive study to the evolution of mechanical properties of Sn anodes during lithiation processes, which is significant to understand the macroscopic failure behaviours of electrode materials. Also, this research provides important mechanical parameters for the study of stress evolution, deformation and failure of different electrode materials under various coupling fields. Based on the interfacial failure mechanism, we further investigate the doping effects of the electrode-collector interface, which reduces the waste of materials and time caused by tedious experimental attempts and provides a theoretical basis for the further optimization and design of Sn anodes in experiments. The concrete research objectives are as follows:

(1) systematically exploring the evolution of mechanical properties of Sn active materials during lithiation to find out the microscale mechanical failure mechanism during charge-discharge processes.

(2) investigating the influence of lithiation on the interfacial mechanical properties between Sn active materials and Cu current collectors to give the microscale interfacial delamination mechanism.

(3) elucidating the effects of Cu_xSn alloys on the interfacial mechanical properties of electrode-collector interface.

(4) illustrating the doping effects of Co on the interfacial properties of electrode-collector to optimize the interfacial properties of electrode-collector interface.

1.3 Thesis organization

This thesis contains eight chapters, that is, introduction, literature review,

introduction to simulation method, results and discussions which is consist of four chapters, and conclusions and perspectives for future studies.

Chapter 1 introduces the background, remaining issues and solutions to the development of LIBs. Besides, it also includes the research objectives and organizations of this thesis.

Chapter 2 systematically summarizes the basics of LIBs, the current cathode and anode materials. In addition, this chapter involves a comprehensive description of the origin and effects of the mechanical fracture of Sn anodes and the current various methods to unveil the degradation mechanism of Sn anodes.

Chapter 3 briefly introduces the development history and theoretical basics of first-principles calculations and the simulation software and methods used in this research.

Chapter 4 reveals the evolution of mechanical properties of Sn active materials during lithiation processes, including elastic constants such as the orientation-averaged bulk (B), shear (G) and Young's (Y) moduli, Poisson's ratios (ν), the anisotropy, brittleness-ductility and ideal tensile strength. Based on the variations of mechanical properties, the microscale mechanical failure mechanism of Sn anodes is analysed.

Chapter 5 investigates the influence of lithiation on the interfacial mechanical properties of electrode-collector interface. In addition, the fracture behaviour of the electrode-collector interface under the interfacial tensile stress is also simulated. Based on the analysis of interfacial chemical bonds, the interfacial failure mechanism of Sn anode materials is revealed.

Chapter 6 elucidates the effects of Cu_xSn alloys on the interfacial mechanical

properties of electrode-collector interface. By simulating the stress-strain behaviour, this chapter also studies the fracture of the interface between Cu_xSn alloys and Cu current collector. These give the microscale mechanism for the excellent electrochemical performance of Cu_xSn containing electrode materials.

Chapter 7 unravels the doping effects of Co on the interfacial properties of electrode-collector, such as interfacial stability, interfacial bonding strength and chemical bonding. Through studying the change trend of interface strength, interfacial stability and formation heat with Co content, an optimal doping content is given.

Chapter 8 presents the useful findings from this research and puts forward some suggestions for future research in Sn anodes.

Chapter 2

Literature review

2.1 Basics of Li-ion batteries

2.1.1 A brief history of Li-ion batteries

Li batteries are batteries which use Li or Li alloys as anode materials together with non-aqueous electrolyte. They are mainly divided into Li-metal batteries and LIBs. The first Li-metal battery was developed by British chemist Whittingham in 1975 [4]. Since it uses metal Li as the anode material, it is called Li-metal battery. Li has the lowest mass density (0.534 g cm^{-1}) and the most negative electrode potential (−3.04 V) among all metallic elements. The theoretical specific capacity of Li metal battery is as high as 3860 mAh g^{-1}. However, spontaneous ignition occurs when Li is in contact with water and oxygen in normal atmospheric conditions because of the high reactive of Li [5]. In addition, Li dendrites form during charging due to the deposition of Li on the surface of electrode materials. Since the growth of Li dendrites consumes electrolyte, which causes irreversible capacity loss and an unstable electrode-electrolyte interface with the continuing of electrochemical cycles [6]. Besides, Li dendrites may destroy the formed SEI film, resulting in short circuit and even explosion of batteries. In view of safety risks of Li-metal batteries, Exxon terminated the research of Li-metal batteries and turned to look for Li alloys that allow the insertion and removal of Li-ions.

In 1979 and 1980, Godshall $et\ al.$ [7] and Goodenough $et\ al.$ [8] discovered that LiCoO$_2$ could be used as a stable cathode material for LIBs and Godshall $et\ al.$ [7] also found a series of ternary transition metal oxide cathode materials (Li$_x$CoO$_2$, Li$_x$MnO, Li$_x$FeO$_2$). Then, in 1983, Yazami $et\ al.$ [9] proved that Li-ions could reversibly embed into graphite electrode by using solid polymer electrolyte, which effectively solved the problem of Li dendrite and improved the safety of LIBs. In the same year, LiMn$_2$O$_4$

cathode material was discovered [10]. Manganese spinel materials are rich in reserves, low cost, and show good electronic and ionic conductivity and structural stability. Thus, $LiMn_2O_4$ is considered as a potential electrode material for LIBs. Although its capacity decays with electrochemical cycles, this can be solved by chemical modification [11]. In 2013, Manganese spinel was applied in commercial LIBs [12].

In 1991, Sony launched the first commercial LIBs, which use $LiCoO_2$ as cathode material and graphite as anode material. After that, LIBs developed rapidly and soon occupied most of battery market. Padhi *et al.* [13, 14] later found that $LiFe_2PO_4$ was an excellent cathode material. In the charge-discharge processes, it shows good thermal stability, cycle performance, and has a strong anti-overcharge ability. Up to now, $LiCoO_2$ and $LiFe_2PO_4$ are the most widely used cathode materials for commercial LIBs. From the beginning of the 21st century, the rapid development of consumer electronic products and new energy vehicle industry has promoted the continuous innovation and optimization of technologies of LIBs. Although the performance of LIBs has been largely improved, it still cannot meet the increasing demand for energy. Therefore, it has become the research focus of researchers to develop a new type of LIBs with lower cost, higher specific capacity and better cycle performance.

2.1.2 Composition and work principles

LIBs are kind of devices which can realize the conversion between chemical energy and electric energy. They rely on the concentration difference of Li-ions between cathode and anode electrodes to realize the intercalation and release of Li-ions in two electrodes. As shown in Figure 2.1, common LIBs mainly have four typical shapes, that is, cylindrical, square, button and thin film. All of them are mainly composed of cathode, anode, electrolyte, separator and shell [15, 16]. Electrolytes are usually Li salts dissolved in organic solvents, which are conductors of ions and insulators of electrons. The separator is a porous polymer film that separates the cathode and the anode during charge-discharge processes, but it allows Li-ions to pass

through [17]. The performance of a separator has a direct impact on the capacity, cyclability and safety of batteries. The cathode and anode materials connect to the external circuit through the current collector. Thus, the interface between active materials and current collectors is vital for the capacity and cycle performance of LIBs. Interfacial exfoliation will result in early capacity decay and poor cycle performance.
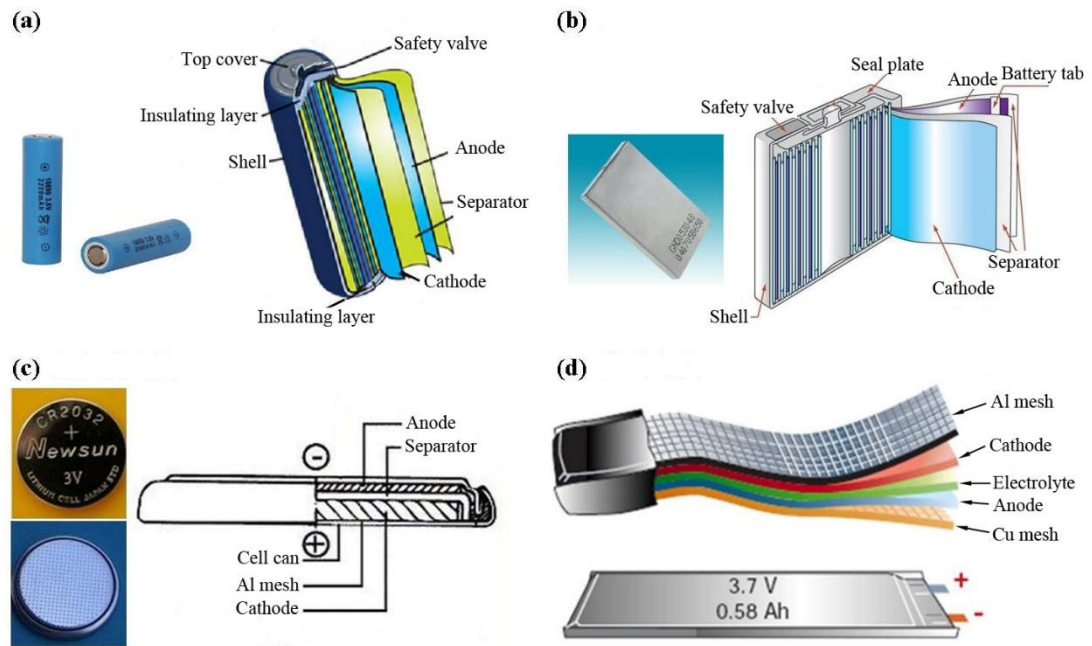
Figure 2.1 Four typical LIBs with shapes of (a) cylindrical, (b) square, (c) button and (d) thin film [2, 18].

There are two typical electrode structures. One type of electrodes is that the active particles are mixed with conductive agents (usually carbon black) and binders to form the electrode. This kind of electrode is widely popularized in commercial LIBs; The other is the thin film electrodes in which films of active materials in nanometres or microns thickness directly attach to the current collectors to form electrodes, without the use of conductive agents and binders. The working principle of LIBs is seen in Figure 2.2. During discharge, Li-ions are detached from the anode, go through the electrolyte and separator, and are taken by the cathode. At the same time, in order to maintain the balance of charges between two electrodes, electrons pass through the

external circuit from the anode to the cathode. Li-ions and electrons combine to Li atoms and are embedded in cathode materials. The charging process is the opposite.
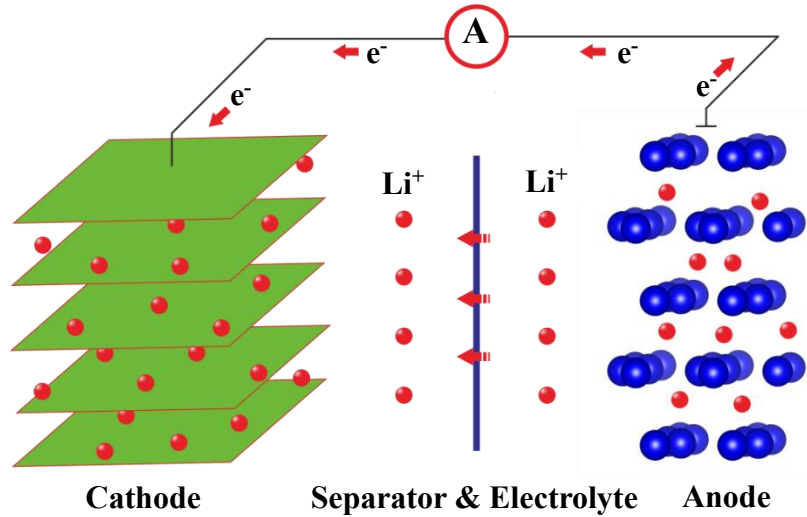
Figure 2.2 Schematic diagram of the working principle of LIBs during the discharge process.

2.1.3 Main advantages and disadvantages

As widely used energy storage devices, LIBs have many virtues. As illustrated in Table 2.1, compared to other secondary batteries, LIBs show many excellent characteristics [19]. For example, LIBs have high operating voltages (~3.6 V), which are about 2–3 times those of other batteries. The gravimetric and volumetric specific capacities of LIBs are respectively 2–3 and 2–4 times higher than those of other batteries. Thus, at the same capacity, LIBs are much lighter. These are the main reasons why LIBs are widely used in small consumer electronics. In addition, LIBs have fast charge-discharge speed and good cycle life (up to thousands of times), which is more than twice as many as other batteries. The self-discharge rate of LIBs is low at room temperature. The formation of SEI film on the surface of electrodes during the first charge-discharge can effectively prevent self-discharge. Furthermore, LIBs have no memory effect and it is environmentally friendly and free of heavy metals.

Table 2.1 Main performance parameters of common secondary batteries [19].

Performance parameter	Lead-acid	Ni–Cd	Ni–H	LIBs
Working voltage (V)	2.0	1.2	1.2	3.6
Operating voltage range (V)	1.8−2.2	1.4−1.0	1.4−1.0	4.2−2.5
Volume specific capacity (Wh L^{-1})	50−80	130−150	190−200	250−400
Mass specific capacity (Wh Kg^{-1})	30−50	50−60	60−70	100−150
Cyclability (Times)	400−600	300−600	300−600	500−2000
Operating temperature range (°C)	−40−65	−20−65	−20−65	−20−60
Self-discharge rate at room temperature (per month)	5−10%	10−20%	20−30%	2−3%
Memory effect	Yes	Yes	Nil	Nil
Anti-overcharge ability	High	Medium	Low	Low
Environmentally friendly	No	No	Yes	Yes

Although LIBs have been popularized, there are still some aspects needed to be improved [20]. For example, the cost of raw materials is high, such as that of $LiCoO_2$ and graphite. The high operating voltage of LIBs makes them incompatible with other batteries and the working voltage is unstable, which cannot guarantee the stable power supply. Besides, LIBs have a poor anti-overcharging ability, therefore, a special protection circuit must be equipped in LIBs. However, compared with its disadvantages, LIBs have irreplaceable advantages in portable electronic products, electronic vehicles, aerospace and other fields. With the development of new technologies, the application of LIBs will be more and more extensive.

2.2 Electrode materials

The performance of a cell such as energy density, cycle life and safety is dominated by its main components, especially the electrode materials [21]. Electrode materials what we usually call mainly refer to active materials in electrode structures, which allow the reversible insertion and removal of Li-ions [22]. Ideal active materials

should equip with the following basic characteristics: (a) electrode materials should demonstrate large reversible volumetric and gravimetric capacities and can stably cycle. In the charge-discharge process, no large volume deformation should occur [23, 24]; (b) the redox potential of cathode materials should be high enough, and the potential of anode materials should be higher than that of Li metal. In this way, the battery has a high overall working voltage, which could avoid the formation of Li dendrite [11]. In addition, to ensure the stability of charge-discharge voltage, the potential must not vary largely with Li concentration.; (c) cathode and anode materials should have high stability in the electrolyte. Cathode materials should not be soluble in the solvents of electrolyte and cannot react with the solvents of electrolyte. In contrast, anodes can react with electrolyte to form a stable SEI film, but, anode materials should not continue to react with the electrolyte when the stable protective film formed on the surface of electrodes [24, 25]; (d) cathode and anode materials should demonstrate high ionic and electronic conductivities [26]; (e) raw materials must be low-cost and environmentally friendly and should have abundant reserves.

2.2.1 Cathode materials

The Common cathode materials are $LiCoO_2$, $LiNiO_2$, $LiMn_2O_4$, $LiFe_2PO_4$ and Ni-Co-Mn ternary materials [7, 8, 13]. $LiCoO_2$ is the earliest cathode material used in commercial cells. Its successful application prompted LIBs to quickly replace traditional batteries in the field of consumer electronics. The actual specific capacity of $LiCoO_2$ can reach 155 mAh g^{-1}, which is about 55−60% of the theoretical specific capacity. Besides, its preparation process is simple and it has high voltage platforms and excellent rate performance, which makes $LiCoO_2$ become the most widely used cathode material in commercial LIBs [27]. However, there are some drawbacks in $LiCoO_2$, such as limited mineral resources, the high cost of raw materials, low thermal stability and environmental pollution. Furthermore, the capacity decays rapidly when charging or discharging at high current rates [28-30]. These greatly hinder its

application in power batteries.

LiNiO$_2$ has a layered structure and its actual specific capacity is about 180−200 mAh g^{-1}, which is slightly higher than that of LiCoO$_2$. Although Ni and Co display similar properties, the cost of LiNiO$_2$ is much cheaper than that of LiCoO$_2$, and LiNiO$_2$ has higher energy density and less toxicity. Also, it is not affected by overcharge and overdischarge. Specially, it illustrates good stability at high temperature and does not have high requirements for the electrolyte [31]. Unfortunately, its preparation process is difficult because it is hard to obtain stable structures since the Ni-ions tend to occupy the positions of Li-ions during the synthesis and delithiation processes, which hinder the diffusion path of Li-ions [32]. In addition, the thermal stability of LiNiO$_2$ is poor because it can be easily reduced, which limits its practical application [30]. Doping metal elements was found to be effective to enhance the thermal stability and cyclability of LiNiO$_2$ [33].

Compared with LiCoO$_2$ and LiNiO$_2$, LiMn$_2$O$_4$ has more obvious advantages. It has richer reserves, cheaper cost, environmentally friendly and is easy to recycle. Its actual specific capacity is about 120 mAh g^{-1}. The three-dimensional network structure can accelerate the diffusion of Li-ions, which is beneficial to high current charge-discharge. These advantages make LiMn$_2$O$_4$ demonstrate a great application prospect [29, 30]. However, the drawback is that the cycle performance of LiMn$_2$O$_4$ is not satisfactory due to the dissolution of Mn-ions in the electrolyte and the irreversible structural change from a layer structure to a spinel one during the delithiation processes [34, 35]. Moreover, the dissolution of Mn-ions also destabilizes the SEI films [28]. Many strategies were put forward to solve these problems. Doping other elements (such as Mg, Zn, Ni and Al) has been regarded as an effective measure to enhance the cyclability [36, 37].

Olivine structure LiFePO$_4$ has the merits of the above three cathode materials, that is, abundant raw materials, low cost and no pollution [13]. It demonstrates an actual specific capacity of about 170 mAh g^{-1} and shows good cyclability and safety

in the charge-discharge cycle. In addition, it also displays excellent thermal stability. These characteristics make LiFePO$_4$ receive much attention and is expected to be suitable candidate cathode materials for power batteries. However, due to its low voltage and intrinsic poor ionic and electronic conductivity, the energy density of LiFePO$_4$ is low. In experiments, other transition metals have been utilized to increase the voltage. The conductivity has been improved by surface modification such as coating a layer of conductive material, reducing the size of active particles and doping other metal elements [38].

Ni-Co-Mn ternary materials are two-dimensional layered electrode materials, which adjusts the properties of electrode materials by using different proportions of Co, Ni and Mn salts [39]. These three elements have different effects on the properties of electrode materials. For example, Co can increase the ionic conductivity of electrode materials, which is helpful to high current charge-discharge; Ni can increase reversible capacity, and Mn mainly plays a role in enhancing structural stability and generally does not contribute to electrochemical reactions [40]. Ternary electrode materials have the merits of low cost and high safety and they displays good cycling performance at room and high temperatures [41, 42]. They have high specific capacities of ~160 mAh g^{-1} in 2.5−4.4 V and ~200 mAh g^{-1} in the voltage range of 2.8−4.6 V, which makes them to be a promising candidate cathode material for LIBs with high energy and power density [40]. Nowadays, the main obstacle in the development of ternary materials is that their voltage platforms are low and their first charge-discharge efficiency also needs to be improved.

Currently, all these cathode materials have been applied in commercial batteries. However, with the rapid development of consumer electronics and the new energy industry, the demand for high-capacity cathode materials is rising. Therefore, further optimizing the performance of cathode materials has become the research focus.

2.2.2 Anode materials

At present, the widely researched anode materials for LIBs are carbon anode materials, alloy materials, and metal oxides, etc, as shown in Figure 2.3 [21, 43]. Carbon anode materials are the earliest anode materials used in commercial LIBs. They have low cost, stable electrochemical cycling performance and environmentally benign. Up to now, they are still the main anode materials of commercial LIBs [44, 45]. Carbon anode materials can be divided into graphite, hard carbon, soft carbon, carbon nanotubes and so on [45]. Graphite has stable voltage platforms and good conductivity. During charging, Li-ions can insert into layered graphite structure and form Li_xC compounds. The electrode structures before and after the intercalation of Li-ions show good structural stability without large volume deformation. The theoretical specific capacity is 372 mAh g^{-1} and the actual specific capacity can reach 360 mAh g^{-1}. Its coulomb efficiency is more than 90% [43, 46]. However, graphite cannot be well compatible with electrolyte, resulting in a low diffusion coefficient of Li-ions [47]. In addition, the low theoretical specific capacity of graphite cannot meet the increasing demand for capacity, therefore it is necessary to find other high-capacity anode materials. There is good compatibility between soft carbon and organic electrolytes, but soft carbon shows a large first irreversible capacity and cannot output high voltage. Hard carbon presents a high reversible specific capacity (500−800 mAh g^{-1}), but it exhibits poor cycle performance [47, 48]. Carbon nanotube has a large specific surface area, high Young's modulus (about 1 TPa) [49] and tensile strength (up to 60 GPa) [50], excellent electrical conductivity and high reversible specific capacities (300−600 mAh g^{-1}) [51, 52]. These merits make Carbon nanotube arouse the upsurge of research [53, 54]. However, like soft carbon, Carbon nanotube has a large irreversible capacity for the first cycle and its volumetric specific capacity is relatively low [43]. These defects restrict the wide application of carbon nanotubes.
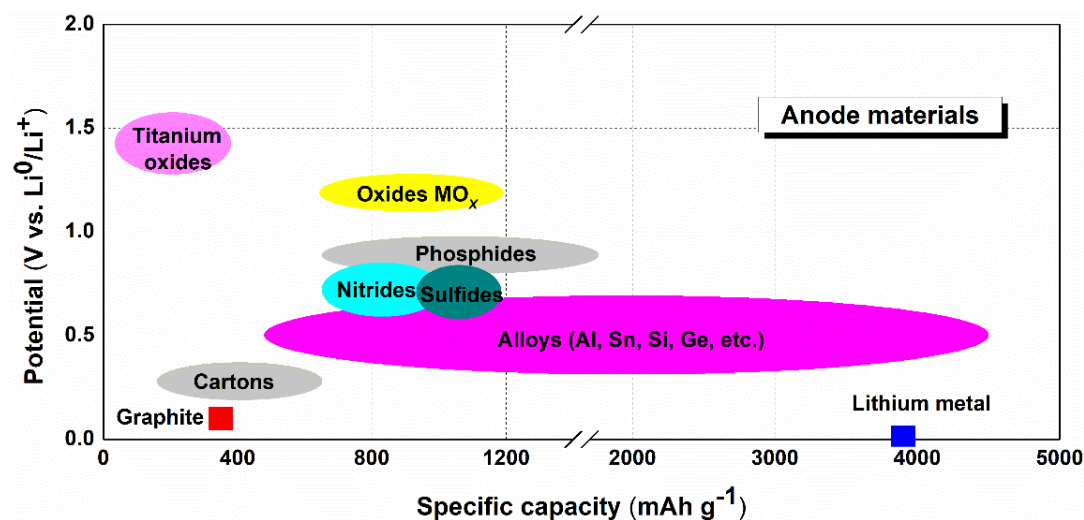
Figure 2.3 Potentials vs Li/Li$^+$ and specific capacities of common anode materials for LIBs [55].

The storages of Li in alloy anodes are realized by the chemical reactions of Li with many metals or metal-like elements (such as Si [56-58], Ge [59, 60], Sn [61-63], Al [64, 65]) to form alloy systems. Such materials usually display very high theoretical specific capacities. The high intercalation potential of Li-ions in alloys avoids the hidden danger caused by Li deposition and Li dendrite which form during rapid charge-discharge processes. The low delithiation voltage makes alloy anodes show high working voltage and energy density [66]. Furthermore, they have other advantages. For example, Sn displays high conductivity, Si has an abundant reserve and Ge demonstrates high diffusion coefficient of Li-ions [67]. Unfortunately, the actual application of these alloy anodes is plagued by the massive volume deformation during charge-discharge. The large internal stress in electrode materials caused by volume change will cause decrepitation or breaking-up of electrode materials, the exfoliation of active materials from current collector and the repeated fracture and reformation of SEI film. All these result in increased cell impedance, an early capacity attenuation and poor cycle performance [16, 68]. Also, the high stress in electrode materials affects the diffusion of Li-ions, which further influence the rate of electrochemical reaction [69, 70].

In view of the size-dependent fracture behaviour of alloy anodes, researchers have extensively studied various nanocomposites and nanostructures (such as nanowires [71-73], nanoparticles [74, 75], nanofilms [76]) to control the volume expansion/contraction. The large surface-to-volume ratio of nanomaterials can facilitate strain relaxation, reduce the diffusion distance of Li-ions and increase the contact area between electrodes and electrolytes which enhances the rate performance. Specially, the free of dislocation in nanosized structures make them less vulnerable to crumbling and cracking [77]. Furthermore, the introduction of inert components which do not react with Li can also greatly relieve the damage induced by volume deformation, thus improving the capacity retention [67, 78].

According to different chemical reaction processes, transition metal oxides can be divided into two categories: (1) the embedding of Li-ions in electrode structures only causes structural changes, without the formation of Li_2O, such as MoO_2 [79], Fe_2O_3 [80, 81], TiO_2 [82, 83] and WO_2 [43, 84, 85]. In this case, Li-ions can well reversibly insert and remove from these materials, which make them show good cycle performance. However, their specific capacities are not high while the charge-discharge potentials are relatively high. In experiments, nanostructures or doping has been applied to solve these problems; (2) transition reaction occurs during the intercalation of Li-ions together with the formation of Li_2O. Because of the high electrochemical activity of Li_2O, it can be reduced to metallic Li in the subsequent discharge processes. These materials are M_xO_y (M = Ni, Sn, Cu, Co, etc.) [43, 82, 86]. They generally have high specific capacities (400−1000 mAh g^{-1}), good cycle capacity and perform well in high rate discharge. The downside is that part of the Li_2O cannot be converted into Li, and the formation of the SEI films consume Li, which lead to a large irreversible capacity loss. In addition, the discharge platforms of most transition metal oxides are high, and their conductivity is not good. The formation of Li_2O will further reduce conductivity. All of these impair the cycling performance of electrode materials. Moreover, this kind of electrode materials will experience large volume

deformation in charge-discharge processes, which will cause the destruction of electrode structures [82]. In experiments, the electrochemical performance of these electrodes is optimized by coating, nanocrystallization, doping or the use of integrated electrodes [45].

2.3 Failure of Sn anodes

Nowadays, the commercial cathode materials are mainly $LiCoO_2$, $LiFePO_4$, $LiMn_2O_4$ and $Li(Ni_xCo_yMn_{1-x-y})O_2$ ternary materials, and anode materials are mainly carbon materials [87]. However, with the popularization of consumer electronic products and the increasing requirements of endurance mileage for electric vehicles, the current LIBs cannot meet the needs of high-capacity and long service time. Therefore, the development of high-capacity anode materials has become the focus of researchers.

As illustrated in Table 2.2, $LiMn_2O_4$ and $LiNiO_2$ are the main high-capacity cathode materials. Alloy anodes (e.g., Si, Ge, Sn) and transition metal oxides present much higher theoretical specific capacities than that of carbon anodes. For example, the theoretical specific capacity of Si (4200 mAh g^{-1}) and Ge (1600 mAh g^{-1}) are respectively about 10 and 4 times that of carbon anodes [67]. However, these materials suffer from large volume changes in charge-discharge processes. The volume deformations of Si, Ge and Sn are about 400%, 270% and 273%, respectively. The huge volume expansion/extraction will lead to large diffusion-induced stress in the lattice of electrode materials, which will cause the disintegration and pulverization of active materials, the loss of electric contact of the electrode-collector interface, and the continuing fracture and reformation of the SEI membrane. These will result in an irreversible consumption of electrolyte and rapid attenuation of capacity. Therefore, the mechanical failure caused by volume deformation has become the bottleneck restricting the application of high-capacity anode materials in LIBs.

Table 2.2 Theoretical specific capacities (mAh g^{-1}) and volume deformations of high-capacity electrode materials for LIBs [16, 28, 82].

Electrode materials		Formula	Theoretical specific capacity	Volume deformation
Cathodes	Lithium cobalt oxide	($LiCoO_2$)	274	
	Lithium nickel oxide	($LiNiO_2$)	276	3–5%
	Lithium manganese oxide	$LiMn_2O_4$	148	
		$LiMnO_2$	286	>10%
	Lithium iron oxide	$LiFe_2PO_4$	170	7%
	Nickel-cobalt-manganese ternary material	$Li(Ni_xCo_yMn_{1-x-y})O_2$	170–280	3–7%
Anodes	Carbon	C	372	9%
	Alloy anodes	Si	4200	400%
		Ge	1632	270%
		Sn	994	273%
	Transition metal oxides	Mn_xO_y	600–1000	150–180%

Many research groups at home and abroad have done a lot of research on the mechanical failure of high-capacity electrodes. In foreign countries, by using in situ transmission electron microscopy and X-ray, the microstructure evolution of Si anodes during the removal and intake of Li-ions was characterized by Chon and Guduru [88], Limthongkul [89], Obrovac and Krause [90], Li and Dahn [91]. When Li content x is about 3.5, the transformation from crystalline to amorphous phases occurs in Si anodes, and there is a sharp phase boundary of about 1 nm between the crystalline and amorphous phases (see Figure 2.4) [88]. Besides, Guduru *et al.* [88] investigated the evolution of stress and fracture processes of Si wafers at initial lithiation stage and they further determine the changes of average stress in lithiated amorphous Si by using Stoney method (Figure 2.5). Using nanoindentation technique, Cheng *et al.* [92] described the variations of Young's modulus and hardness of Si composite electrodes

under different charging conditions. The effects of porosity, liquid environment and attenuation on mechanical properties of Si anodes were unveiled.
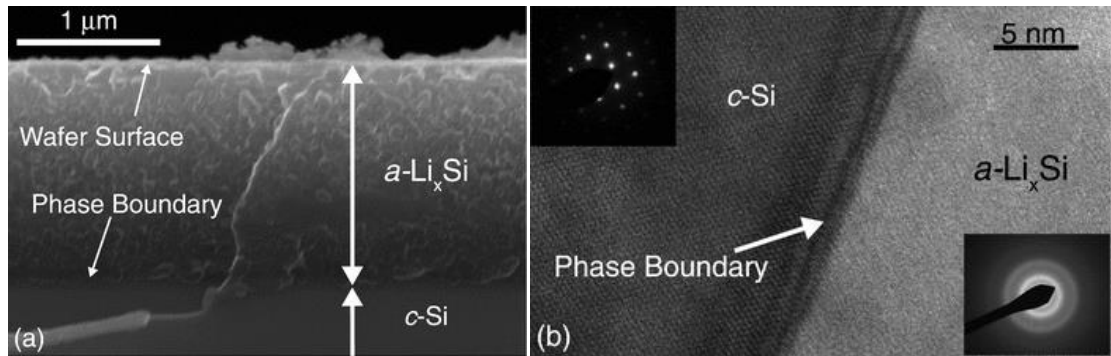
Figure 2.4 (a) Scanning electron microscopy images of the cross section of amorphous Si lithiated for 25 hours and (b) the corresponding high-resolution transmission electron microscopy. An obvious interface can be observed between the crystalline and the amorphous phases [88].
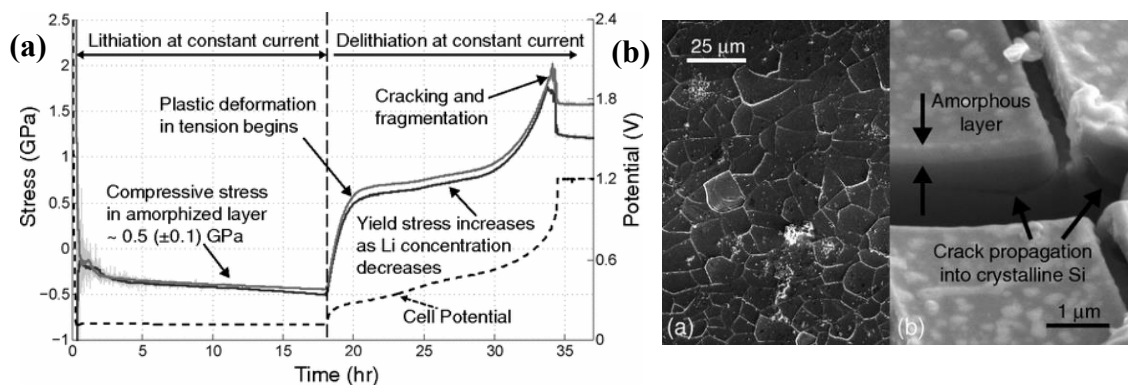
Figure 2.5 (a) The evolution of stress in Si film electrode during the lithiation and delithiation and (b) the disintegration of the amorphized layer in Si anodes during delithiation. The electrode material is subjected to compressive stress (~ 0.5 GPa) during lithiation. In the process of delithiation, the stress will quickly reverse from compressive stress to tension. With the continuing of delithiation, the tensile stress increases gradually, and the large tensile stress will cause the plastic deformation and fragmentation of electrode materials, as seen the sudden drop of stress [88].

By using first-principles calculations, Shenoy and Qi *et al.* [93, 94] studied the variations of elastic constants and interfacial properties of electrode-collector interface during lithiation of Si anodes. The micromechanical failure mechanisms of Si active materials and the electrode-collector interface were revealed. Besides, Wang *et al.* [95] explored the shear deformation of Si electrode-collector interface during lithiation and the delamination of the electrode-collector interface was explained from the perspective of interface atomic slip. Hwang *et al.* [96] compared the change of structures, electronic and mechanical properties of alloy anodes upon lithiation and found that the alloying reaction between Li and Sn was much easier to occur according to the change of mixing entropy. Based on plastic mechanics and diffusion equation, Suo *et al.* [97] considered the effect of embedded atoms on solid and chemical reactions by establishing a coupled mechanical-electrochemical model. Utilizing theoretical simulations and experimental characterizations, Nix and Cui *et al.* [98] revealed the evolution of stress and morphology of Si nanowires with different sizes before and after lithiation, and the critical size to avoid fracturing was given. Bower and Guduru [99] unravelled the mechanical and electrochemical responses of Si amorphous thin films during lithiation, which provided important material parameters in the electrochemical cycle. Based on the large strain theory of continuum mechanics, Zhang and Li *et al.* [68] proposed that stress can affect the lithiation kinetics.

The research on the failure mechanism of electrode materials in China started a little late, but some characteristic research teams form in recent years. For example, by using theoretical analysis and numerical simulation, Shanghai University [100-102], Beijing Institute of Technology [103], University of Science and Technology of China [104], The Hong Kong Polytechnic University [105], Institute of Mechanics and Physics of the Chinese Academy of Sciences [106, 107], Central South University [108-110], and Tongji University [111, 112] studied the deformation, exfoliation, stress distribution, surface and interface effects of electrode materials in the process of lithiation and delithiation, and a series of multivariable coupled mechanical models

were established. Tianjin University *et al.* [113] used the optical method to observe the real-time deformation of electrode materials during lithiation. Combined with theoretical simulations and experiments, the change law of diffusion stress was presented. Based on electrochemical reactions and neutron radiation effect, the evolution of the electrochemical performance of LIBs in the radiation environment was studied [114]. By using numerical analysis and finite element simulation, the phase transition lithiation model and stress prediction model of electrode materials with different structures are also established. The mechanical failure of electrode materials under various coupling fields (thermal-mechanical-chemical coupling) is also explored [18, 115].

As a typical high-capacity anode material, Sn has a high theoretical specific capacity. In addition, it is rich in reserves, cheap, environmentally friendly, and shows high storage capacity of Li-ions and electronic conductivity (1.1×10^{-7}) [116, 117]. Compared with Si and Ge, the theoretical capacity of Sn is relatively low. However, Sn anode materials are easier to synthesize. Although there are abundant reserves of Si in the earth crust, extracting a large amount of pure Si from silica is difficult and this process would consume a lot of energy and may cause environmental pollution. Specially, it is hard to obtain high-quality Si using the commonly used reductants (such as carbon materials). In addition, considering the large volume changes in lithiation and delithiation, it is almost impossible to make full use of its theoretical specific capacity. As for Ge, its reserves on earth are relatively small and widely distributed, so how to obtain high concentration Ge is a problem. In contrast, Sn shows a slightly higher discharge voltage than metal Li (0–400 mV) which avoids the safety risks caused by Li deposition and Li dendrite and Its volume deformation during charge-discharge is also smaller than that of Si and Ge anodes [66]. Moreover, Sn anodes do not have the problem of solvent co-intercalation which happens in graphite anodes [67]. Considering these characteristics, Sn anode is chosen as the research object to investigate the mechanical failure mechanism of high-capacity anode materials.
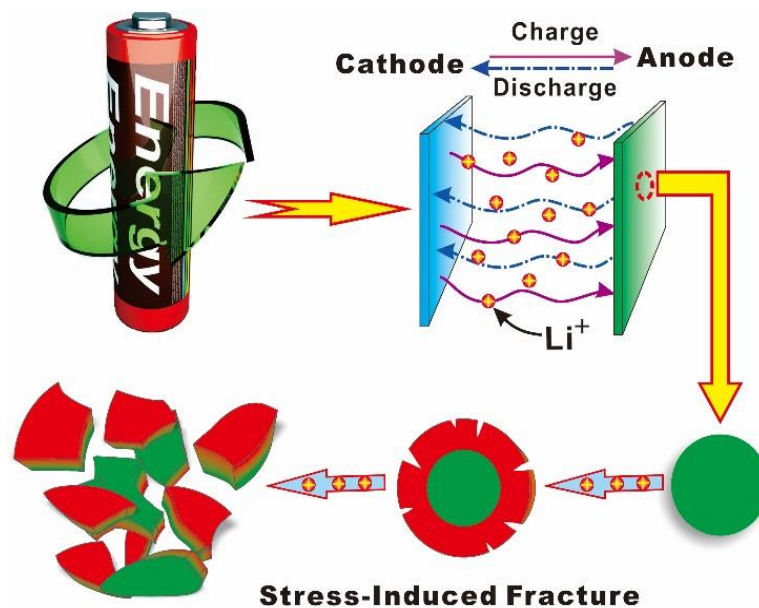
Figure 2.6 Schematic illustration of mechanical failure of Sn electrode materials during charge-discharge processes [118].

Despite the appreciable merits, however, the practical application of Sn anode materials is far from commercialization. Since Sn experiences large mechanical stress during the lithiation and delithiation process, which leads to the mechanical instability of electrode materials and further causes the early capacity loss and poor cycle life, as illustrated in Figure 2.6 [102, 118]. Stresses in Sn anodes are mainly induced by the electrochemical reactions in electrochemical cycles and external stresses arising from battery packing in the manufacturing processes [16]. Here, we mainly focus on the internal stresses created by electrochemical reactions.

2.3.1 Causes of stress development

Lithiation and delithiation of Sn anodes occur through alloying and dealloying reactions with Li-ions occupying the interstitial sites of the lattices and binary alloys (e.g., Li_2Sn_5, $LiSn$, Li_7Sn_3, Li_5Sn_2, $Li_{13}Sn_5$, Li_7Sn_2 and $Li_{17}Sn_4$) progressively form during the lithiation progresses (see Figure 2.7) [119-122]. Sn can host up to 4.25 Li atoms per atom. This leads to a high theoretical capacity of 994 mAh g^{-1} which is

about 2.5 times that of graphite anodes. But such a high Li loading leads to a net volume change of about 300%, which is about 20 times that of graphite anodes [66]. The enormous stress caused by the colossal volume change is a major fraction of stresses in Sn anodes.
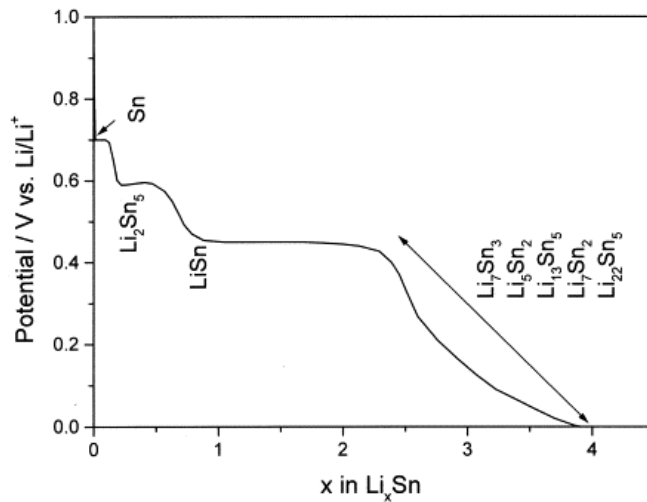
Figure 2.7 The characteristic charging curve of Sn anodes and the corresponding Li_xSn alloys formed during the charging process [119].

The stress in active materials is not uniform and its magnitude influences by many factors, such as the electrode architecture, the electrode composition, the electrochemical lithiation and delithiation rate and different lithiation stages [123-127]. The three main reasons for stress generation are summarized as follows [16]: (1) physical constraints on morphology change during charge-discharge processes. The repeated insertion and removal of Li-ions during charge-discharge processes induces varied lattice sizes and structures, and transformation of different alloy phases which leads to the macroscopic volume and morphological changes [119, 125, 128-131]. But volume/morphology changes are generally constrained by neighbouring particles, current collectors/substrates, or the space/geometry of the cells, which will generate enormous internal stresses in electrode materials, as seen in Figure 2.8 [124, 132-134]. These are the dominant source of stress in Sn electrodes; (2) interparticle contacts. The
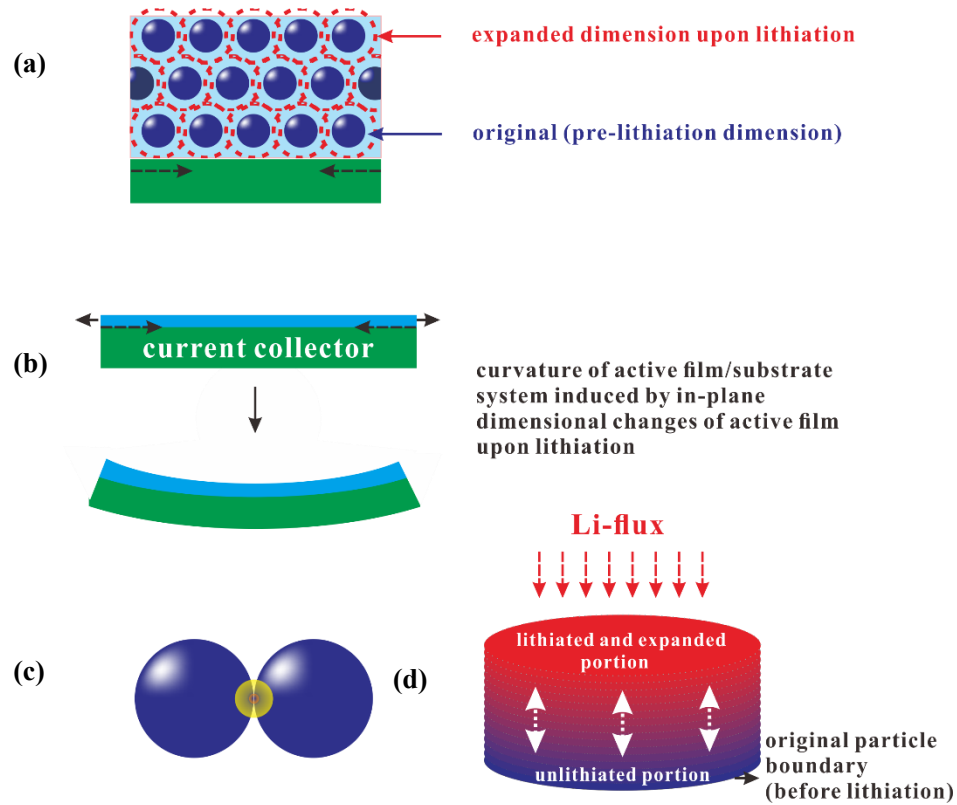
Figure 2.8 Schematic illustration of (a) constraining effects of inactive matrix, current collector/substrate, and expansion constrained by interparticle contacts and by binders/conductive additives upon lithiation of porous composite electrode; (b) the in-plane lithiation expansion of thin film electrode is constrained by current collector/substrate; (c) Stress generation due to the contact of expanded lithiated particles; (d) stress discontinuities caused by Li-concentration gradient between lithiated and unlithiated parts of a particle or by different crystal phases/structures between adjacent regions [134].

large volume expansion of active particles upon lithiation makes particles contact with each other, which would cause huge stresses at the contact points [124]; (3) Li-concentration gradient and lattice mismatch between different alloy phases. Lithiation and delithiation processes happen through the diffusion of Li-ions in active materials. Upon lithiation, Li-ions diffuse from the surface to the core and vice versa. In these processes, steep Li-concentration gradients form in the interior of active materials (Figure 2.9). This is arising from transport limitations that are related to the diffusivity

of Li-ions and current density [135]. Since phase transformations are associated with Li-content, these large Li-concentration gradients would lead to different phase transformations and further cause differential volume and morphology changes from the surface to the core [136-139]. This means that the neighbouring regions within the same active materials exist different alloy phases with various crystal structures, molar volume and mechanical properties. The interaction/contact between these regions results in mismatch-induced stress [140-143].
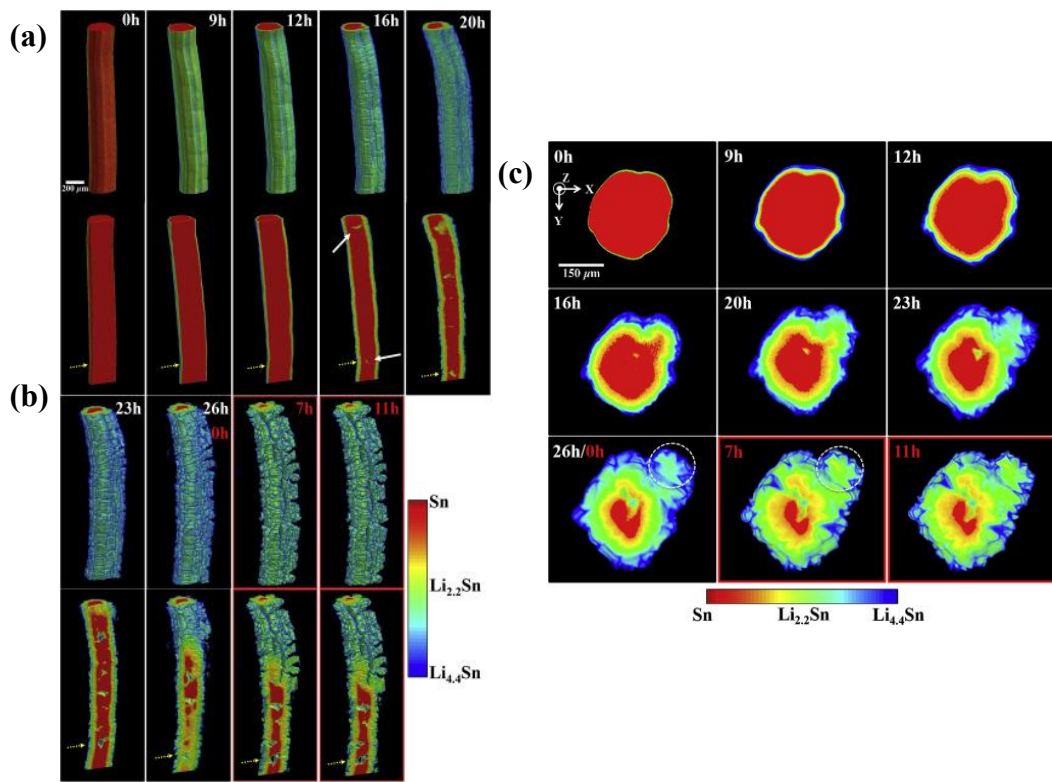
Figure 2.9 3D rendered volumes of (a) the surface and (b) interior of a Sn wire at different lithiation (white time stamps) and delithiation (red time stamps) time, and (c) the corresponding cross-sectional slice views of the region indicated by the yellow arrows [146].

Because the lithiation and delithiation processes are dynamically transformed during charge-discharge, the stress changes repeatedly between the compressive stress during lithiation and the tensile stress during delithiation, as shown in Figure 2.5(a),

which aggravates the damage on active materials [134, 144, 145]. With the repeated insertions/removals of Li-ions during electrochemical cycles, the accumulating damage can be described by the fatigue mechanism [16].

2.3.2 Effects of stresses on Sn anodes

Power density, energy density and cycle lifetime are three main parameters to measure the performance of a battery, which are associated with the lithiation and delithiation rates, the available Li-capacities in electrode materials and the ability of an electrode to keep appreciable specific capacity and structural integrity during electrochemical cycles [134]. The large stress developed in electrochemical cycles can affect the mechanical integrity of electrode materials, the formation and fracture of SEI films and various other factors relating to electrochemical behaviour. These would influence the electrochemical performance of batteries to different extents.
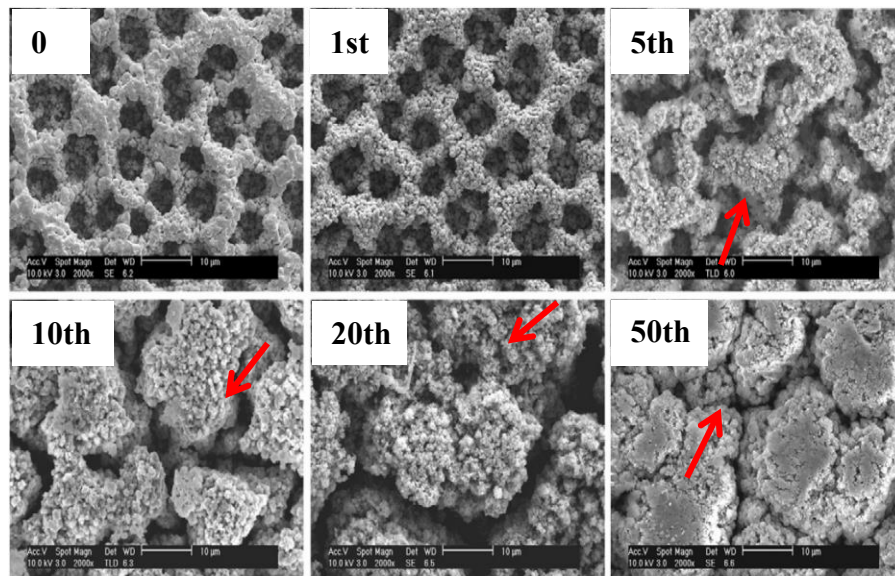
Figure 2.10 Surface morphology of Sn/Cu foam electrode after different cycles [147].

(1) Impacts of stress on structural integrity of electrode materials

The mechanical failure of electrode materials is influenced by many factors, such as the mechanical properties of electrode materials, electrode architecture, the extent

of volume changes in repeated lithiation and delithiation processes, and the mechanical constraints [124, 127-129, 140, 146, 148-150]. Besides, the extent of lithiation and delithiation and the rate of electrochemical cycling also have large relations with mechanical failure [151, 152]. Cracking and crumbling of active electrodes and the surrounding matrixes are common mechanical degradations in metal-alloy anodes [117, 125, 149, 151, 153-155]. In most circumstances, the fracture portions lose contact with the rest of active materials and even the current collectors/conductive carbons, which leads to the breakdown of conductive networks (Figures 2.10 and 2.11) and less and less available active materials with progressive fracturing [119, 125, 128, 156]. Furthermore, the large stress also damages the binder and reduces the pore volume [129]. All of these impair the mechanical integrity of electrode structures, which in turn results in the irreversible capacity loss, decreased energy density and poor cyclability of batteries in electrochemical cycling. The stress-induced fracture is one of the key factors for the poor performance of LIBs.
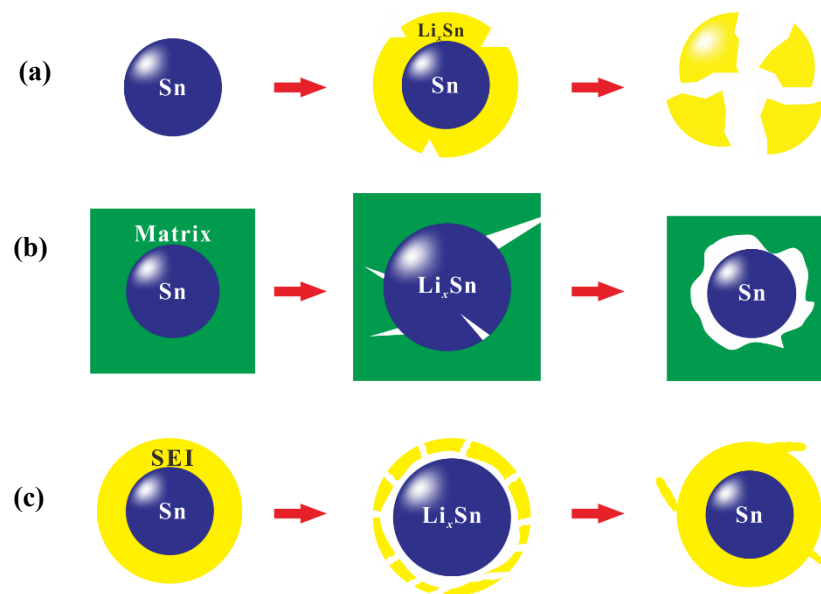
Figure 2.11 The influence of lithiation/delithiation-induced stress: (a) fracture and pulverization of active particles, (b) lose electrical contact between active materials and conductive matrixes/current collectors and (c) iterative breakdown and reformation of SEI films [157].

(2)   Impacts of stress on the fracture and reformation of SEI films

Fracture of electrode materials creates fresh electrode surfaces. When the fresh metal surfaces meet electrolyte, the passivating SEI films form [25]. Since the formation of SEI layer consumes the organic electrolyte, which would cause continuous irreversible consumption of Li in the electrode system, even the depletion of liquid electrolyte [158]. This in turn causes the capacity decay. In addition, the large volume expansion and contraction also lead to the constant growth of unstable SEI on the surface of anode materials [159, 160]. The iterative breakdown and reformation of SEI layer would form thick SEI layer on the surface of electrode particles, impeding the effective transport of ions/electrons through the SEI layer and further affecting the subsequent lithiation and delithiation processes [161, 162]. This will influence the electrochemical performance of LIBs [163].

(3)   Effects of stress on lithiation kinetics

The process of electrochemical lithiation and delithiation contains the long-range diffusion of Li-ions and electrons, and the whole process involves the coupling of kinetic process and stress. Lithiation kinetics (such as lithiation rate, lithiation anisotropy) modulate the generation of stress, which in turn affects the electrochemical reaction. The stress produced in the lithiation process will reduce the diffusion rate of Li-ions in the lithiated electrode materials and the electrochemical reaction rate [69, 164-166]. The lithiation anisotropy of alloys will affect the magnitude and distribution of stress in electrodes, which will further lead to varied lithiation hysteresis, the anisotropic expansion and fracture of electrode materials [167].

2.4   Failure mechanism of Sn anodes

The electrochemical performance of electrode materials has strong relationships with its structure, including the phases and properties, particle sizes, dimensionality, interface, etc. [43, 67, 77, 127, 128, 168, 169]. To conquer the mechanical degradation

and realize the sophisticated design of Sn anode materials, numerous efforts have been dedicated to elaborately tailoring the structures to accommodate the large volume change. Sn-based nanostructures with various dimensionalities and shapes have been synthesized in these years, ranging from zero-dimensional nanoparticles to one-dimensional nanowires or nanotubes, two-dimensional nanoplates, and three-dimensional nanoarchitectures [149, 170-179]. However, the current performances and technologies still cannot meet the increasing demand for energy. This gap requires the more sophisticated design of electrode materials based on a deep understanding of the fundamental mechanical failure mechanism during the lithiation and delithiation processes. The recent development of experimental techniques and multiscale theoretical simulations promotes our understanding of the degradation mechanism of Sn anode materials [125, 128, 139].

In experiments, various *ex-situ* and *in-situ* technologies have been used to investigate the evolution of volume/morphology change, phase transformation and fracture of Sn electrode materials [123, 131, 139, 169, 180]. The recent advances *in-situ* characterization methods such as *in-situ* X-ray tomography and *in situ* transmission electron microscopy facilitate the real-time observation of the morphology and phase transition mechanism of electrode materials during the lithiation and lithiation processes [181, 182]. This information is vital to simulate the stress evolution and its impact on electrochemical reactions. For example, by using *in-situ* transmission X-ray microscopy, Chao *et al.* [183, 184] studied a core-shell reaction mechanism of Sn particles with diameters of ~10 μm. Radical cracks and porosity respectively appear in the first lithiation and delithiation. Utilizing *in-situ* transmission electron microscopy, nanoscale Sn particles and nanowires show complex size-dependent failure behaviours during the sequential phase transformations in lithiation and delithiation processes [124, 125]. No surface cracks appear in Sn particles with diameters of a few hundred nanometres after the first lithiation, but there are severe pulverization and pore growth in active materials with the removal of Li-ions. In

addition, the aggregation of small particles upon lithiation has been observed, but the formed large particles usually pulverize during delithiation [124]. Similarly, using *in-situ* transmission X-ray microscopy, Cook *et al.* investigated the influence of porosity on the volume expansion and shrinkage of Sn anodes during lithiation and delithiation, and found that nanoporous active particles can largely relieve the volume change and no cracks were observed [133].
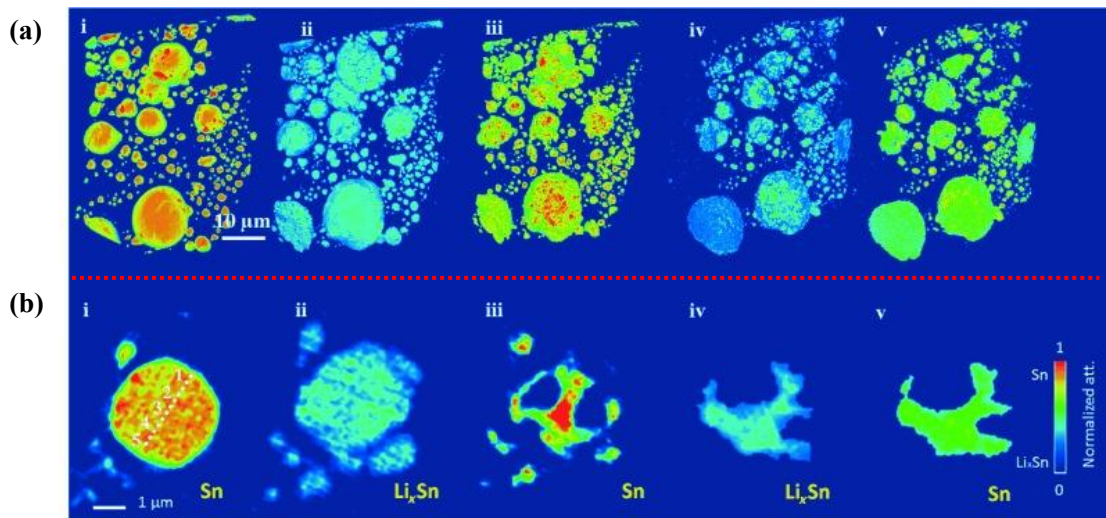
Figure 2.12 (a) Three-dimensional morphology evolution of Sn particles during the first two lithiation-delithiation cycles and (b) the corresponding cross-section images of a single Sn particles in these processes. Figure i is the morphology before lithiation; Figure ii(iv) and iii (v) are the morphologies after the first (second) lithiation and delithiation. It is seen that the electrode material shows obvious volume expansion and cracks after the first lithiation. After the first delithiation process, fracture and pulverization are obviously observed on the surface and in the inner part of electrode materials. The structure tends to be stable in the second cycle with a small volume deformation in this process [128].

More recent work reveals the real-time microstructural changes of a Sn electrode at the nanoscale using *in-situ* three-dimensional X-ray nanotomography. As seen in Figure 2.12, the first two cycles have severe impacts on structural damage of electrode

materials, then the morphology stabilizes after a few cycles [128]. Similarly, using X-ray tomography, Gonzalez *et al.* [146] unravelled the lithiation-induced creep and stress relaxation of Sn wires with microscale diameters. Different from Sn active particles whose fracture and pulverization are mainly in delithiation processes, most of the fragmentations and damages of nanowires come from the initial delithiation and the following lithiation and delithiation processes, and no obvious morphology changes/damages appear when the initial lithiation is less than 25%. Furthermore, the damages during the following cycles are dominated by overpotential which can be mitigated by selecting suitable overpotential. Besides, *in-situ* atomic-force microscopy was utilized to unveil the morphology change of patterned Sn films [185]. Also, neutron depth profiling spectroscopy was applied to characterize the distribution of Li concentration in electrode materials [135]. Wafer curvature measurements and nanoindentation tests were performed to reveal the stress evolution in the electrochemical reaction of Sn anode materials [186, 187].

Apart from experimental methods, macroscale theoretical modellings have been developed to study the degradation of Sn anode materials [187-190]. For example, Ma *et al.* [191] simulated the dynamic lithiation process of film and hollow core-shell electrodes via finite element analysis, which provides the dynamic evolution of Li-ion concentration and stress in electrode materials. Combining the theory and experiments, they also determined the relationship among critical failure, structural dimensions and mechanical properties [188]. Besides, Yang *et al.* [132] developed models to consider the influence of insertion-induced deformation on structural degradation of thin-film electrodes, which confirms the relationship between the critical concentration of solute atoms and average damage size for charge-induced cracking and buckling in an elastic film. Based on the cohesive model, Zhang *et al.* [192, 193] investigated the interfacial delamination of the thin-film electrode for LIBs and introduced a theoretical method to determine the states of charge and time at which delamination starts for patterned thin-thin electrodes. Huang *et al.* [140] proposed a mechanics foundation to understand

the stress evolution upon lithiation of high-capacity anode materials.

In addition, microscale simulations are also used to have a deep understanding of the lithiation processes of electrodes materials. For example, by using ab initio random structure searching and species swapping methods, Morris *et al*. [194] conducted a structure prediction to the crystal structures of all stable and metastable Li_xSn alloys. Similarly, Jojari *et al*. [195] explored the crystal structures of the stable and metastable Li_xSn phases at the ambient and moderate pressures and their properties to understand the role of pressure in redefining the reaction mechanism during lithiation and delithiation processes. Using ab initio calculations, Zhang *et al*. [166] evaluated the phase evolution of Li_xSn alloys during lithiation and the effects of elastic-strain energies on phase transitions of alloys, which shows that the lithiation processes of Sn anodes can be classified into two steps, e.g., the two-phase and selective equilibrium, as seen in Figure 2.13. Besides, the diffusion behaviours of Li in Sn and Li_xSn alloys are also calculated which helps to deeply understand the lithiation process [196].
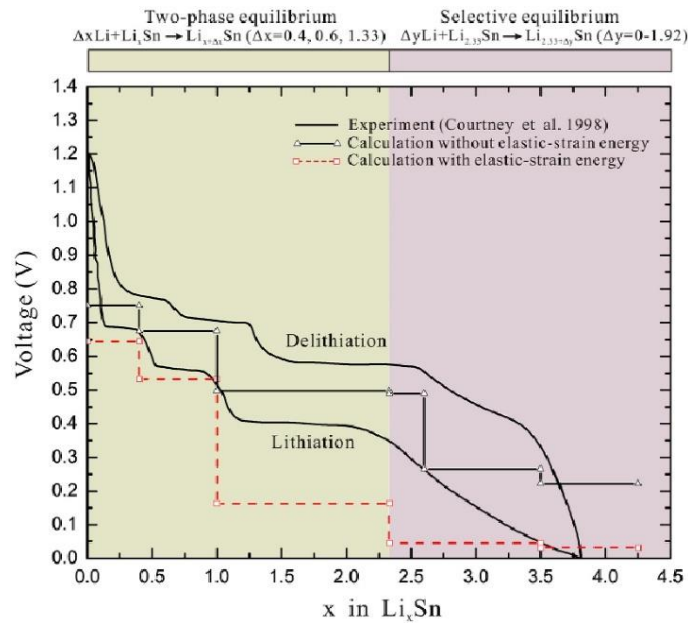
Figure 2.13 The change of voltage of Sn anodes during the lithiation and delithiation processes. The left part is the process of two-phase equilibrium, which shows a plateau for each lithiation reaction, while the right part is the selective equilibrium, in which the voltage decreases gradually upon lithiation [166].

Chapter 3

Basic theory and calculation method

3.1 Introduction

First-principles calculations (that is, ab-initio simulations) have been widely applied in the simulations of energy materials, semiconductor materials, metals, insulators and other solid materials. It treats the polyatomic system as a multiparticle system which is composed of atomic nuclei and electrons. Only five basic physical constants (e.g., Boltzmann's constant, Planck constant, electron energy, electron mass and the speed of light) are used in the whole theoretical method and no other empirical parameters are involved. Therefore, compared with other semi-empirical methods, first-principle calculations have more advantages in the strictness of the theoretical method and the objectivity of the results. First-principles calculations based on density functional theory (DFT) have significant merits in the field of material science. For example, it can predict the properties of materials and the possibilities of chemical reactions in the experimental preparation stage which reduces the tedious experimental attempts and the waste of materials and time. Secondly, through theoretical simulations, we can also reveal the physical mechanism behind the experimental phenomenon which is helpful to have an in-depth understanding of the observed macroscale phenomenon. Nowadays, ab-initio calculations have been widely used in material synthesis, optimization, explorations of material properties and many other aspects.

The core of quantum computation is to obtain the wave function (ψ) and energy (E) of a system by solving the Schrödinger equation and then further obtain the electronic structure of the atom. Since our study mainly involves the electronic energy levels of solid materials, it is only needed to consider the motion of particles that make up the solid materials in a constant potential field which does not evolve with time. In this potential field, the Hamiltonian operator (H) and ψ do not change with time.

Therefore, the distribution of particles in this space is independent of time. At this circumstance, H and ψ obey the time-independent, nonrelativistic Schrödinger equation:

$$H\psi = E\psi \ . \tag{3.1}$$

However, it is difficult to directly solve the Schrödinger equation. Thus, some approximate methods are used to convert the solution of the Schrödinger equation of a multi-electron system into those of a set of single-electron Schrödinger equations.

Born-Oppenheimer and Hartree-Fock approximations are two main approximations applied nowadays. Since the mass of a nucleus is more than 1800 times that of an electron, therefore, an electron can travel several orders of magnitude faster than a nucleus. When an electron is moving at a high speed, the nucleus only conducts thermal motion at its equilibrium position. However, when the position of the nucleus changes slightly, the electron can quickly adjust its motion status to reach a new equilibrium [197]. Based on this, Born-Oppenheimer approximation deals with the motions of the nucleus and electrons in a molecule separately [198]. The Hartree-Fock approximation averaged the Coulomb repulsion between electrons. Each electron is approximately regarded as moving in an average potential field created by the interaction of the nucleus and other electrons to this electron. The motion of each electron is only affected by the electron cloud of other electrons. Therefore, the motion status of an electron can be obtained by solving the single-electron Schrödinger equation [197]. In this way, the ψ with $3N$ variables for a system with N particles can be simplified to solve a single electron equation with three degrees of freedom. That is, the Hartree equation: $\sum_i H \psi = E\psi$ [199]. Unfortunately, the Hartree equation does not consider the case in which electrons are fermions. According to the antisymmetric principle, if two electrons exchange positions, the sign of their ψ will change, but exchanging places of two electrons does not change the sign of the Hartree product. Fock improved the Hartree equation and expressed the ψ of N electrons as the determinant of a matrix of single-electron wave functions [200]. For systems with

a small number of atoms, the Hartree-Fock method works well. However, for polyatomic systems, e.g., metallic Fermi levels and semiconductors, there will be a big deviation between the calculated results and the experimental results.

3.2 Density functional theory

First-principles calculations are established on the basis of DFT, which simplifies a complex many-body problem into a self-consistent single-particle model [201, 202]. DFT is developed based on Hohenberg–Kohn theorems and Kohn-Sham equations. Its basic idea is that the ground-state physical properties of atoms, molecules and solids can be expressed by DFT. The first Hohenberg-Kohn theorem proves that the ground-state energy from Schrödinger equation is a unique functional of the electron density, $\rho(\vec{r})$, in the identical fermion system without spin. That is, the ground-state $\rho(\vec{r})$ is the only factor that determines all properties [203]. This means that the Schrödinger equation can be solved by finding a function of 3 spatial variables, $\rho(\vec{r})$, instead of a function of $3N$ variables, $\psi(\vec{r})$. But this theorem does not give the concrete form of the functional. The second Hohenberg-Kohn theorem points out that the $\rho(\vec{r})$ that minimizes the energy of the overall functional is the true $\rho(\vec{r})$ which is the full solution the Schrödinger equation. Since the nondegenerate ground state is discussed here, the H of the multielectron system can be written as follows:

$$H = T + U + V \, . \tag{3.2}$$

The T, U and V are the kinetic energy of each electron, the interaction energy between different electrons, the interaction from the external field, respectively. The functional of the ground-state energy to the $\rho(\vec{r})$ for the multi-electronic system is

$$E[\rho] = T[\rho] + \int \rho(\vec{r}) V(\vec{r}) dr$$

$$+ \frac{1}{2} \iint d\vec{r} d\vec{r'} \frac{\rho(\vec{r}) - \rho(\vec{r'})}{|\vec{r} - \vec{r'}|} + E_{N-N} + E_{\text{xc}}(\rho) \, . \tag{3.3}$$

The terms on the right part are respectively the kinetic energy of electrons, the Coulomb interaction between the electrons and the nuclei, the Coulomb interaction

between pairs of electrons, the repulsive energies between the nuclei and the exchange-correlation functional. $E_{xc}(\rho)$ contains all the quantum mechanical effects that are not included in the first four terms. The Hohenberg-Kohn theorems show that the ground-state energy can be obtained by solving a simple electron density function. However, in order to obtain the $E[\rho]$, the $\rho(\vec{r})$, $T[\rho]$ and $E_{xc}(\rho)$ of the system also need to be determined.

To obtain the energy in the interacting electron system, Kohn and Sham proposed to replace the electron kinetic energies with known electron kinetic energies in the non-interacting system and the two systems have the same $\rho(\vec{r})$ which can be expressed by the ψ of N electrons:

$$\rho(\vec{r}) = \sum_{i=1}^{N} |\varphi_i(\vec{r})|^2 \ . \tag{3.4}$$

Then the electron kinetic energies can be written as:

$$T[\rho] = \sum_{i=1}^{N} \int d\vec{r} \varphi_i^*(\vec{r})(-\frac{1}{2}\nabla^2)\varphi_i(\vec{r}) \ . \tag{3.5}$$

Expressing the integral of $E[\rho]$ to ρ by the variation of $\psi_i(\vec{r})$ obtains the Kohn-Sham equation [204]:

$$[-\nabla^2 + V(\vec{r}) + V_H(\vec{r}) + V_{xc}(\vec{r})]\varphi_i(\vec{r}) = E_i\varphi_i(\vec{r}) \ , \tag{3.6}$$

where E_i is the Lagrange multiplier. The three potentials (V, V_H, V_{xc}) on the left side of the equation refers to, in order, the interaction between an electron and the collection of atomic nuclei, the Hartree potential and the exchange-correlation potential. The V_H is defined as the Coulomb repulsion between the electron be considering in one equation and the total electron density produced by all electrons in the system. It is expressed by:

$$V_H(\vec{r}) = e^2 \int \frac{\rho(\vec{r'})}{|\vec{r} - \vec{r'}|} d^3r' \ . \tag{3.7}$$

And $V_{xc}(\vec{r})$ can be written as

$$V_{xc}(\vec{r}) = \frac{\delta E_{xc}(\vec{r})}{\delta\rho(\vec{r})} \ . \tag{3.8}$$

The above discussion reveals that in order to solve the Kohn-Sham equation, we need to define the $V_H(\vec{r})$; to determine the $V_H(\vec{r})$, the $\rho(\vec{r})$ is needed, but to obtain the $\rho(\vec{r})$, we must know the $\psi_i(\vec{r})$. However, to get the single electron wave function $\psi_i(\vec{r})$, the Kohn-Sham equation needs to be solved. To break this circle, in the actual calculations, this problem can be solved by the following iterative algorithm: (1) partition the primitive cells of the multibody systems with enough grid points and define a set of initial, trial $\psi_i(\vec{r})$ at each grid point; (2) determine the initial electron density $\rho(\vec{r})$ based on the trial $\psi_i(\vec{r})$; (3) solve the Kohn-Sham equation to obtain the new single-electron functions, $\psi_{im+1}(\vec{r})$; (4) compare the newly obtained $\psi_{im+1}(\vec{r})$ and the initial $\psi_{im}(\vec{r})$. Usually, they are not the same. Then, modify the initial $\psi_{im}(\vec{r})$ by using the new $\psi_{im+1}(\vec{r})$ and repeat the above cycle from step 2 until the two $\psi_i(\vec{r})$ are the same. This process is called self-consistent. Further, the E, ρ and other properties of the system can be calculated by using the obtained $\psi_i(\vec{r})$.

Up to now, there is only one unknown part of DFT, that is, the specific form of $V_{xc}(\vec{r})$. Currently, the widely used $V_{xc}(\vec{r})$ are mainly local density approximation (LDA) and generalized gradient approximation (GGA). LDA is the simplest and most effective approximation in computational simulations, which assumes that the E_{xc} at a point in space is only related to the $\rho(\vec{r})$ of that point, and can be expressed by E_{xc}^{unif} of uniform electron gas of the same density [205]:

$$E_{xc}^{LDA}[\rho] = \int d\vec{r}\, \rho(\vec{r}) E_{xc}^{unif}(\rho(\vec{r})) \ . \tag{3.9}$$

The corresponding $V_{xc}(\vec{r})$ can be expressed as:

$$V_{xc}^{LDA}(\vec{r}) = \frac{\delta E_{xc}^{LDA}}{\delta\rho(\vec{r})} = E_{xc}[\rho(\vec{r})] + \rho(\vec{r})\frac{\partial E_{xc}(\rho)}{\partial\rho} \ . \tag{3.10}$$

For most calculations, LDA shows good accuracy. For example, the simulations of molecular bond lengths and crystal structures can reach an accuracy of 1%. For atomic ionization energy and molecular dissociation energy, the error is 10%−20% [206] However, LDA is not suitable for systems that are very different from uniform electron gases or electron gases that change slowly in space, for example, strongly correlated magnetic systems [207, 208].

The generalized gradient approximation (GGA) improves the LDA by considering the local gradient in the electron density [209]. The corresponding $E_{xc}(\rho)$ can be written as:

$$E_{xc}^{GGA}[\rho] = \int d\vec{r} f_{xc}(\rho(\vec{r}), |\nabla\rho(\vec{r})|) \ . \tag{3.11}$$

$E_{xc}^{GGA}(\rho)$ can be further expressed as a modified Becke functional [210, 211]:

$$E_{xc}^{GGA}[\rho] = E_{xc}^{LDA} - \beta \int d\vec{r} \rho^{\frac{4}{3}} \frac{(1 - 0.55 \exp[-1.65x^2])x^2 - 2.4 \times 10^4 x^4}{1 + 6\beta x \sinh^{-1}x + 1.08 \times 10^{-6}x^4} \ , \tag{3.12}$$

where $x = \dfrac{|\nabla\rho|}{\rho^{\frac{4}{3}}}$, β is a constant.

Compared with LDA, GGA greatly improves the accuracy of atomic exchange energy and correlation energy, but the ionization energy of valence electrons is rarely improved [197]. GGA contains more physical information than LDA, it should be more accurate. However, this is not always the case. There are many different types of GGA functionals according to the methods used to include the gradient information of electron density in the GGA functionals. Perdew-Wang (PW91) functional [212, 213] and Perdew-Burke-Ernzerhof (PBE) functional [210] are widely used in simulations involving solids. At present, the commonly used pseudopotential methods are plane-wave pseudopotential method, norm-conserving pseudopotential, ultra-soft pseudopotential and projector augmented-wave pseudopotential.

Plane-wave pseudopotential method: the valence electrons in the outer layers of the nucleus are chemically active and are significant in defining chemical bonding and other properties of materials which is of most interest in our calculations while the core electrons are less important. In general, the interaction between adjacent atoms has little effects on the state of core electrons but it largely influences the valence electrons. Therefore, the coordinate space of a polyatomic solid can be divided into two parts according to the different wave functions. Suppose there is a cutoff distance r_c, for the region within r_c (the core region), the wave function is consisting of the wave function of the tight-bound core electrons and there is almost no interaction between the wave functions of the adjacent atoms. The electron wave function outside

r_c (the valence electron wave function) will change due to the influence of other atoms. Therefore, based on the difference of interatomic interaction, the wave function of electrons can be treated approximately. The valence electron wave function outside r_c retains the shape of the real wave function, while the wave function inside r_c is replaced by the shape of a weak potential field. The resulting electron wave function is called a pseudo-wave function.

In addition, the Coulomb potential between nuclei and valence electrons and the equivalent repulsive effect from the core electrons to the valence electrons in the atomic potential are approximated as the effective potentials, which makes the pseudo-wave function become an eigenstate of atoms [197]. Thus, to solve the pseudo-wave function, a false potential energy is used to replace the real one. This false potential energy is called the pseudopotential, and the total system of the pseudopotential and pseudo-wave function is called the pseudo-atom. In fact, pseudo-atoms cannot accurately describe the internal properties of real atoms, but it is effective for dealing with the interaction between atoms. The accuracy of approximate calculations is mainly determined by the size of r_c. The larger r_c is, the smoother the pseudo-wave function, the greater the deviation from the real wave function and the greater the error will be. Conversely, the smaller r_c is, the closer to the real wave function and the more accurate the calculation will be.

The use of pseudo-atoms greatly reduces the plane-wave cutoff energy E_cut and the calculational burdens of the core regions and the whole systems. The amount of calculation is greatly affected by r_c. Because the smaller the r_c is, the more oscillations of the pseudo-wave functions are considered, and the more plane-wave expansion bases are needed, which leads to high calculational burdens. As a result, high accuracy and small computational burdens cannot be achieved at the same time. Compared with other high-precision first-principles calculations, the calculational burden of the plane-wave pseudopotential method is relatively low. Thus, it is suitable for complex systems which do not require high computational accuracy. According to

the different construction methods, pseudopotentials can be divided into the empirical pseudopotentials and ab initio atomic pseudopotentials. Before the 1980s, the empirical pseudopotentials were mainly applied to study the properties of metals, semiconductors and other materials. However, its application in different chemical environments is limited, and it can hardly deal with the systems which involve the charge transfer.

Norm-conserving pseudopotential: the wave function of norm-conserving pseudopotential (NCPP) has the same energy eigenvalues as those of the real potential [214]. In addition, the shape and amplitude of the wave function for valence electron are the same as those of the real wave function. In the core region, the wave function changes slowly and kinetic energy is relatively small. NCPP provides a correct description of $\rho(\vec{r})$ and it promotes the convergence of self-consistent calculations. After being proposed by Hamann *et al.* [214], the parameters of NCPP were further modified by Bachelet *et al.* [215] and a relatively complete pseudopotential was formed. NCPP had been continuously simplified under the premise of ensuring the accuracy of the calculation. The number of plane-wave bases was reduced as much as possible in order to reduce calculation burdens for the whole system. The required bases for pseudopotential calculations can be determined by the convergence of total energy to E_{cut}. The smaller the E_{cut} is, the softer the corresponding pseudopotential will be. Currently, NCPP has been improved to very soft, but it is still inferior to the commonly used ultra-soft pseudopotential (US-PP) when dealing with the nodeless valence electron clouds.

Ultra-soft pseudopotential: US-PP can make the wave function smoother and as soft as possible in the core region, which reduces the E_{cut} and the required plane-wave bases, thus improving the cost-performance ratio of calculations [216]. There is a small difference in the numerical evolutionary algorithm between US-PP and NCPP, but the approximate wave function of US-PP does not need to conform the norm-conserving approximation. It achieves the generalized norm-conserving condition by

41

using additional charges which further compensate the approximated localized electron cloud. This makes it possible to approximate the wave function of the nodeless valence electrons very smoothly. As a result, fewer plane-wave bases are needed in calculations which greatly improve the computational efficiency. Besides, it also expands the use range of USPP.

Projector augmented wave pseudopotential: in projector augmented wave (PAW) pseudopotential, the linear transformation is introduced to deal with the transformation from the pseudo-wave function to the full-electron wave function to generate the total energy function of PAW pseudopotential. This linear transformation is also used in the Kohn-Sham equation [217]. The treatment of additional charges in PAW pseudopotential is different from that of USPP. The PAW method only includes the full-electron wave function and the total electron pseudopotential but avoids the pseudopotential of additional charges, thus, it is relatively easy to establish the base of the pseudopotential. When US-PP method defines additional charges precisely, the simulation results obtained by using these two pseudopotentials are the same. PAW is an important complement to the pseudopotential methods.

3.3   A brief introduction to VASP

VASP (Vienna Ab-initio Simulation Package) is a widely used first-principles calculations software [218, 219]. It is based on the pseudopotential and projection-augmented plane-wave methods. It mainly uses the US-PP and PAW pseudopotentials to solve the interaction between electrons and ions. These pseudopotential methods have good universality of the calculation method and can reduce the calculational burden. Since it covers the pseudopotentials of most elements in the periodic table, so it is more versatile than the traditional NCPP. In addition, compared with other full electronic computing software (e.g., WIEN2K), the US-PP and PAW pseudopotentials can reduce the computational burdens at the promise of accuracy. The plane-wave method used in VASP can obtain accurate material properties by expanding the finite

electron wave function in the form of the plane-wave. The sets of plane-wave basis have the following three characteristics: (1) the uniform method is used to deal with the spatial lattice points and this method is not affected by the atomic position; (2) the mathematical expression of the arbitrary electron wave function is simple; (3) the accuracy of simulations can be improved by using high cutoff energy.

VASP is the most popular plane-wave computing software in the field of material science. It is widely used in DFT calculations of various materials, for example, it can simulate the properties of zero-dimensional clusters, atoms, molecules and even quantum dots, one-dimensional nanowires and nanotubes, two-dimensional thin films, surfaces, amorphous materials and three-dimensional solid materials under the periodic boundary conditions. First, it can optimize the crystal structures and then get the structural parameters (for example, bond lengths, bond angles, lattice constants, atomic positions, etc.) and basic mechanical properties (such as elastic constants, elastic moduli, brittle-ductile properties, anisotropies, etc.) of materials. Secondly, the electronic properties (such as energy band, electronic density of states, differential charge density, Bader charge analysis, etc.) can be revealed to show the types and strengths of chemical bonds in materials. In addition, VASP is also applied to calculate optical, magnetic and lattice dynamics properties, such as phonon spectrum. Compared with other quantum mechanics software, the advantages of VASP can be summarized as follows: (1) it equips with a complete and accurate pseudopotential library; (2) many optimizations have been done for the whole electronic self-consistent algorithm and the calculation process is stable; (3) the software can automatically judge the symmetry of the structures; (4) the parallel efficiency is high and the computation burden is small.

3.4 Calculation methods of mechanical properties

3.4.1 Structural optimization

For calculations of elastic constants of bulk Li_xSn alloys, LDA was used as the electron exchange-correction functional and the projected augmented wave method

was utilized to describe the ion-electron interaction [205, 219]. The kinetic energy cutoff for the plane-wave basis set is 500 eV and the Brillouin zone was sampled with the Monkhorst−Pack k-point grid [220]. In structural optimizations, all atoms were fully relaxed by using the conjugate gradient method until residual forces on constituent atoms were less than 5×10^{-2} eV/Å, and in determining mechanical properties, the value of convergent force increases to 1×10^{-3} eV/Å. The convergence tolerance for electronic relaxation was 10^{-6} eV and the total energy was calculated by the tetrahedron method coupled with Blöchl correction.

For all simulations in Chapter 5, 6 and 7, GGA was adopted as the electron exchange-correction functional [209]. The plane-wave energy cut-off of 380 eV and gamma centred k-meshes were used in calculations. Structural relaxation was carried out until the Hellmann-Feynman forces on constituent atoms were less than 0.01 (bulk and surface) and 0.05 (interface) eV/Å, respectively. Both atom positions and shapes were fully relaxed for bulk crystals. For the vacuum cells, atom positions were relaxed into the vacuum region above the interface without changing the cell shape and volume. Both atom positions and the cell length along the c-direction of the dense cell were optimized.

3.4.2 Elastic constants

By applying a small strain to the equilibrium lattice, the elastic constants, C_{ij}, in a crystalline system can be deduced from the change of its total energy with strain. The strain ε_{ij} has six independent components, and with the Voigt notation, they can be expressed as

$$\varepsilon_{ij} = \begin{pmatrix} e_1 & \frac{1}{2}e_6 & \frac{1}{2}e_5 \\ \frac{1}{2}e_6 & e_2 & \frac{1}{2}e_4 \\ \frac{1}{2}e_5 & \frac{1}{2}e_4 & e_3 \end{pmatrix}. \tag{3.13}$$

Under a small strain ε_{ij}, the relationship between the strain energy E and stress σ_{ij} is given by

$$\sigma_{ij} = \frac{1}{V_0}\left[\frac{\partial E(V,\varepsilon)}{\partial \varepsilon_{ij}}\right]_{\varepsilon=0} . \tag{3.14}$$

According to the Hooke law, $\sigma_{ij} = C_{ijkl}\varepsilon_{kl}$, the elastic constants can be identified as the second derivative of the total energy to strain, that is

$$C_{ijkl} = \frac{1}{V_0}\left[\frac{\partial^2 E(V,\varepsilon)}{\partial \varepsilon_{ij}\partial \varepsilon_{kl}}\right]_{\varepsilon=0} . \tag{3.15}$$

Here, the total energy of a crystal is expanded in the following Taylor form:

$$E(V,\varepsilon_{ij}) = E(V_0,0) + V_0\sum_{ij}\sigma_{ij}\varepsilon_{ij} + \frac{V_0}{2}\sum_{ijkl}C_{ijkl}\,\varepsilon_{ij}\varepsilon_{kl} + \ldots, \tag{3.16}$$

where V_0 is the volume of the unstrained system and $E(V_0,0)$ is the corresponding total energy.

Then, through selecting a specific strain $\varepsilon_{ij} = (e_1, e_2, e_3, e_4, e_5, e_6)$, we can determine the change of total energy before and after a set of different strains ($\leq \pm 2\%$, with an internal of 0.002) and the corresponding quadratic coefficients. According to the Voigt−Reuss−Hill approximation [221, 222], the isotropic elastic moduli of polycrystals can be calculated from the anisotropic C_{ij} of single crystals. The bulk (B) and shear (G) moduli can be calculated by

$$B_V = \frac{1}{9}(C_{11} + C_{22} + C_{33}) + \frac{2}{9}(C_{12} + C_{13} + C_{23}), \tag{3.17}$$

$$B_R = \frac{1}{(S_{11} + S_{22} + S_{33}) + 2(S_{12} + S_{13} + S_{23})}, \tag{3.18}$$

$$G_V = \frac{1}{15}(C_{11} + C_{22} + C_{33} - C_{12} - C_{13} - C_{23}) + \frac{1}{5}(C_{44} + C_{55} + C_{66}), \tag{3.19}$$

$$G_R = \frac{15}{4(S_{11} + S_{22} + S_{33}) - 4(S_{12} + S_{13} + S_{23}) + 3(S_{44} + S_{55} + S_{66})}, \tag{3.20}$$

where subscripts 'V' and 'R' indicate the Voigt and Reuss approximations, respectively, S_{ij} are the elastic compliance constants, i.e., the inverse matrix of elastic constants. Hill [222] proved that the elastic moduli of polycrystals can be obtained by calculating the arithmetic mean value of Voigt and Reuss values, that is, bulk modulus (B), shear modulus (G), Young's modulus (Y) and Poisson's ratio (v) of polycrystals can be

calculated from the following formula:

$$B = \frac{(B_V + B_R)}{2} \ , \tag{3.21}$$

$$G = \frac{(G_V + G_R)}{2} \ , \tag{3.22}$$

$$Y = \frac{9BG}{(3B + G)} \ , \tag{3.23}$$

$$v = \frac{(3B - 2G)}{2(3B + G)} \ . \tag{3.24}$$

3.4.3 Ideal tensile strength

The ideal tensile strength of a material is the minimum tensile stress required to make a defect-free crystal structure unstable. Here, the effects of defects, grain sizes and other factors on properties of a material are ignored and the strength of a material is explored from the perspective of internal chemical bonds and crystal structure. The ideal tensile strength provides the upper limit of the strength that a material can reach which is larger than the actual strength. Macroscopically, many factors such as defects, dislocations and grain boundaries will affect the tensile strength of a material to a great extent. Therefore, the macroscopic stress-strain curve should not be compared with the stress-strain curve calculated by first-principle calculations. However, the ideal strength is not an idealized concept. Previous studies have found that the ideal shear strength and ideal tensile strength can be obtained by nanoindentation test and metal whisker tensile test [223, 224]. Because the test area is very small in these experiments, the material can be considered to be in an ideal state without defects. For anisotropic materials, different maximum stress values are often obtained by applying strain along different directions. The minimum tensile strength and its direction are usually the most concerned parts of a study., because it corresponds to the easiest cleavage plane of a material. Besides, the ideal tensile strength can not only describe the hardness of a material, but also reflect the maximum stress required for fracture and phase transformation.

To obtain the ideal tensile strength of a material, it is necessary to obtain its stress-strain curve. The stress-strain relationships are determined by incrementally deforming lattice vectors in the applied strain direction. At each step, the applied tensile strain is fixed, while the atomic basis vectors orthogonal to strain and atoms inside the unit cell are simultaneously relaxed. At each strain step, the initial position is taken from the relaxed coordinates of a previous strain step. Failure of the interface was simulated by applying a uniaxial tensile strain along the c-axis of the symmetrical interface structure.

The engineering strain of tension is

$$l = (1 + \varepsilon)l_0 \ , \tag{3.25}$$

where l_0 and l are respectively the length of a material before and after stretching. Stress is the force per unit area, which can be expressed as

$$\sigma = \frac{F}{A} \ . \tag{3.26}$$

Since the force is the derivative of the energy to the length, that is,

$$F = \frac{\partial E}{\partial l} = \frac{1}{l_0} \frac{\partial E}{\partial \varepsilon} \ . \tag{3.27}$$

Combining Eqs (3.26) and (3.27), the stress can be obtained by

$$\sigma = \frac{1}{Al_0} \frac{\partial E}{\partial \varepsilon} = \frac{1 + \varepsilon}{V(\varepsilon)} \frac{\partial E}{\partial \varepsilon} \ . \tag{3.28}$$

Then, at each strain step, once the total energy and volume of the optimized structure are obtained, the stress can be calculated by Eq (3.28). Then, the stress-strain curve can be made according to the obtained stress. The corresponding value of the first local maximum stress is the ideal tensile strength in this direction.

3.4.4 Surface energy and interfacial properties

The stability of a surface is described by surface energy (γ_s) that is the energy required to cleave a surface from a bulk crystal. It is given by

$$\gamma_s = \frac{1}{2A}(E_{\text{unrelax}} - NE_b) + \frac{1}{A}(E_{\text{relax}} - E_{\text{unrelax}}) \ . \tag{3.29}$$

Here, E_{relax} and E_{unrelax} are the energies of the relaxed and unrelaxed surfaces, respectively. A is the area of the surface considered, N is the number of formula units

and E_b is the energy of one formula unit of bulk structure.

The interface strength is evaluated by the work of separation (W_{sep}), which is defined as

$$W_{sep} = \frac{(E_1 + E_2 - E_{12})}{A_i} \quad , \tag{3.30}$$

where E_{12} is the total energy of a relaxed Li_xSn/Cu interface system, E_1 and E_2 refer to the total energies of isolated upper and lower slabs in the same cell when one of them is kept and the other is replaced by vacuum, and A_i is the total interface area [44]. W_{sep} is the energy consumption per unit area in separating an interface into two fixed separate surfaces with the same atomic positions as the interface [225]. Then, each separate surface was relaxed into a free surface to obtain the adhesion energy W_{ad}, which is the energy gain per unit area to reversibly separate an interface into two free surfaces, neglecting plastic and diffusional degrees of freedom, that is

$$W_{ad} = \frac{(E_{1\text{-relax}} + E_{2\text{-relax}} - E_{12})}{A_i} \quad , \tag{3.31}$$

where $E_{1\text{-relax}}$ and $E_{2\text{-relax}}$ are the total energies of isolated upper and lower slabs in the same cells after relaxation. All the surface calculations were conducted in the same supercell as that for interfacial calculations.

The work of decohesion (W_{dec}) is defined as the energy difference (per unit surface area) between the fractured system and the interface structure at a zero-stress state, namely

$$W_{dec} = \frac{(E_{Frac} - E_0)}{2A_s} \quad , \tag{3.32}$$

where E_{Frac} and E_0 are the total energies of the fractured and the zero-stress state Li_xSn/Cu interfaces, respectively. A_s is the corresponding surface area. W_{dec} can be used to confirm the fracture location of interface structures. If $W_{dec} > W_{sep}$, fracture occurs at the interface, otherwise, it is energetically more favourable to fracture within the Li_xSn slab [225].

Chapter 4

Mechanical properties of Sn anode materials upon lithiation

Abstract

To obtain a better understanding of the failure mechanism of LIBs during charging-discharging, we have systematically studied the mechanical properties of Li_xSn alloys, including elastic constants such as the orientation-averaged bulk (B), shear (G) and Young's (Y) moduli, Poisson's ratios (ν), the anisotropy, brittleness-ductility, as well as ideal tensile strength. It is shown that B of Li_xSn alloys decrease almost linearly with the increase of Li concentration. However, the Y, G, ν and ideal tensile strength of Li_xSn alloys fluctuate with the Li concentration. Li_7Sn_3, Li_5Sn_2, $Li_{13}Sn_5$ and Li_7Sn_2 alloys show high Y and G due to their strong covalent hybridization. Through analysing the variations of mechanical properties upon lithiation, we explain the micromechanism for the poor cycle performance and crushing failure of Sn anode materials during charge-discharge cycles. Besides, electronic structures and chemical bonding have been elaborated to explain the change in mechanical properties.

4.1　Introduction

Sn anode materials undergo massive volume deformations and a series of phase transformations during charge-discharge processes. With the increase of Li content, a series of binary alloys (such as Li_2Sn_5, $LiSn$, Li_7Sn_3, Li_5Sn_2, $Li_{13}Sn_5$, Li_7Sn_2 and $Li_{17}Sn_4$) are gradually formed, and the colossal volume change causes large diffusion-induced stresses in electrode materials [66, 135]. This stress will lead to cracks on the surface of active materials, and further result in the fracture and pulverization of active materials in the subsequent charge-discharge cycles. The large stress may also cause the delamination of active materials from current collectors and the repeated fracture and regeneration of SEI films. This directly results in rapid capacity decay and poor cycle performance of LIBs [16, 124]. To improve the electrochemical performance of Sn anode materials, it is significant to have a deep understanding of its microscale failure mechanism.

The failure of electrode materials is closely related to their structural sizes and basic mechanical properties. Previous theoretical studies show that lithiation affects the mechanical properties of electrode materials. For example, the average change of Y in Li_xFePO4 during lithiation is less than 1% [226]. However, the Y values of crystalline and amorphous Li_xSi electrodes decrease almost linearly with the Li concentration, and the Y decreases to 1/3 when the $Li_{15}Si_4$ phase forms [93]. Therefore, lithiation-induced elastic softening is the microscopic physical mechanism of the failure of Si anodes.

In this chapter, by using first-principles calculations, we study the evolution of basic mechanical properties of Li_xSn alloys upon lithiation, such as B, G, Y, v, brittle-ductile properties, anisotropy and ideal tensile strength. In addition, the electronic structure and chemical bonding are also analysed to explain the changes in mechanical properties. Finally, combined with the calculated results and experimental research, we give the microscale mechanical failure mechanism of Sn anodes.

4.2 Electronic properties and chemical bonding of Li$_x$Sn alloys

The structural information of crystalline Li$_x$Sn phases obtained after relaxation is summarized in Table 4.1 and Figure 4.1, and for comparison, the available experimental values are also listed. Our results are well agreement with experimental data. From the structures, we can see that Sn−Sn bonds have been decreasing during lithiation while Li atoms play rising roles in the alloys. The Li−Sn bonds first increase with Li content, then decrease. The change of chemical bonds with Li content would result in the variation of mechanical properties of Li$_x$Sn alloys.
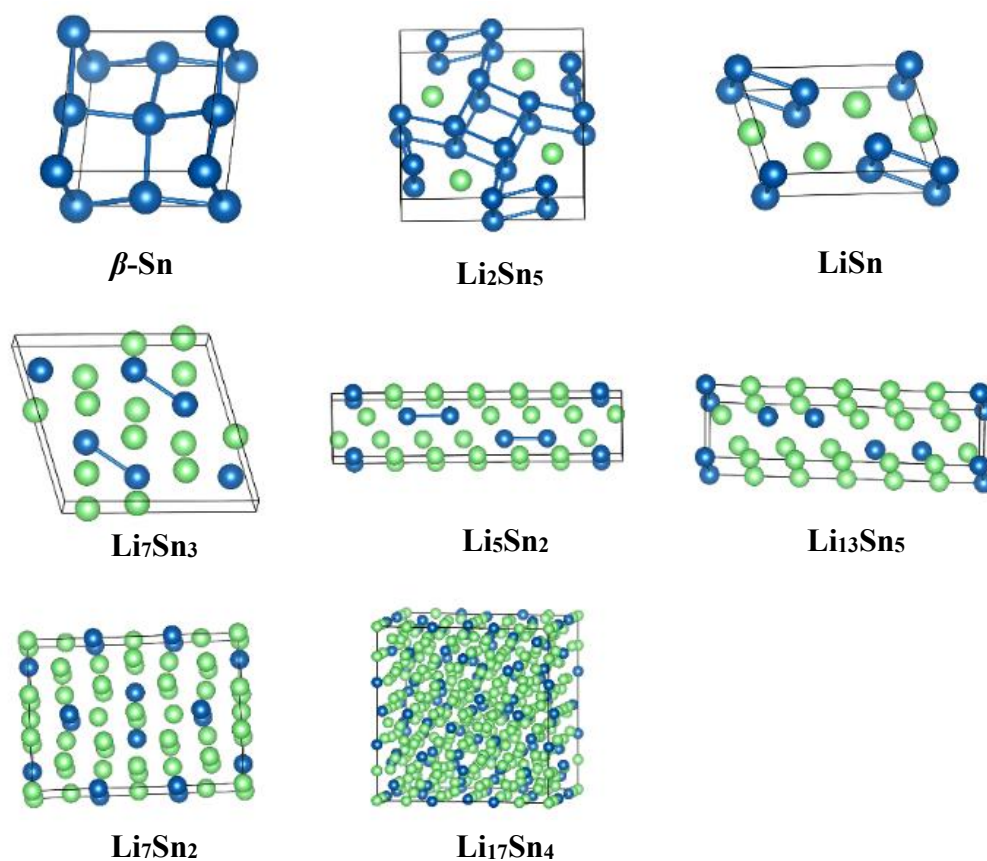
Figure 4.1 Crystal structures of Li$_x$Sn alloys after relaxation.

Table 4.1 Lattice constants in units of Å and k-points used in the calculation, where the experimental values are listed in parentheses [227-235].

Phase	Space group	x	y	a	b	c	k-points
β-Sn	$I4_1/amd$	0.00	0.00	5.792(5.831)	5.792(5.831)	3.122(3.184)	9×9×16
Li_2Sn_5	$P4/mbm$	0.40	0.29	10.331(10.274)	10.331(10.274)	3.169(3.125)	3×3×11
LiSn	$P2/m$	1.00	0.50	5.162(5.172)	7.764(7.742)	3.233(3.182)	7×10×4
Li_7Sn_3	$P2_1/m$	2.33	0.70	9.495(9.451)	8.536(8.561)	4.738(4.721)	4×7×4
Li_5Sn_2	$R\bar{3}m$	2.50	0.71	4.725(4.740)	4.725(4.740)	19.844(19.833)	8×8×2
$Li_{13}Sn_5$	$P\bar{3}m1$	2.60	0.72	4.703(4.701)	4.703(4.701)	17.130(17.124)	8×8×2
Li_7Sn_2	$Cmmm$	3.50	0.78	9.847(9.802)	13.838(13.803)	4.712(4.752)	3×2×7
$Li_{17}Sn_4$	$F\bar{4}3m$	4.25	0.81	19.670(19.690)	19.670(19.690)	19.670(19.690)	2×2×2

52

Based on optimized structures of Li_xSn alloys, electronic structures of Li_xSn alloys are explored. As shown in Figure 4.2, the finite values at Fermi levels (E_F) indicate the existence of metallic bonding which mainly comes from Sn $5p$ states and contains a little contribution of Sn $5s$ and Li s states. In $Li_{17}Sn_4$, the main contribution is from Li s states and Sn $5p$ levels. For pure Sn and Li_2Sn_5, the conduction band and valence band near E_F level are mainly contributed by Sn sp orbitals, with small contributions of Li s orbitals included in Li_2Sn_5. Upon lithiation, Li s orbitals play an increasing role. The covalent hybrid of Sn sp orbitals and Li s orbitals leads to the appearance of pseudo-gap (a sharp valley around E_F level), which directly reflects the covalency of Li–Sn bonds. With the continue of lithiation, covalent hybridization between Sn and Li atoms becomes more and more intense. The sharp peaks around E_F level in $Li_{13}Sn_5$ reflect that its covalent hybridization is the strongest among alloys, as shown in Figure 4.2(f).

With lithiation, the number of Li atoms increases gradually while that of Sn atoms decreases, which leads to weakened covalent hybridization between Sn and Li atoms. In $Li_{17}Sn_4$. Li atoms are the main component atoms, which make Li–Li metallic bonds become the dominate chemical bonds. The small content of Sn atoms causes the disappearance of pseudo-gap in $Li_{17}Sn_4$. Li_7Sn_3, Li_5Sn_2, $Li_{13}Sn_5$ and Li_7Sn_2 show a similar extent of covalent hybridization because of their minor difference of Li contents (~0.008−0.078), which further results in their similar mechanical properties. In addition, strong covalent hybridization will make them demonstrate higher Young's modulus, strength, melting point, hardness and brittleness [236].

For binary alloys, their stabilities have a strong correlation with the position of E_F in the DOS curve. If E_F falls on the pseudo-gap which separates bonding states from antibonding/nonbonding states in a structure, the system will be more stable. That is, stable structures tend to have low values at E_F [237]. From Figure 4.2, E_F falls in the pseudo-gaps of LiSn, Li_7Sn_3, Li_5Sn_2, $Li_{13}Sn_5$ and Li_7Sn_2 which suggests that all bonding states of these alloys are filled with electrons and all the antibonding states
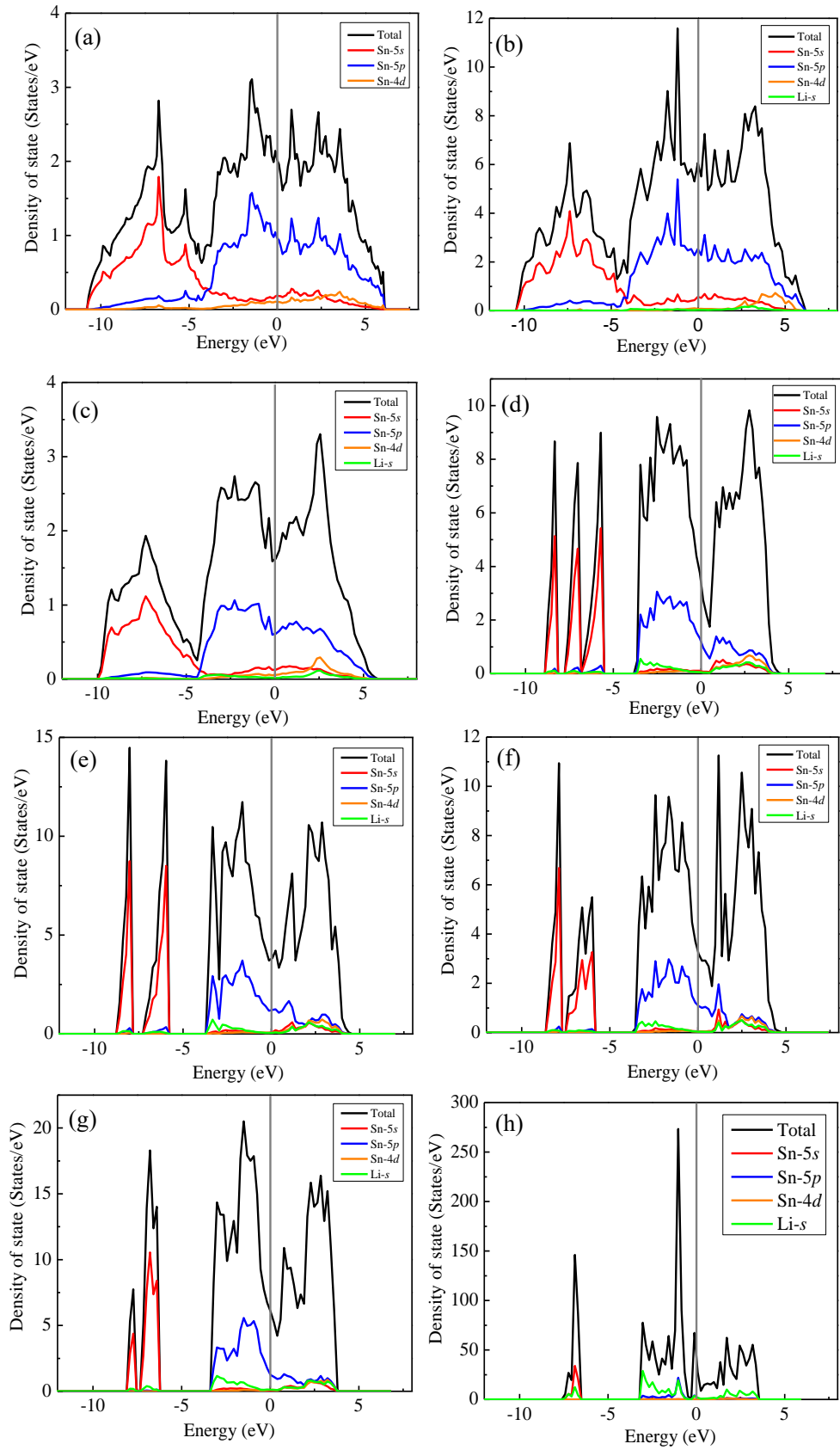
Figure 4.2 TDOS and PDOS of (a) β-Sn, (b) Li_2Sn_5, (c) LiSn, (d) Li_7Sn_3, (e) Li_5Sn_2,

(f) $Li_{13}Sn_5$, (g) Li_7Sn_2 and (h) $Li_{17}Sn_4$.

are left empty. The strong bonding effect would enhance the stability of these alloys. At high Li content, the bonding states of $Li_{17}Sn_4$ have been moved to lower energy and E_F falls on the peak of DOS curves which leads to the metastability of the system.

To have an in-depth understanding of the mechanical behaviours of Li_xSn alloys, we further unravel their chemical bonding by using Electron Localized Function (ELF) and Bader charge analysis [238, 239]. Bader charge results are summarized in Table 4.2. It is shown that in Li_xSn alloys, Li atoms lose electrons while Sn atoms obtain electrons which indicates their ionic bonding. Besides, upon lithiation, each Li atom donates fewer electrons to Sn atom. The average net charge of Li atom decreases with increasing Li content, dropping from 0.85 e (at Li content x of 0.40) to 0.81 e (x = 4.25). This suggests that each Sn can coordinate with more Li-ions which results in a higher Li/Sn ratio and weaker Li−Sn ionic bonds during the lithiation process.

Table 4.2 Average net charge of Sn and Li atoms in Li_xSn alloys.

	Average net charge (e)						
	Li_2Sn_5	LiSn	Li_7Sn_3	Li_5Sn_2	$Li_{13}Sn$	Li_7Sn_2	$Li_{17}Sn_4$
Sn	−0.34	−0.85	−1.94	−2.07	−2.15	−2.87	−3.46
Li	0.85	0.85	0.83	0.83	0.83	0.82	0.81

The values of ELF range from 0 to 1, with 1 representing localization such as covalent bonds, 0.5 corresponding to the electron-gas-like pair probability such as metallic bonds, and ELF = 0 indicates a high degree of delocalization [239]. As seen in Figure 4.3, there are mainly Sn−Sn metallic bonds in pure Sn. The ELF of LiSn, Li_5Sn_2 and Li_7Sn_2 show that with rising Li content, Sn−Sn metallic bonds gradually change into weak Li−Sn ionic bonds and Li−Li metallic bonds during lithiation. Combined with the results of electronic structure analysis, during lithiation, Sn−Sn metallic bonds will gradually transform into Li−Sn ionic-covalent bonds and Li−Li

metallic bonds, and the number of Li−Sn ionic-covalent bonds first increases and then decreases. Li−Li metallic bonds keep rising with lithiation. Besides, the ionicity of Li−Sn bonds decreases with increasing Li concentration while the covalency of Li−Sn bonds first increases and then decreases.
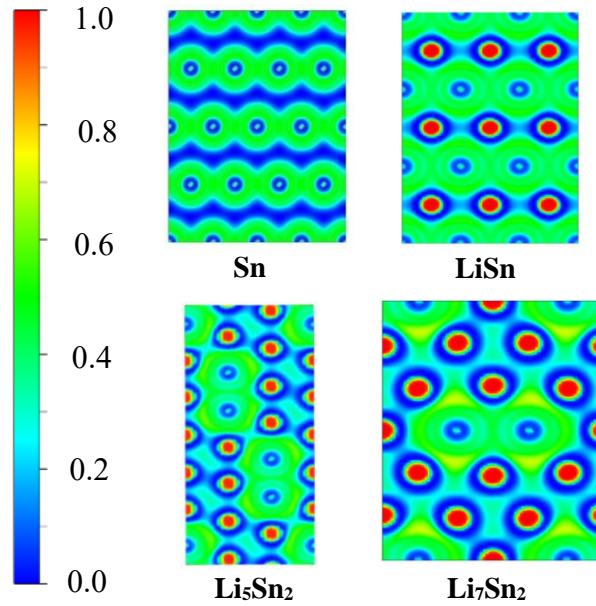
Figure 4.3 ELF of Li$_x$Sn alloys.

4.3 Influence of lithiation on elastic properties of Li$_x$Sn alloys

Different deformation modes are applied to obtain elastic constants (C_{ij}) of alloys [240]. The calculated C_{ij} are given in Table 4.3. For β-Sn, the calculated elastic constants are C_{11} = 77.92 GPa, C_{33} = 94.94 GPa, C_{44} = 20.38 GPa, C_{66} = 25.58 GPa, C_{12} = 55.70 GPa and C_{13} = 46.52 GPa, respectively, which are consistent with their corresponding experimental data, that is, C_{11} = 73.40 GPa, C_{33} = 90.70 GPa, C_{44} = 21.90 GPa, C_{66} = 25.82 GPa, C_{12} = 59.90 GPa and C_{13} = 39.10 GPa [241]. Based on calculated C_{ij}, the mechanical stabilities of alloys can be judged by using Born mechanical stability criterion [242]. The mechanical stability criteria for tetragonal (Sn

and Li$_2$Sn$_5$) and hexagonal systems (Li$_5$Sn$_2$ and Li$_{13}$Sn$_5$) is

$$C_{11} > |C_{12}|, 2C_{13}^2 < C_{33}(C_{11} + C_{12}), C_{44} > 0, C_{66} > 0 \,, \qquad (4.1)$$

and those of monoclinic (LiSn and Li$_7$Sn$_3$), orthorhombic (Li$_7$Sn$_2$) and cubic (Li$_{17}$Sn$_4$) systems are given in Eqs (4.2), (4.3) and (4.4):

$$C_{ij} > 0, i = j = 1{\sim}6$$

$$C_{11} + C_{22} + C_{33} + 2(C_{12} + C_{13} + C_{23}) > 0$$

$$C_{33}C_{55} - C_{35}^2 > 0, C_{44}C_{66} - C_{46}^2 > 0, C_{22} + C_{33} - 2C_{23} > 0$$

$$C_{22}(C_{33}C_{55} - C_{35}^2) + 2C_{23}C_{25}C_{35} - C_{23}^2C_{55} - C_{25}^2C_{33} > 0$$

$$g = C_{11}C_{22}C_{33} - C_{11}C_{23}^2 - C_{22}C_{13}^2 - C_{33}C_{12}^2 + 2C_{12}C_{13}C_{23}$$

$$2[C_{15}C_{25}(C_{33}C_{12} - C_{13}C_{23}) + C_{15}C_{35}(C_{22}C_{13} - C_{12}C_{23})$$

$$+ C_{25}C_{35}(C_{11}C_{23} - C_{12}C_{13})] - C_{15}^2(C_{22}C_{33} - C_{23}^2)$$

$$- C_{25}^2(C_{11}C_{33} - C_{13}^2) - C_{35}^2(C_{11}C_{22} - C_{12}^2) + C_{55}g > 0, \qquad (4.2)$$

$$C_{11} > 0, C_{11}C_{22} > C_{12}^2$$

$$C_{11}C_{22}C_{33} + 2C_{12}C_{13}C_{23} - C_{11}C_{23}^2 - C_{22}C_{13}^2 - C_{33}C_{12}^2 > 0$$

$$C_{44} > 0, C_{55} > 0, C_{66} > 0 \,, \qquad (4.3)$$

$$C_{11} - C_{12} > 0, C_{11} + 2C_{12} > 0, C_{44} > 0 \,. \qquad (4.4)$$

From Table 4.3, all elastic constants C_{ij} of Li$_x$Sn alloys meet Born stability criterion, thus they are mechanically stable. For Sn and Li$_2$Sn$_5$, their $C_{11} < C_{33}$ indicates that the incompressibility along the [001] direction is stronger than those along [100] and [010] directions which implies that the bond strength along the [001] direction is stronger than those along [100] and [010] directions. For most alloys, except that of LiSn, their [001] direction displays stronger incompressibility than those of [100] and [010] direction. For LiSn, its $C_{22} > C_{33}$ means that the [010] direction is more incompressible than that of [001] direction. $C_{11}+C_{12} > C_{33}$ can be observed in all alloys which suggests that the resistance to elastic deformation is higher in the (001) plane than along the c-axis. The varied C_{44} in alloys represent their different deformation resistant ability with respect to a shear deformation applied in the (100) plane along the [010] direction. Therefore, the different C_{ij} reflect the anisotropy of alloy phases.

57

Table 4.3 Elastic constants C_{ij} of Li$_x$Sn alloys, where all quantities are in units of GPa.

Phase	C_{11}	C_{22}	C_{33}	C_{44}	C_{55}	C_{66}	C_{12}	C_{13}	C_{23}	C_{15}	C_{25}	C_{35}	C_{46}
β-Sn	77.92	77.92	94.94	20.38	20.38	25.58	55.70	46.52	46.52	–	–	–	–
Li$_2$Sn$_5$	77.29	77.29	102.47	30.55	30.55	37.89	41.77	16.62	16.62	–	–	–	–
LiSn	57.70	87.36	58.42	16.20	15.20	17.35	14.96	26.56	21.32	−6.89	5.81	−3.04	1.03
Li$_7$Sn$_3$	56.26	76.17	80.53	10.26	37.20	35.48	18.00	18.03	−6.50	−14.92	9.81	8.97	11.42
Li$_5$Sn$_2$	74.81	74.81	109.89	17.66	17.66	30.36	14.08	−4.46	−4.46	–	–	–	–
Li$_{13}$Sn$_5$	75.12	75.12	101.15	20.11	20.11	31.34	12.45	−3.20	−3.20	–	–	–	–
Li$_7$Sn$_2$	53.53	63.83	74.23	10.62	33.38	35.23	19.74	11.20	−4.13	–	–	–	–
Li$_{17}$Sn$_4$	48.30	48.30	48.30	23.78	23.78	23.78	15.41	15.41	15.41	–	–	–	–
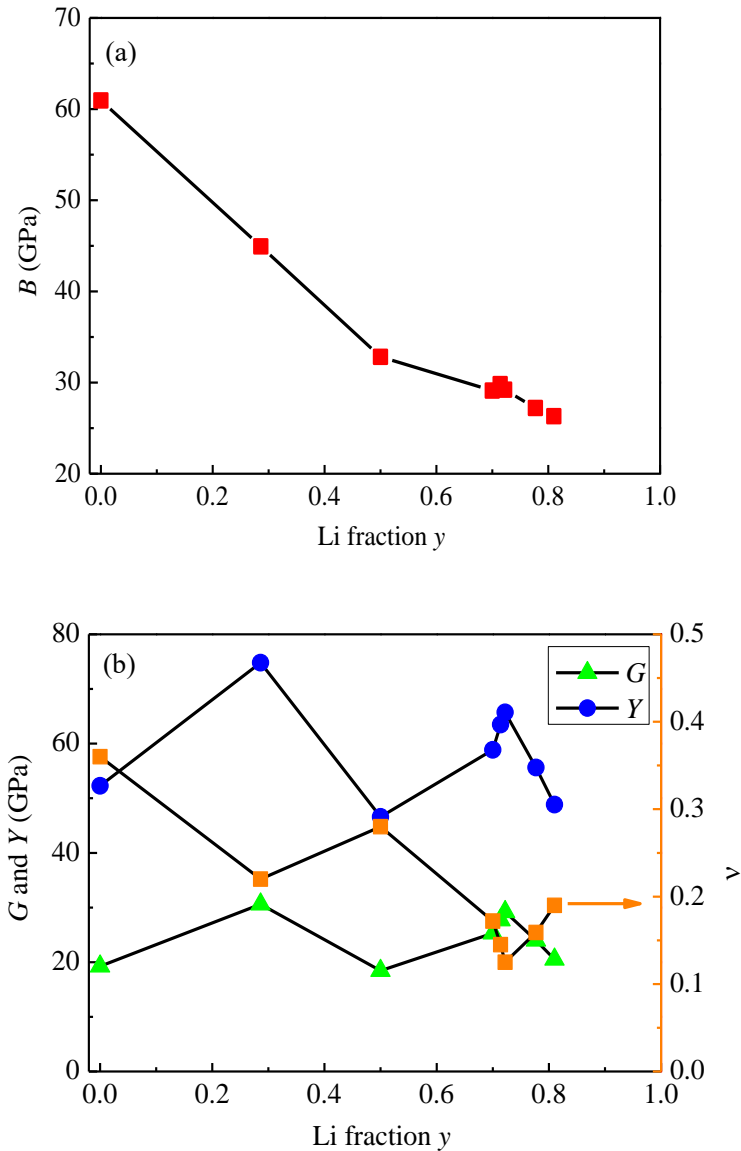
Figure 4.4 (a) B and (b) G, Y and ν of Li$_x$Sn alloys *versus* Li fraction y.

Based on these elastic constants, other mechanical parameters of Li$_x$Sn alloys, such as B, G, Y and ν, can be derived by using the Voigt−Reuss−Hill approximation [221]. The obtained Y of Sn agrees well with the experimental finding [243]. The orientation-averaged elastic moduli and ν for crystalline Li$_x$Sn phases are plotted in Figure 4.4. Here, the Li fraction y is defined as the ratio of Li atoms (x) in Li$_x$Sn alloys, i.e., $y = x/(1 + x)$. y is a dimensionless quantity with a range of 0−1, where $y = 0$ corresponds to metal Sn and $y = 1$ refers to the case where Li content x tends to be infinity. Figure 4.4 (a) shows that B decreases almost linearly with the increase of Li

concentration, which reveals a weakened resistant ability of Li_xSn alloys to volume compression. Microscopically, B mainly depends on the strength and compressibility of chemical bonds. In the early stage of lithiation, the decrease of B is mainly attributed to the weakening effect of Li−Sn polar covalent bonds on B, that is, the different electronegativity of the two bonding atoms in polar covalent bond results in the uneven distribution of valence electrons on chemical bonds, which reduces the resistance of chemical bonds to external pressure. In the late stage of lithiation, the decrease of B is mainly due to the weakened chemical bond strength of alloys [244].

Different from Li_xSi alloys [93], the Y, G and v of Li_xSn alloys fluctuate with Li content, which is due to the comprehensive effects of different chemical bonds in alloys. According to the change of chemical bonds in alloys, the lithiation process can be divided into four stages: (1) $x < 0.5$ (Sn and Li_2Sn_5), during this stage, Sn−Sn metallic bonds transfer into Li−Sn ionic-covalent bonds. The strong Li−Sn ionic-covalent bonds make Li_2Sn_5 show high Y and G; (2) $x = 0.5$(LiSn), the main chemical bonds in LiSn are Sn−Sn metallic bonds, Li−Sn ionic-covalent bonds and Li−Li metallic bonds, the increase of weak Li−Li metallic bonds and the decrease of Sn−Sn metallic bonds result in decreasing Y and G of LiSn; (3) $x = 2.33−2.6$ (Li_7Sn_3, Li_5Sn_2 and $Li_{13}Sn_5$), the transformation from Sn−Sn bonds to Li−Sn ionic-covalent bonds mainly takes place in this stage, as seen in the electronic structure analysis. This leads to increased average chemical bond strength, which further increases the Y and G of alloys. Because of the small change in Li content, the effect of Li−Li metallic bonds on Y and G is very small. The minor Li content also has a negligible effect on the ionicity of Li−Sn bonds; (4) $x = 3.5−4.25$ (Li_7Sn_2 and $Li_{17}Sn_4$), in this process, Li–Sn ionic-covalent bonds gradually transform into Li−Li metallic bonds, resulting in the weakening of the average chemical bond strength and the decrease of B, Y and G moduli of alloys. In addition, all v of alloys are larger than 1/8, suggesting that the resistance of all alloys to the change of bond lengths is stronger than that of bond angles [245].
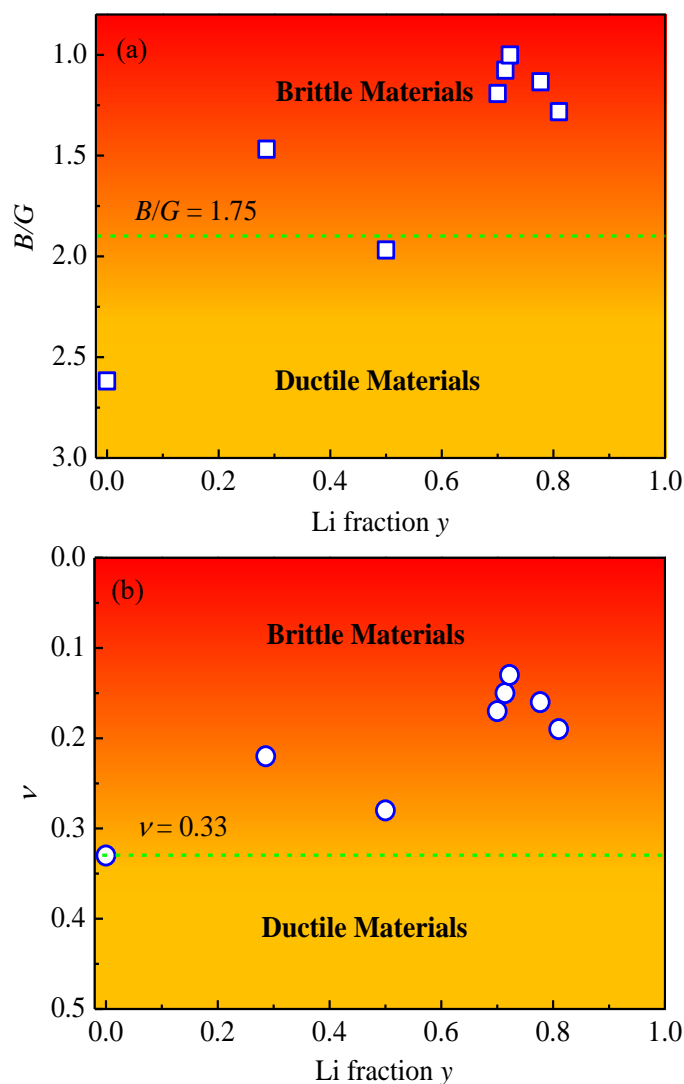
Figure 4.5 (a) B/G and (b) ν *versus* Li fraction y.

4.4 Ductility-brittleness transformation and anisotropy

According to the empirical Pugh formula [246], the B/G ratio can be adopted to distinguish the ductile and brittle behaviours of intermetallic and metalloid compounds. In the case of $B/G > 1.75$, a material behaves in a ductile manner, otherwise, it is brittle. Here, it is worth noting that, due to the over-simplification, the ductile to brittle transition value of 1.75 is not definitive. However, the B/G ratio can qualitatively describe the ductile-brittle transformation of electrode materials during lithiation. In addition, ν can also reveal the ductile and brittle properties. For ductile materials, their

v values are generally more than 1/3, while the v of brittle materials are less than 1/3. As seen in Figure 4.5, the B/G value of β-Sn is larger than 1.75 and its v is 1/3. Thus, Sn is ductile. Obviously, Li$_x$Sn alloys exhibit brittle properties because their B/G values are less than 1.75 and their v are less than 1/3. The brittleness of alloys is consistent with the evolution of Li−Sn ionic-covalent bonds.

Due to the anisotropy of active materials, micro-cracks can be induced during charge-discharge processes. To study the influence of anisotropy on their mechanical properties, we have calculated the elastic anisotropy of Li$_x$Sn alloys by using the universal anisotropy index A^U [247], that is

$$A^U = 5\frac{G_V}{G_R} + \frac{B_V}{G_R} - 6 \ . \tag{4.5}$$

As shown in Figure 4.6, at low Li content ($y < 0.70$), alloys show small anisotropies and their A^U increase slowly with increasing Li content, which is consistent with the approximately uniform expansion of Sn electrode particles observed in experiments at low Li content [248]. When $y > 0.70$, A^U fluctuates with rising Li concentration. Both Li$_7$Sn$_3$ and Li$_7$Sn$_2$ display high anisotropies while Li$_{17}$Sn$_4$ tends to be isotropic with A^U of 0.17. The large anisotropy difference of alloys also explains the uneven volume expansion of Sn microparticles in the late stage of lithiation [248].
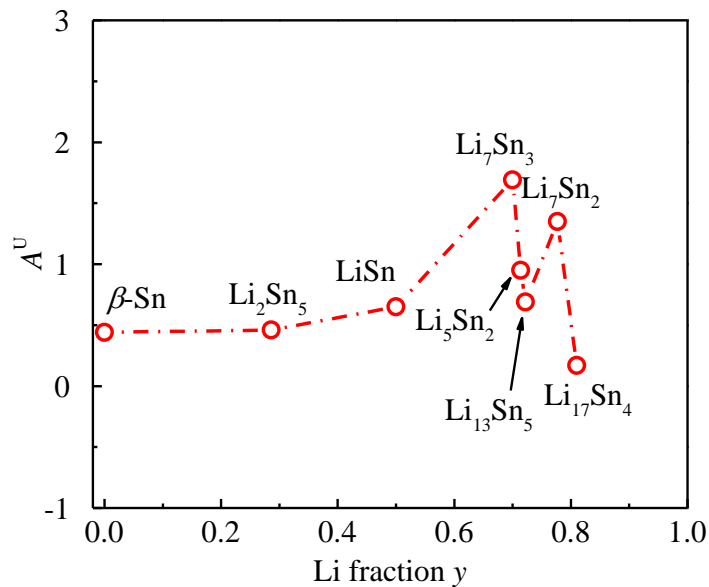
Figure 4.6 A^U of Li$_x$Sn alloys at different Li content.
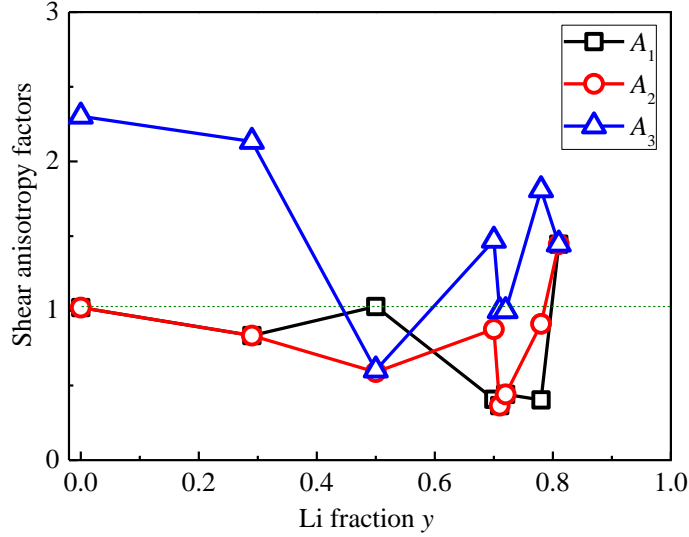
Figure 4.7 Shear anisotropy factors of Li$_x$Sn alloys.

Further, the shear anisotropies of Li$_x$Sn alloys in different planes have been analysed by using the following equations [249]:

$$A_1 = 4C_{44}/(C_{11} + C_{33} - 2C_{13}) \text{ , for (100) plane,} \tag{4.6}$$

$$A_2 = 4C_{55}/(C_{22} + C_{33} - 2C_{23}) \text{ , for (010) plane,} \tag{4.7}$$

$$A_3 = 4C_{66}/(C_{11} + C_{22} - 2C_{12}) \text{ , for (001) plane.} \tag{4.8}$$

For isotropic crystals, their A_1, A_2 and A_3 values equal to 1 while the values of anisotropy materials are lower or larger than 1. Figure 4.7 shows that the anisotropies of alloys in these three planes fluctuate largely at different Li content. Tetragonal Sn and Li$_2$Sn$_5$ demonstrate higher anisotropies in (001) plane than those of (100) and (010) planes. For monoclinic LiSn, it is isotropy in (100) plane while there are higher anisotropies in (010) and (001) planes. Comparing with LiSn, Li$_7$Sn$_3$ displays higher anisotropies in (100) and (001) planes while shows lower anisotropy in (010) plane. Li$_5$Sn$_2$ and Li$_{13}$Sn$_5$ show almost the same anisotropies in all three planes due to their same crystal system and similar chemical bonding, and they have larger anisotropies in (100) and (010) planes. As an orthorhombic crystal, Li$_7$Sn$_2$ has large anisotropies in (001) and (100) planes. By contrast, cubic Li$_{17}$Sn$_4$ displays same anisotropies in three planes. The varied anisotropies of Li$_x$Sn alloys make electrode materials vulnerable to cracks during the repeated lithiated/delithiated cycles.

63

4.5 Ideal tensile strengths of Li$_x$Sn alloys

Upon delithiation, electrode materials suffer from tensile stress which would cause the fracture of electrode materials. Therefore, we further explore the stress-strain behaviours of Li$_x$Sn alloys under tension. Here, the strain applied in different directions is determined by the strain of ideal tensile strength of a material. Because after reaching ideal tensile strength, the structure become unstable and phase transformation will occur, which will lead to the fluctuation of stress and make the following large stress unreachable. For example, Sn[100] shows a decrease of stress at the strain of 0.03, followed by a gradual increase in stress with the increase of strain (Figure 4.8(a)). Although Sn[100] exhibits high tensile stress under large strain, the ideal tensile strength of Sn[100] is defined as the first local maximum stress (1.12 GPa) at the strain of 0.02. This fluctuation of stress has been observed in many directions of Li$_x$Sn alloys, such as Li$_2$Sn$_5$[001], LiSn[001], Li$_7$Sn$_3$[001], Li$_5$Sn$_2$[$\bar{1}2\bar{1}0$] and Li$_{17}$Sn$_4$[111].

For tetragonal Sn and Li$_2$Sn$_5$, their stress-strain curves in [100], [001], [110] and [111] directions are given in Figures 4.8(a) and (b). Both Sn and Li$_2$Sn$_5$ exhibit strong stress responses in all directions. Their maximum tensile strengths (5.26 and 6.15 GPa) are in the [001] direction, while their ideal tensile strengths appear in the [100] direction and the ideal tensile strength of Li$_2$Sn$_5$(2.85 GPa) is higher than that (1.12 GPa) of Sn, which is attributed to the strong Li−Sn ionic-covalent bonds in Li$_2$Sn$_5$.

In the case of monoclinic LiSn and Li$_7$Sn$_3$ phases, their stress-strain curves in the [100], [010] and [001] directions are given in Figures 4.8(c) and (d). It is found that the ideal tensile strength (2.27 GPa) of LiSn at a strain of 0.05 in the [010] direction is higher than that (2.02 GPa) of Li$_7$Sn$_3$ at a strain of 0.03 in the [001] direction. Although Li$_7$Sn$_3$ demonstrates higher tensile stress in the following strain, the unstable structure makes it unreachable. The highest tensile strength of Li$_7$Sn$_3$ (7.67 GPa) is higher than that of LiSn (4.82 GPa), which reflects their anisotropies.
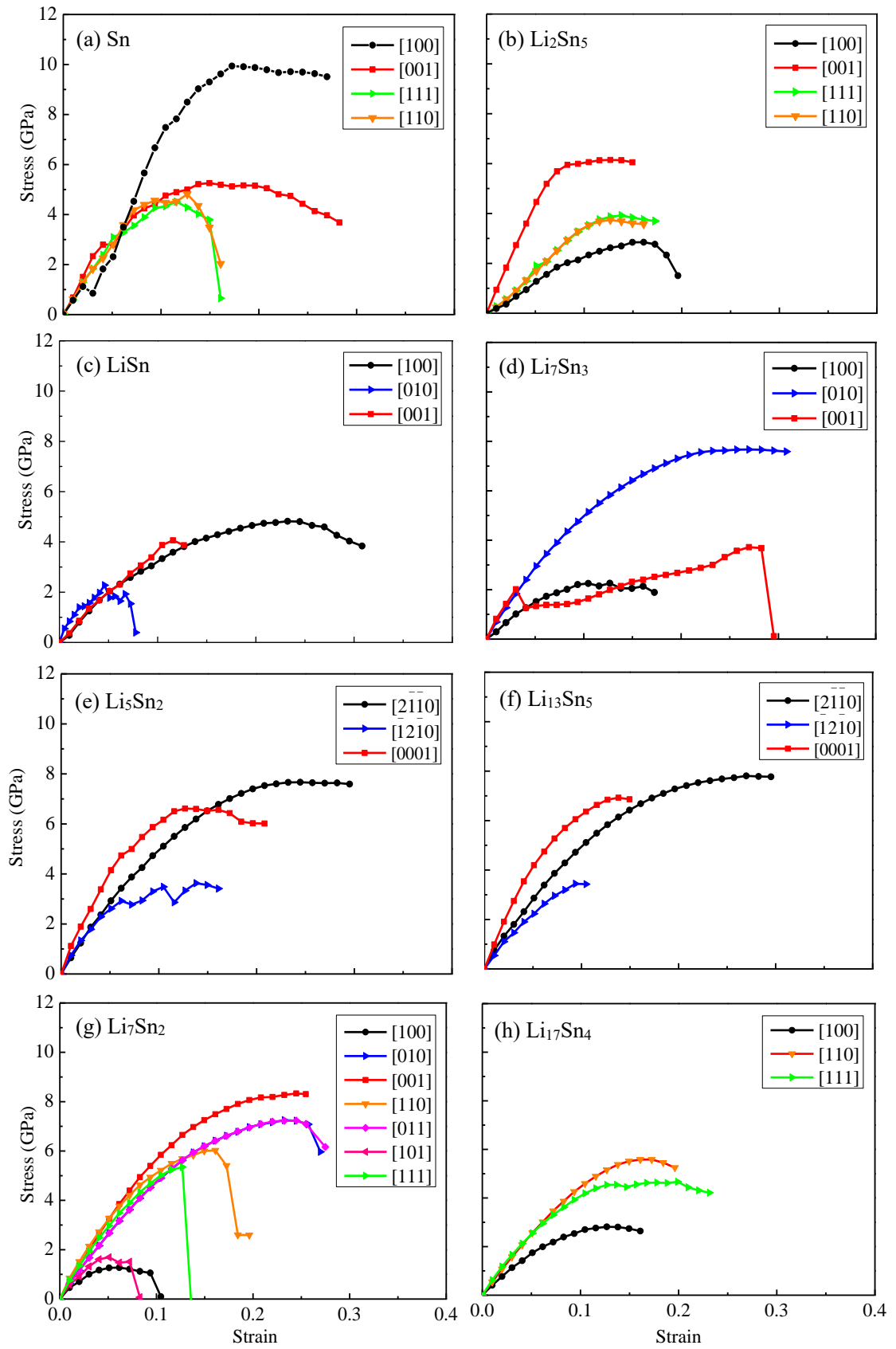
Figure 4.8 The stress-strain curves of Li$_x$Sn alloys.

Table 4.4 Ideal tensile strengths (GPa) of Li_xSn alloys and the corresponding strains and directions. The estimated strengths (GPa) are given as references.

Phases	Ideal tensile strength (strain)	Direction	Estimated strength
Sn	1.12 (0.02)	[100]	5.23
Li_2Sn_5	2.85 (0.16)	[100]	7.48
LiSn	2.27 (0.05)	[010]	4.73
Li_7Sn_3	2.02 (0.03)	[001]	5.93
Li_5Sn_2	2.92 (0.06)	$[\bar{1}2\bar{1}0]$	6.35
$Li_{13}Sn_5$	3.44 (0.09)	$[\bar{1}2\bar{1}0]$	6.57
Li_7Sn_2	1.27 (0.06)	[100]	5.56
$Li_{17}Sn_4$	2.81 (0.13)	[100]	4.88

In the case of hexagonal Li_5Sn_2 and $Li_{13}Sn_5$ phases, their ideal tensile strengths are calculated in three principal symmetry crystallographic directions. As shown in Figures 4.8(e) and (f), the ideal tensile strengths of Li_5Sn_2 are 7.67, 6.62, and 2.92 GPa in the $[2\bar{1}\bar{1}0]$, [0001] and $[\bar{1}2\bar{1}0]$ directions. The corresponding strengths of $Li_{13}Sn_5$ are 7.81, 6.92 and 3.44 GPa, respectively. Hence, Li_5Sn_2 and $Li_{13}Sn_5$ have similar ideal tensile strengths. Moreover, they display similar anisotropy ratios, with $[2\bar{1}\bar{1}0]:[0001]:[\bar{1}2\bar{1}0]$ of 2.63:2.27:1 and 2.27:2.01:1, respectively. From the stress-strain curves of orthorhombic Li_7Sn_2 and cubic $Li_{17}Sn_4$ phases (Figures 4.8(g) and (h)), both Li_7Sn_2 and $Li_{17}Sn_4$ exhibit strong stress responses in principal symmetry crystallographic directions with peak stresses between 1−9 and 2−6 GPa, respectively. The highest tensile stress of Li_7Sn_2 is 8.33 GPa in the [001] direction, which is higher than that (5.58 GPa) of $Li_{17}Sn_4$ in the [110] direction. Both of their ideal tensile strengths are along the [100] direction, indicating that Li_7Sn_2 and $Li_{17}Sn_4$ would fracture in the [100] direction with a tensile strength of 1.27 and 2.81 GPa, respectively.

The ideal tensile strengths of alloys are summarized in Table 4.4. In general, the strength of a material can be roughly estimated by $Y/10$. Therefore, according to the obtained elastic moduli, the estimated tensile strengths are given as references. Table 4.4 shows that the ideal tensile strengths of alloys fluctuate with the increase of Li content, ranging from 1.0 to 3.5 GPa. The large difference of ideal tensile strengths in different directions further reflects their large anisotropy.

In the charging processes, due to the embedding of Li-ions, electrode materials experience large volume expansion [250], which makes electrode materials suffer from compressive stress. The largely weakened bulk moduli, the ductile-brittle transformation and the large difference of anisotropies of alloys at high Li content will result in the appearance of cracks on the surface of lithiated electrode materials [128, 146, 183, 184]. In addition, since the lithiation and delithiation processes involve the diffusion of Li-ions in electrode materials, thus different parts of electrode materials may contain varied alloys, even at the same lithiation time. The various structures and mechanical properties (such as elastic moduli and stress-strain behaviours) of alloys, will cause large mismatch-induced stress due to the contact/interaction of different alloys in the interior of electrode materials. This will result in the cracking and disintegration of electrode materials [127, 146, 250]. In the discharging process, the volume of electrode materials shrinks due to the removals of Li-ions. In the meantime, the average stress upon electrode materials is tensile, which will promote the propagation of cracks from the external surface to the interior of electrode materials. As the charge-discharge processes continue, more cracks appear on the surface and in the interior of electrode materials, which eventually lead to the fracture and pulverization of electrode materials [128, 146, 183, 184]. This significantly affects the efficiency of active materials and cause degradation of cycle performance.

4.6 Conclusions

Based on first-principles calculations, we have systematically studied the Li concentration-dependent mechanical properties of Li$_x$Sn alloys. The results show that the bulk moduli of Li$_x$Sn alloys decrease almost linearly with increasing Li concentration, demonstrating that the resistant ability of Li$_x$Sn alloys to volume compression is weakened during the lithiation processes. The G, Y and v of Li$_x$Sn alloys fluctuate with the increase of Li content. The strong covalent hybridization of Li$_7$Sn$_3$, Li$_5$Sn$_2$, Li$_{13}$Sn$_5$ and Li$_7$Sn$_2$ leads to their high Y, G, as well as high brittleness. Besides, in the process of lithiation, Li$_x$Sn alloys go through a transformation from ductility to brittleness and they demonstrate various anisotropies and ideal tensile strengths. When Li content is less than 0.5, the anisotropy of alloys is small, and it increases slowly with Li content. But alloys show large anisotropy at high Li content. The ideal tensile strengths fluctuate with the increase of Li content, ranging from 1.0 to 3.5 GPa. The large difference in structures and mechanical properties of alloys will cause large mismatch-induced stress in the interior of electrode materials and make electrode materials vulnerable to cracking and fracture. The study of mechanical properties of Sn active materials deepens our understanding of the macroscopic failure behaviours of electrode materials during lithiation. The results provide important mechanical parameters for further simulating the stress evolution and mechanical failure behaviours under various coupling fields.

Chapter 5

Lithiation-induced interfacial failure of electrode-collector

Abstract

In this chapter, we investigate the interfacial failure between a lithiated Sn electrode and a Cu current collector for LIBs. The results show that segregation of Li-ions at the interfacial region causes the transformation of interfacial bonding from Sn–Cu to Li–Cu bonds, and weak Li–Sn bonds near the interface region. This leads to the weakened interfacial strength upon lithiation and failure of most lithiated Sn/Cu interfaces within Li_xSn slabs. Based on the simulation results and a linear elastic fracture theory, a diagram was constructed to determine the optimal dimension range of Sn–Cu core-shell electrodes. These findings highlight the interfacial failure mechanism of Sn anodes and provide a valuable guide to designing heterogeneous nanostructure electrodes for LIBs.

5.1   Introduction

Microcracking and debonding are two main types of structural damages caused by the insertion of Li-ions into active materials. By using *in-situ* observation, Chao *et al.* [10] revealed that cracks appear in lithiated layer of Sn particles during the first lithiation. Besides, Winter *et al.* [119] showed that the electrochemical lithiation of Sn caused surface cracks and local delamination of Sn active materials from Cu current collector, which eventually led to the loss of electronic contact (Figure 5.1). In addition, cracking and debonding of amorphous Si from Cu-foil substrate were observed during electrochemical cycling [251]. These directly lead to an early capacity loss and poor cycle performance. Thus, lithiation-induced microcracking and debonding of electrode materials pose a challenge to the application of Sn anodes in LIBs.

(a) After 2 cycles	(c) After 2 cycles
(b) After 5 cycles	(d) After 23 cycles
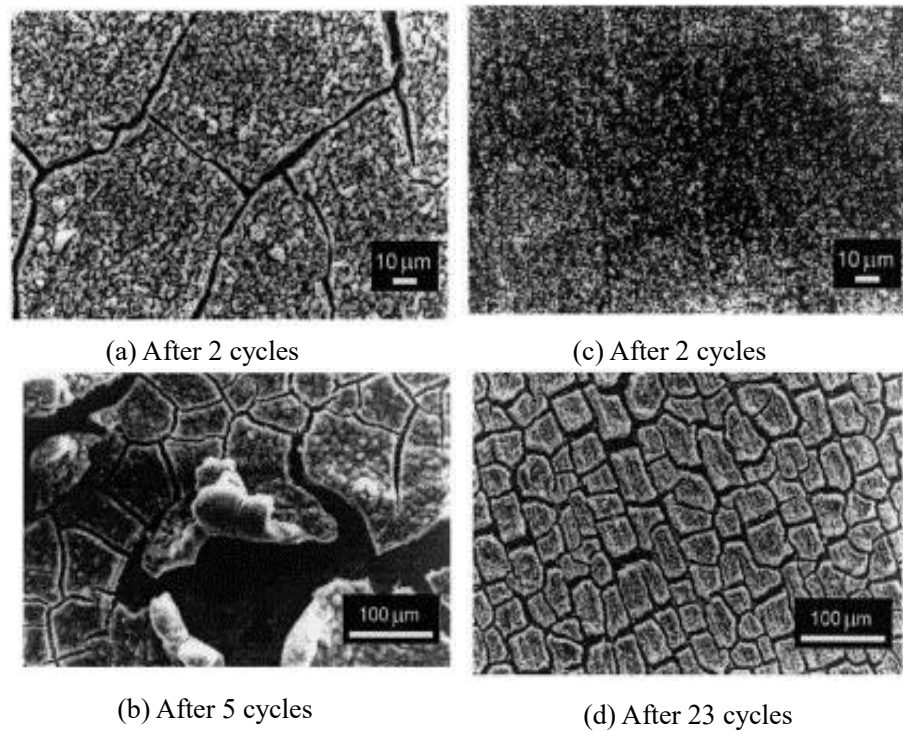
Figure 5.1 Scanning electron microscopy images of electroplated Sn on Cu substrate: (a-b) coarse (2–4 μm) and (c-d) fine (0.2–0.54 μm) Sn electrode particles after different cycles [119].

Previous microscopic investigations of Sn anodes were mainly focused on the failure mechanism of active materials during lithiation such as structures and phase

evolution of Li$_x$Sn alloys [120, 139, 181, 194, 195, 252], the change of mechanical properties [240, 253], as well as the diffusion of Li-ions in active materials [196, 254]. However, to the best of our knowledge, there are few studies on the failure mechanism of the electrode-collector interface at the atomic scale. Taking experimental difficulties into account, here we resort to atomistic simulations to attain some important interface information.

In this chapter, by using *ab initio* calculations, quantitative analysis is done to study the influence of lithiation on the interfacial properties of Sn anodes. Then, bonding analysis is conducted to explore the reason for the change of interfacial properties. Finally, based on the numerical results and a linear elastic fracture theory, a case study is conducted for Sn–Cu hollow core-shell spherical structures and the relationship between the critical sizes of the core and shell to avert fracture and debonding and the state of charge is determined. This work deepens our understanding of interfacial failure mechanism between Sn active materials and Cu current collectors and provides guidance for the design of nanocomposite architectures.

5.2 Surface properties of Li$_x$Sn alloys

To unveil the lithiation effect on interfacial properties of Sn anodes, four kinds of Li$_x$Sn alloys (Li$_2$Sn$_5$, LiSn, Li$_5$Sn$_2$ and Li$_7$Sn$_2$) and pure Sn are chosen with Li concentration x ranging from 0 to 3.5. For crystalline Li$_x$Sn and Cu, their optimized structural information is summarized in Table 5.1. The calculated lattice constant of Cu is 3.631 Å, which agrees well with the experimental value with the gap of less than 0.5%. The obtained lattice parameters of Sn also match well with experimental values.

To find the stable surfaces to form interface structures, surface energy convergence tests are carried out for several low-index planes of Li$_x$Sn phases by using a slab model. Based on the optimized bulk structures, the slab models are constructed with 5−9 atom layers depending on the degree of openness of the surfaces to ensure convergence in all cases. During optimization, the topmost 2−4 layers are relaxed,

71

Table 5.1 Li fraction y, lattice constants (Å), volume (Å^3) and k-points used in bulk calculations, where experimental values are listed in parentheses [139, 228, 229, 231, 233, 255].

Phase	y	a	b	c	Volume	k-points
β-Sn	0.00	5.941 (5.831)	5.941 (5.831)	3.208 (3.184)	113.21	9×9×16
Li$_2$Sn$_5$	0.29	10.386 (10.274)	10.386 (10.274)	3.141 (3.125)	338.80	5×5×16
LiSn	0.50	5.155 (5.172)	7.765 (7.742)	3.236 (3.182)	125.15	10×7×16
Li$_5$Sn$_2$	0.71	4.722 (4.740)	4.722 (4.740)	19.822 (19.833)	382.80	8×8×2
Li$_7$Sn$_2$	0.78	9.811 (9.802)	13.844 (13.803)	4.713 (4.752)	640.06	3×2×7
Cu	–	3.631 (3.615)	3.631 (3.615)	3.631 (3.615)	47.87	13×13×13

while the 2−3 bottom layers are fixed to mimic the bulk. A 15 Å vacuum layer is applied in the c-direction to avoid the interaction between upper and lower surfaces. Besides, the dipole correction is carried out to correct potential spurious terms arising from the asymmetry of slabs [256]. The surface energy (γ_s) of Cu(111) (1.40 J m^{-2}) is simulated to check the simulation method, which is consistent with the experimental result (1.83 J m^{-2}) [257]. Here, Cu(111) surface is chosen to form interfaces with Li$_x$Sn alloys [94, 258]. For Li$_x$Sn, considering the atomic densities in different planes and the lattice mismatches between the low-index planes of alloys and Cu(111), some planes are selected as more stable ones.
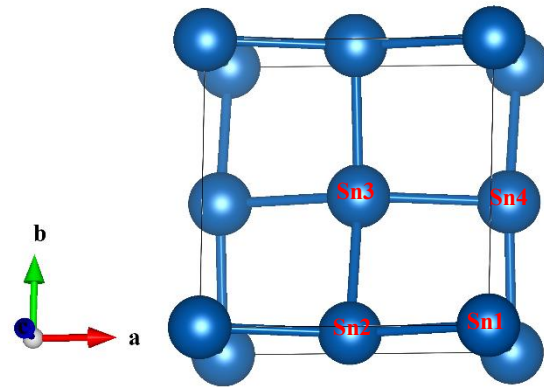
Figure 5.2 Crystal structure of β-Sn with four different Sn atoms.
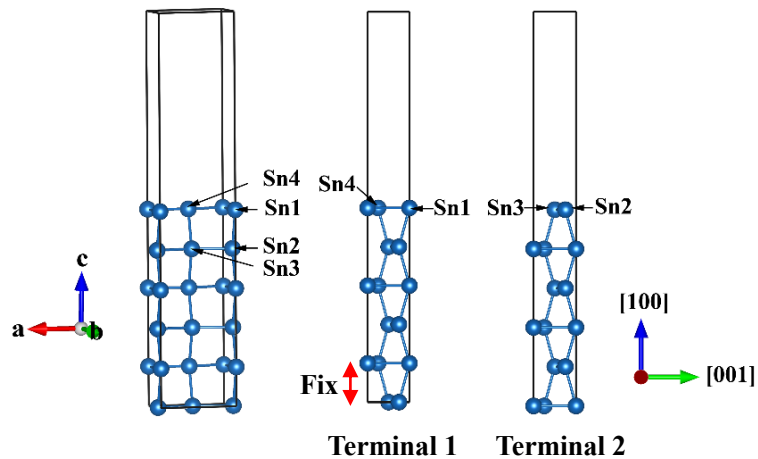
Figure 5.3 Atomic layer stacking of a Sn(100) slab and side views of (100) slabs with two different atom terminations.
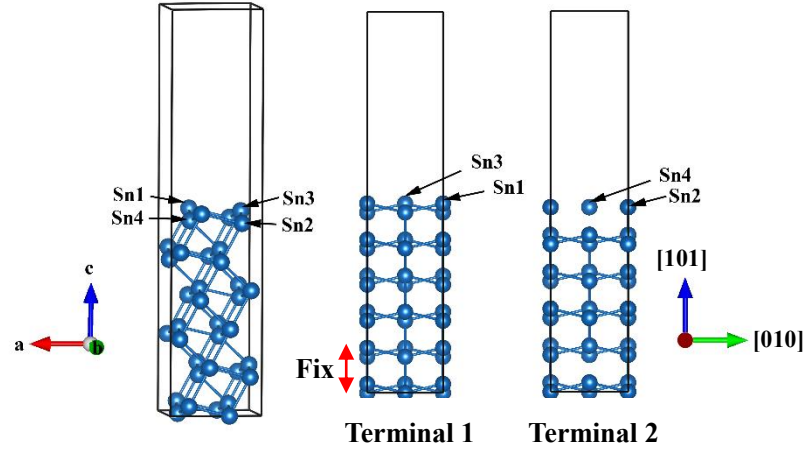
Figure 5.4 Atomic layer stacking of a Sn(101) slab and front views of (101) slabs with two different atom terminations.

β-Sn：According to the XRD data [259], surface energy test is done for (100), (101) and (110) planes of *β*-Sn. As seen in Figure 5.2, *β*-Sn has four different Sn atoms. Based on the periodic atomic layer stacking along [100] direction (Figure 5.3), there are two kinds of atom terminations for (100) surface, with terminal 1 containing Sn1 and Sn4 atoms and terminal 2 having Sn2 and Sn3 atoms. The γ_s of slabs with these two terminations are 0.41 and 0.42 J m^{-2}, thus atom terminations have little influence on the γ_s of (100). The difference of γ_s for models with twelve and fourteen formula units is ~0.01 J m^{-2}. That is, twelve formula units are enough to form a stable (100) surface. (101) surface has two different atom terminations, as shown in Figure 5.4. (101) slab with Sn3 and Sn1 atom termination demonstrates smaller γ_s (0.43 J m^{-2}) than that (0.45 J m^{-2}) of slab with Sn4 and Sn2 atom termination. For (110) surface, the γ_s of slabs with these two terminations are 0.47 and 0.48 J m^{-2}, respectively (see Figure 5.5). Thus, (100) has the lowest γ_s. Considering the largest interlayer spacing of (100) among all surfaces and the small lattice mismatch (1.87%) between *β*-Sn(100) and Cu(111), (100) is the most stable surface to form an interface with Cu current collector. The result is consistent with the experimental observation [259].

74
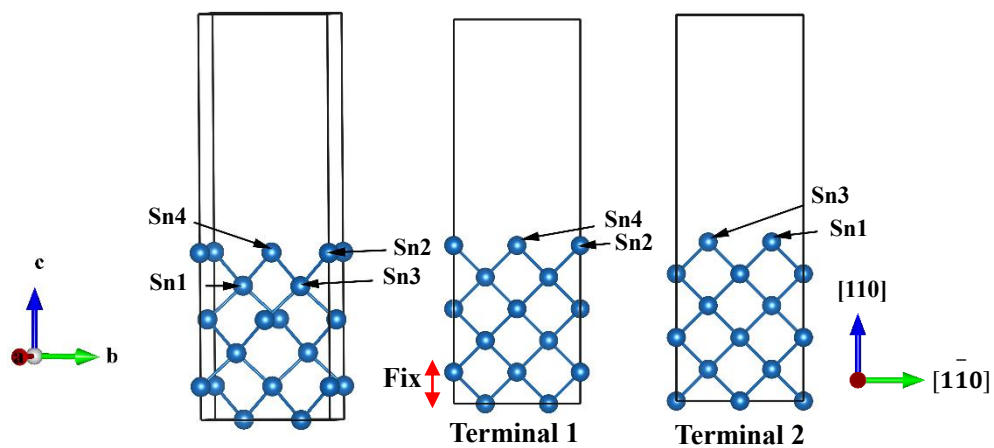
Figure 5.5 Atomic layer stacking of a Sn(110) slab and front views of (110) slabs with two different atom terminations.
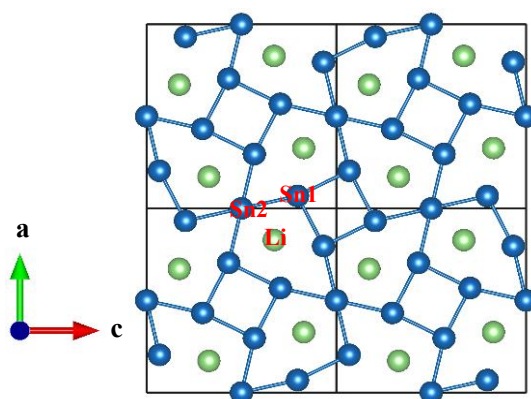
Figure 5.6 Li_2Sn_5 supercell with three different atoms.
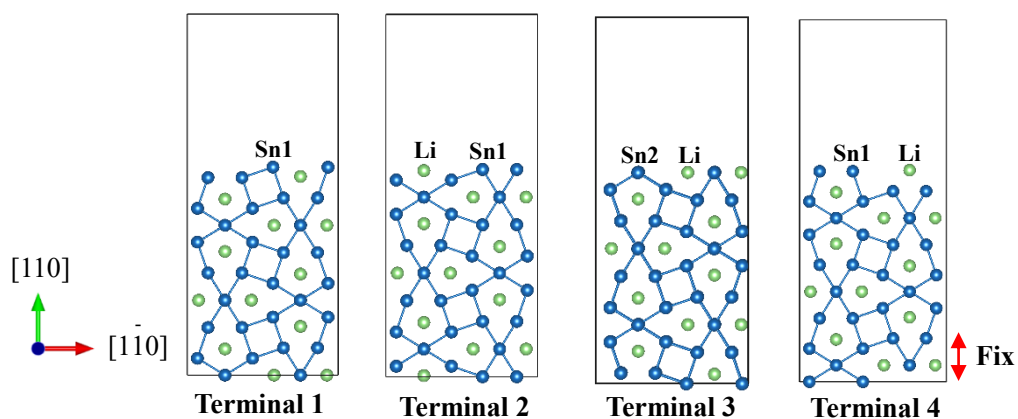
Figure 5.7 Li_2Sn_5(110) slabs with four different atom terminations.

Li$_2$Sn$_5$: There are five main planes (i.e., (100), (001), (110), (101), and (111)) in Li$_2$Sn$_5$. It is known that surface with a large interlayer spacing possesses a large surface atomic density, and the larger interlayer spacing is, the more stable the surface will be. Li$_2$Sn$_5$(100), (110) and (001) surfaces have much larger interlayer spacings (> 0.1 nm) than those (< 0.05 nm) of (101) and (111) surfaces. Thus, (100), (110) and (111) are more likely to be stable surfaces. Surface energy convergence test is conducted for these three surfaces. As shown in Figure 5.6, there are three different types of atoms (Sn1, Sn2 and Li) in Li$_2$Sn$_5$. Li$_2$Sn$_5$(110) surface has four different atom terminations based on the periodic atom arrangement along [110] direction (Figure 5.7). The results show that (110) slab with terminal 2 has smaller γ_s (0.35 J m^{-2}) than those of slabs with terminals 1, 3 and 4 (0.43, 0.42 and 0.48 J m^{-2}). Then, according to the thickness test of slabs with terminal 2, there is a little difference (~0.02 J m^{-2}) of γ_s between models with four and six formula units. That is, four formula units are enough to form a stable surface. The γ_s of these planes are summarized in Table 5.2.

The influence of atom terminals on γ_s of (100) and (001) is also considered (Figures 5.8 and 5.9). The γ_s of (100) slabs with the three atom terminations are 0.40, 0.43 and 0.42 J m^{-2}. The test is conducted with four formula units of Li$_2$Sn$_5$. Slab with terminal 1 is the most stable. The test of slab thickness shows that three formula units are required to form a stable surface. There is a small gap (0.01 J m^{-2}) of γ_s between slabs with three and four formula units. For (001) surface, the slab with Li atoms termination is more stable than that of Sn atoms termination. Their γ_s are 0.43 and 0.46 J m^{-2}, respectively. Thus, Li$_2$Sn$_5$(110) with terminal 2 has the lowest γ_s. Moreover, (110) has smaller lattice mismatch (3.00%) with Cu(111) than those (3.30% and 4.78%) of (111) and (100) surfaces. Thus, (110) surface with terminal 2 is energetically favourable to form a stable interface with Cu current collector.

Table 5.2 Surface energies (γ_s) of main low-index planes of Li$_x$Sn alloys. The corresponding thickness is shown by the number of Li$_x$Sn formula units in a slab model.

Phase	Plane	Number of formula units	γ_s (J m^{-2})
	(100)	12	0.41
Sn	(101)	16	0.43
	(110)	10	0.47
	(100)	3	0.40
Li$_2$Sn$_5$	(001)	8	0.43
	(110)	4	0.35
	(100)	6	0.45
LiSn	(010)	9	0.54
	(001)	6	0.41
	(0001)	3	0.48
	($10\bar{1}0$)	6	0.74
Li$_5$Sn$_2$	($2\bar{1}\bar{1}0$)	4	0.79
	($11\bar{2}0$)	8	0.59
	($\bar{1}2\bar{1}0$)	9	0.67
	(100)	4	0.75
	(010)	4	0.63
	(001)	12	0.69
Li$_7$Sn$_2$	(110)	4	0.78
	(011)	8	0.72
	(111)	8	0.75
	(101)	8	0.80
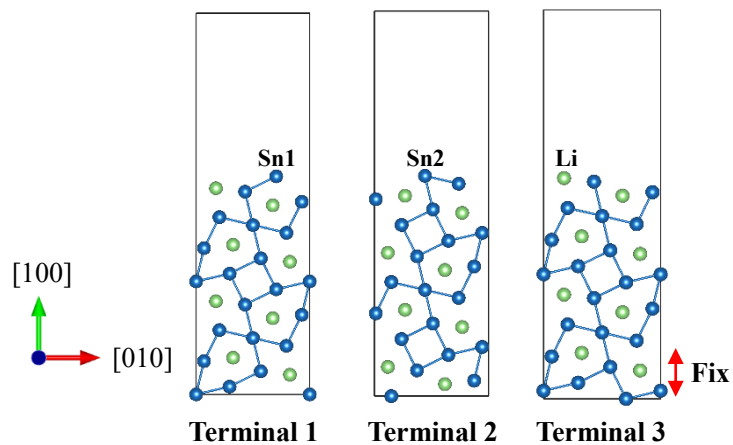
Figure 5.8 Li$_2$Sn$_5$(100) slabs with three different atom terminations.
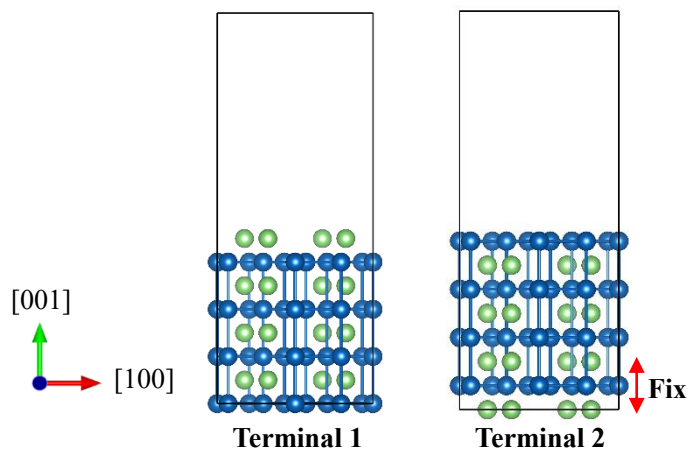
Figure 5.9 Li$_2$Sn$_5$(001) slabs with two different terminations.
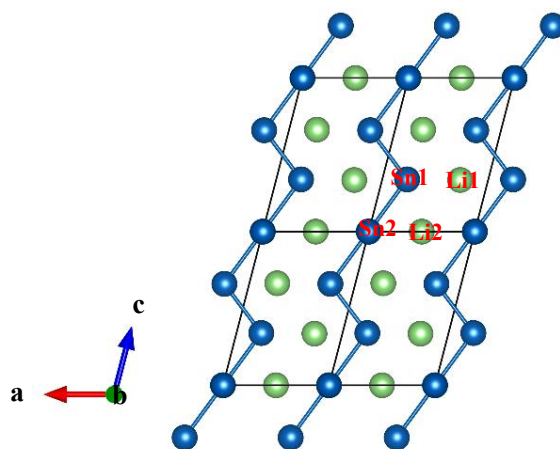
Figure 5.10 LiSn supercell with four different atoms.
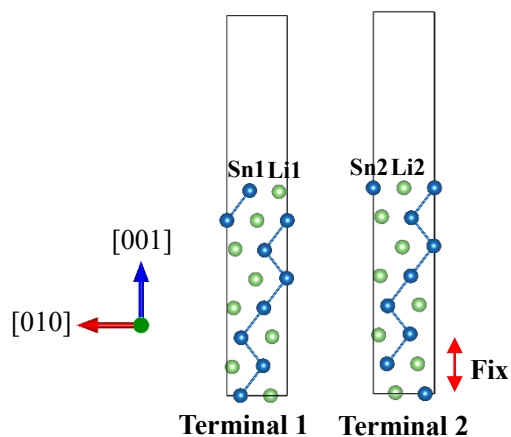
Figure 5.11 Atomic layer stacking of LiSn(001) slabs with two different terminations.
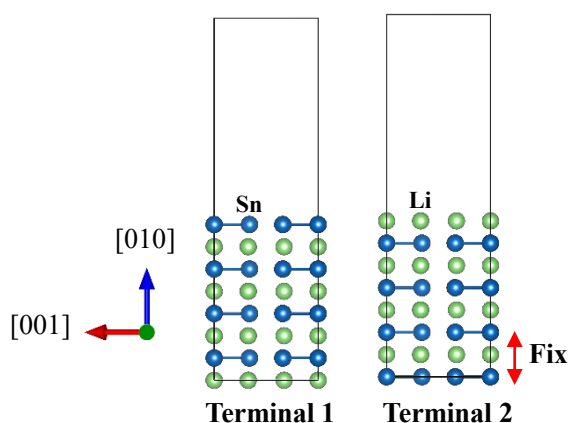
Figure 5.12 Atomic layer stacking of LiSn(010) slabs with two different terminations.

LiSn: (100), (010) and (001) are the main low-index planes of LiSn. As seen in Figure 5.10, LiSn has four different atoms (Sn1, Sn2, Li1 and Li2). According to the atomic layer arrangement along [001] direction, (001) surface has two different atom terminations (see Figure 5.11). The γ_s of these two slabs are 0.43 and 0.45 J m^{-2}. Test of slab thickness of slabs with terminal 1 shows that the γ_s of slabs with six and seven formula units are 0.41 and 0.42 J m^{-2}, respectively. Thus, a slab with six formula units could form a stable surface. Likewise, there are two atom terminations in (010) surface with γ_s of 0.61 and 0.54 J m^{-2} (Figure 5.12). As illustrated in Figure 5.13, (100) surface has four different atom terminations and slab with terminal 4 (Li2 atoms) displays the lowest γ_s (0.45 J m^{-2}). The γ_s of slabs with terminal 1, 2 and 3 are 0.51,

0.58 and 0.62 J m^{-2}, respectively. Thus, (001) surface with terminal 1 demonstrates the lowest γ_s. Considering the lattice mismatches of these three surfaces ((001), (010), (100)) with Cu(111) (1.15%, 1.15% and 1.29%, respectively), LiSn(001)/Cu(111) interface should be the most stable one.
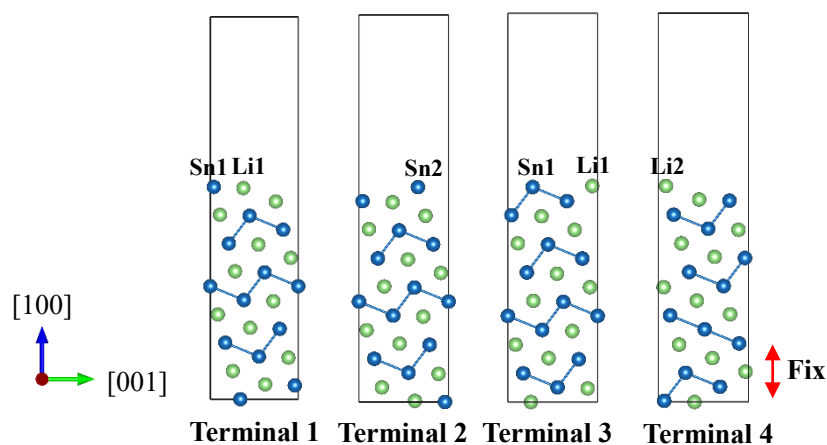
Figure 5.13 Atomic layer stacking of LiSn(100) slabs with four different terminations.

Li$_5$Sn$_2$: As a hexagonal structure, (0001) is the stable surface of Li$_5$Sn$_2$ and it has seven kinds of atom terminations, as shown in Figure 5.14. The γ_s of slabs with these seven terminations are 1.04, 0.77, 0.48, 0.54, 0.87, 0.89 and 0.72 J m^{-2}, respectively (see Figure 5.15). Test of slab thickness shows that three formula units are enough to form a stable surface. Using the same method, the γ_s of other low-index planes of Li$_5$Sn$_2$ are also studied. The γ_s of $(2\bar{1}\bar{1}0)$, $(11\bar{2}0)$, $(10\bar{1}0)$ and $(\bar{1}2\bar{1}0)$ are 0.79, 0.59, 0.74 and 0.67 J m^{-2}, respectively. Thus, (0001) surface with Li2 atom termination displays the lowest γ_s. Besides, (0001) surface has the lowest lattice mismatch with Cu(111) with a small value of 1.57%. The lattice mismatches between other surfaces and Cu(111) are in the range of 2.03%–3.15%. Considering the γ_s and lattice mismatch, it is energetically favourable for (0001) surface with Li2 atom termination and Cu(111) to form an interface.
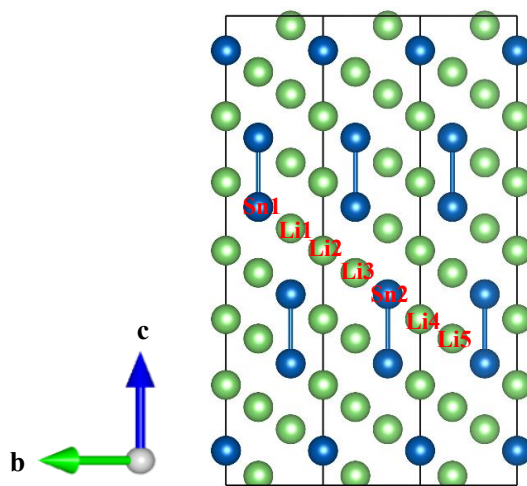
Figure 5.14 Li$_5$Sn$_2$ supercell with seven different atoms.
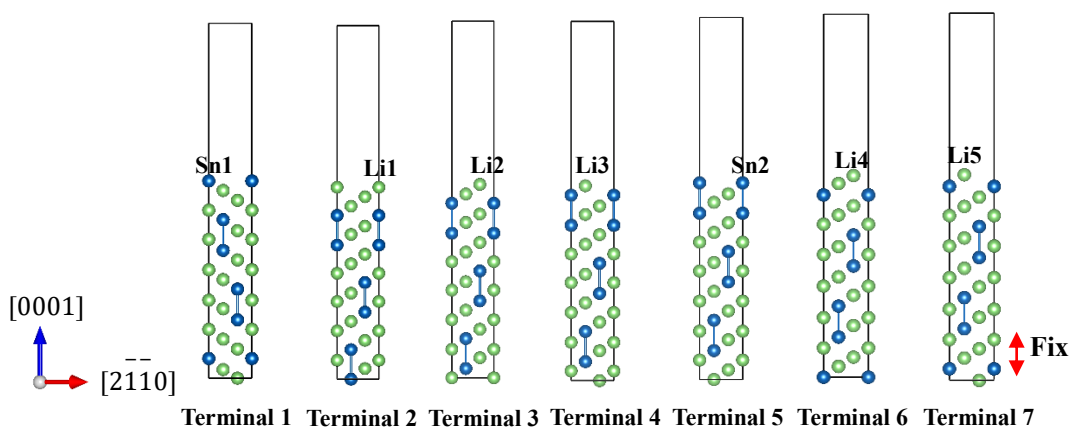
Figure 5.15 Atomic layer stacking of Li$_5$Sn$_2$(0001) with different atom terminations.

Li$_7$Sn$_2$: There are seven main planes for Li$_7$Sn$_2$ ((100), (010), (001), (110), (101), (011) and (111)). Since the interlayer spacings of (100), (010) and (001) surface (0.16, 0.23 and 0.24 nm) are much larger than those of the other four surfaces (< 0.14 nm). (100), (010) and (001) are more likely to be stable surfaces. As seen in Figure 5.16, there are two atom terminations for (001) surface with γ_s of 0.72 and 0.69 J m^{-2}, respectively. For (010) surface, the γ_s of the slabs with the two atom terminations are 0.67 and 0.63 J m^{-2} (Figure 5.17). Likewise, based on the periodic atom arrangements along [100] direction, (100) surface has two terminations (see Figure 5.18). The calculated γ_s are 0.75 and 0.80 J m^{-2}, respectively. Besides, the γ_s of (110), (101),

(011) and (111) are also calculated, which are 0.78, 0.80, 0.72 and 0.75 J m^{-2}, respectively. From the above results of Li$_7$Sn$_2$, (010) surface with terminal 2 has the lowest γ_s (0.63 J m^{-2}), a little smaller than that of (001) (0.69 J m^{-2}). Since (001) has the largest interplanar spacing among all planes and it has smaller lattice mismatch (2.77%) with Cu (111) than that (3.44%) of (010) surface. Thus, (001) with terminal 2 might form a stable interface with Cu. Through comparing the work of separation (W_{sep}) (0.45 and 1.70 J m^{-2}) of Li$_7$Sn$_2$(010)/Cu(111) and Li$_7$Sn$_2$(001)/Cu(111) interfaces, Li$_7$Sn$_2$(001)/Cu(111) is the most stable interface. The γ_s of main low-index planes of Li$_x$Sn alloys are shown in Table 5.2.
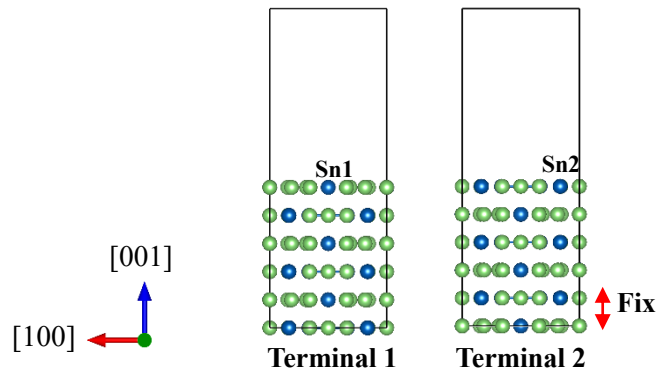
Figure 5.16 Atomic layer stacking of Li$_7$Sn$_2$(001) with two atom terminations.
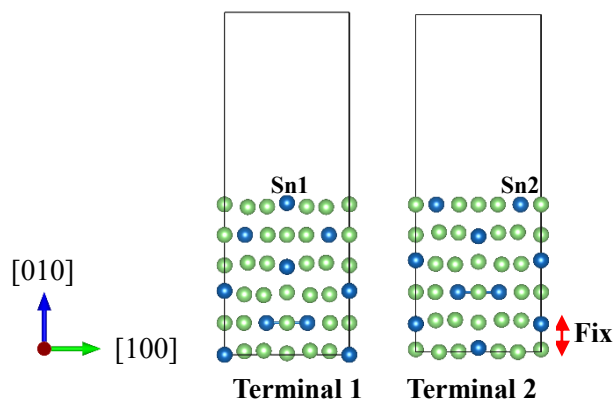
Figure 5.17 Atomic layer stacking of Li$_7$Sn$_2$(010) with two atom terminations.
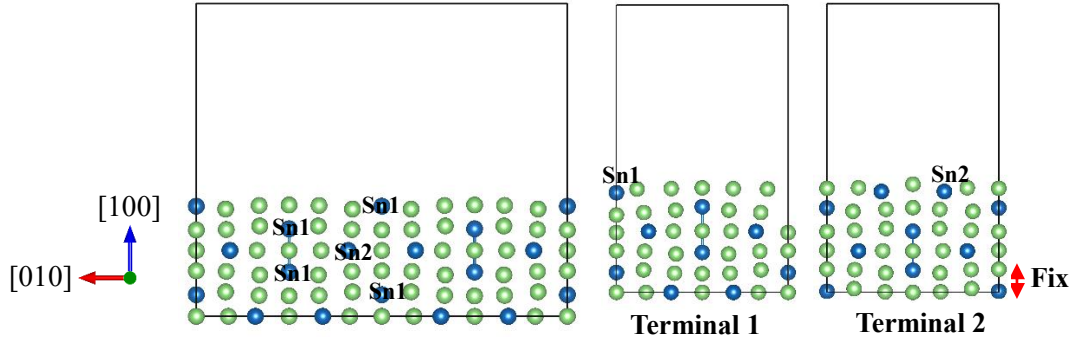
Figure 5.18 A supercell of Li$_7$Sn$_2$(100) slab with two unit cells and (100) slabs with two different terminations.

Table 5.3 Structural details of established interfaces and k-points used in simulations.

Interface	a (Å)	b (Å)	Number of atoms	k-points
Sn(100)/Cu(111)	6.793	9.257	80	5×4×1
Li$_2$Sn$_5$(110)/Cu(111)	16.033	6.793	169	2×6×1
LiSn(001)/Cu(111)	13.341	5.135	108	2×6×1
Li$_5$Sn$_2$(0001)/Cu(111)	9.257	9.257	149	4×4×1
Li$_7$Sn$_2$(001)/Cu(111)	10.270	13.341	228	3×2×1
LiSn/Cu*	13.341	5.135	152	2×6×1

* The interface LiSn/Cu refers to a symmetric interface structure.

5.3   Li$_x$Sn/Cu interface models

Through the Virtual NanoLab-Atomistic ToolKit [260], two kinds of interface models (vacuum and dense cells) are created using the obtained stable surfaces of alloys. In vacuum cells, stable Li$_x$Sn slabs are placed on Cu(111) slabs [94, 258] with 15 Å vacuum added along the c-axis of simulation cells (Table 5.3). Three possible atomic stacking configurations have been taken into consideration, that is, the interfacial Sn or Li atom locates at top, bridge and vacancy sites of interfacial Cu atoms (see Figure 5.19). The lattice mismatches for all interfaces are less than 5%. The

optimum separations (~0.24 nm) of original structures are obtained by the full relaxation of interface supercells with different separations. The LiSn/Cu dense cell is composed of an alternate stacking of a LiSn slab and a Cu slab with fully periodic boundary conditions. No vacuum is added in the model. The interfacial orientation relationships of established interfaces are shown in Figure 5.20.
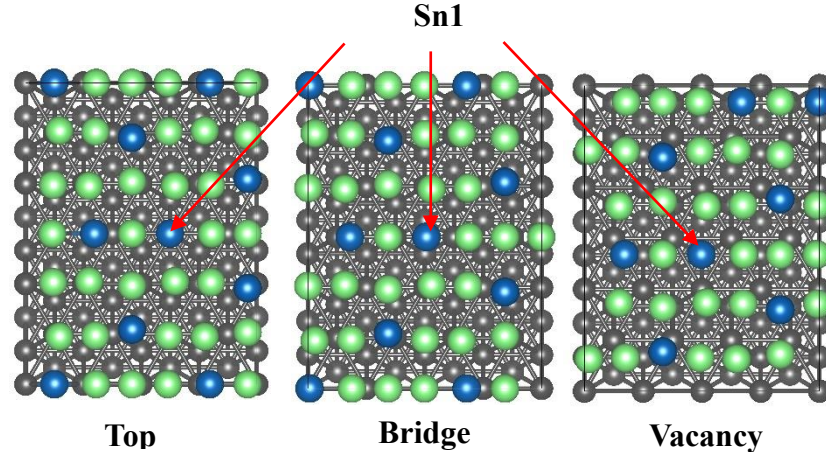
Figure 5.19 Three atomic stacking configurations of $Li_7Sn_2(001)/Cu(111)$.

5.4   Interface strength

As listed in Table 5.4, Li_xSn/Cu interfaces demonstrate almost the same work of separation (W_{sep}) values for different atomic stacking configurations when $y \leq 0.5$. Due to the anisotropy of Li_xSn alloys, W_{sep} is largely influenced by atomic stacking configurations when $y > 0.5$ [240]. Here, we also calculate the adhesion energies (W_{ad}) of Sn/Cu and LiSn/Cu interfaces. Their values with top, bridge, and vacancy atomic stackings are 1.53, 1.55 and 1.56 J m^{-2} and 1.40, 1.39 and 1.39 J m^{-2}, respectively, which are consistent with the W_{sep} values. In addition, lithiation severely weakens the interface strength between Sn active materials and Cu current collectors with W_{sep} dropping from 1.59 J m^{-2} ($y = 0$) to 0.45 J m^{-2} ($y = 0.78$) with the overall reduction of ~70% (Figure 5.21). Besides, W_{sep} decreases gradually when $y \leq 0.5$, following by a sharp drop.
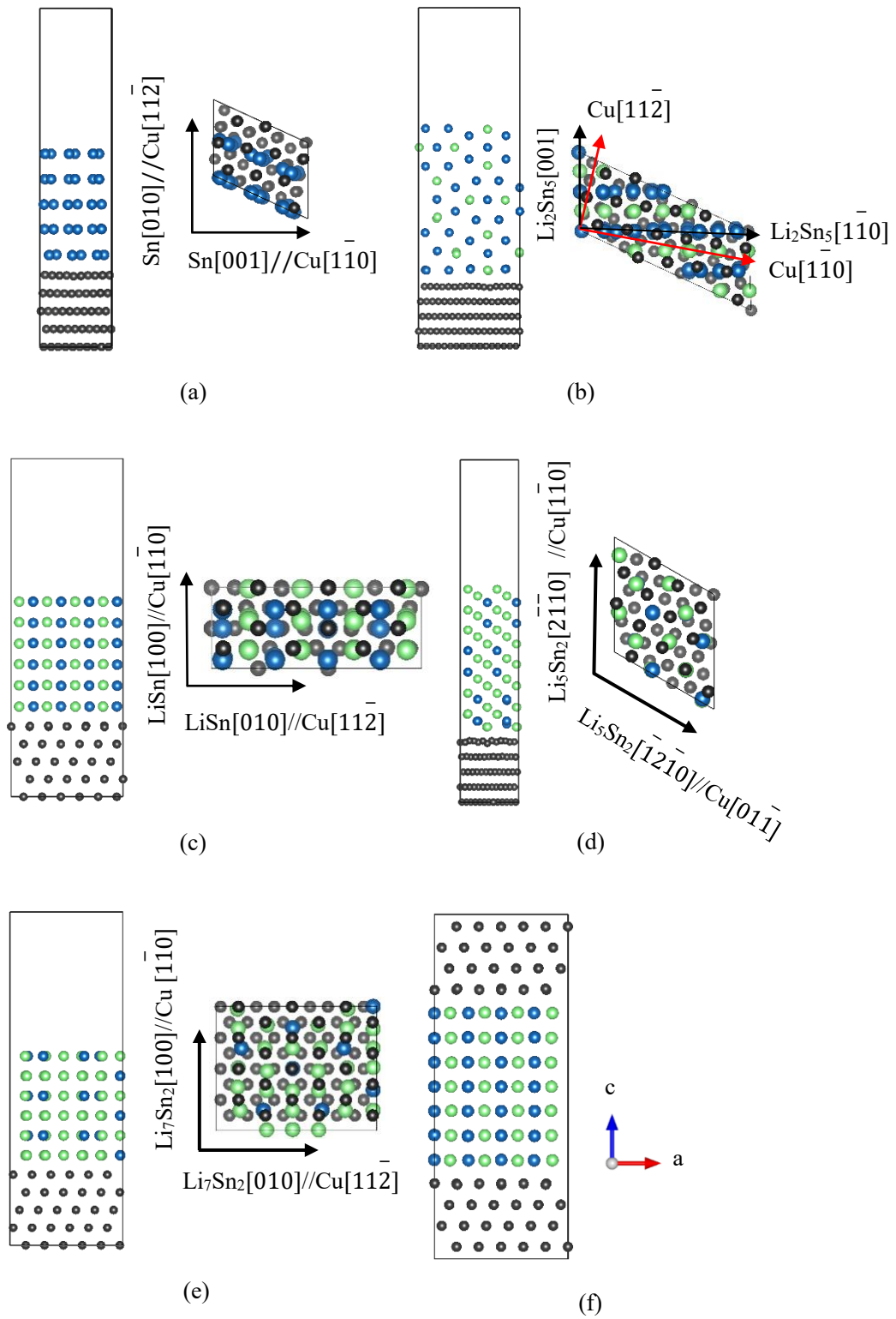
Figure 5.20 Interfacial orientation relationships of (a) Sn(100)/Cu(111), (b) Li$_2$Sn$_5$(110)/Cu(111), (c) LiSn(001)/Cu(111), (d) Li$_5$Sn$_2$(0001)/Cu(111) and (e) Li$_7$Sn$_2$(001)/Cu(111), as well as (f) LiSn(001)/Cu(111) dense cell. Cu atoms are represented by brown.

Table 5.4 W_{sep} of Li$_x$Sn/Cu interfaces with the three atomic stacking configurations.

Interface	W_{sep} (J m^{-2})		
	Top	Bridge	Vacancy
Sn(100)/Cu(111)	1.59	1.59	1.59
Li$_2$Sn$_5$(110)/Cu(111)	1.57	1.55	1.56
LiSn(001)/Cu(111)	1.47	1.48	1.47
Li$_5$Sn$_2$(0001)/Cu(111)	1.07	1.07	1.80
Li$_7$Sn$_2$(001)/Cu(111)	1.66	0.45	0.70
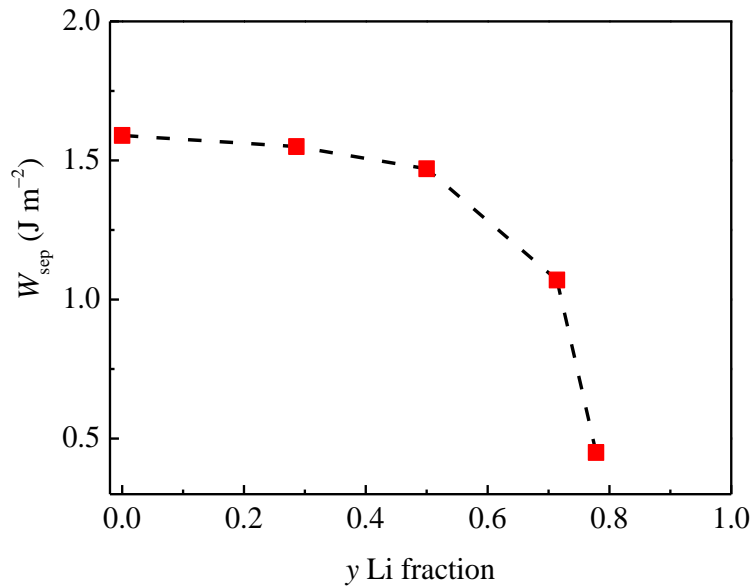
Figure 5.21 Lowest W_{sep} values of Li$_x$Sn/Cu interfaces *versus* Li fraction y.

Then, the interfacial bonding during lithiation is captured by ELF. As shown in Figure 5.22, before lithiation, there are mainly metallic bonds between neighbouring Sn atoms in bulk Sn and the interface bonding is Sn–Cu metallic bonds [239]. As lithiation goes on, Sn–Sn metallic bonds transform into weak Li–Sn ionic and Li–Li metallic bonds [244], and interfacial bonding changes from Sn–Cu to weak Li–Cu

metallic bonds. When $y = 0.71$ (Li$_5$Sn$_2$/Cu interface), Li–Cu metallic bonds play dominating roles in the interface region. This is the reason why the interface strength weakens upon lithiation.
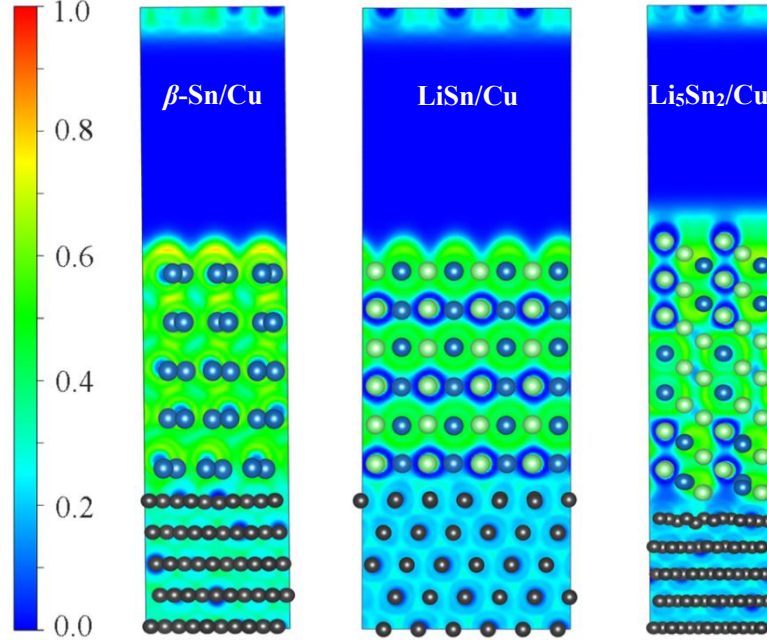
Figure 5.22 ELF of Li$_x$Sn/Cu interfaces.

Bader charge analysis is used to explore the collective effect of lithiation at interface [238]. The average net charges on interfacial Cu atoms increase with Li content y, rising from 0.06 e per atom ($y = 0$) to 0.12 e per atom ($y = 0.77$). In bulk Li$_x$Sn, Li donates all its valence electrons to Sn. However, in the presence of Cu substrate, charges are redistributed among bonds with Cu and Sn. That is, Li donates fewer electrons to Sn comparing with the number of electrons from Li in bulk Li$_x$Sn. Thus, each Sn can coordinate with more Li-ions, which results in a higher Li/Sn ratio and weaker Li–Sn bonds near the interface. This would cause the fracture of Li$_x$Sn/Cu interface near the interface region. With lithiation, more negative charges localize on interfacial Cu atoms which leads to segregation of Li-ions at interface and transformation of interfacial bonding from Sn–Cu to weak Li–Cu bonds. Therefore, the interface strength weakens upon lithiation. Similar phenomena were observed at Li$_x$Si/Cu and Li$_x$Si/graphene interfaces [94, 261].

5.5   Fracture of LiSn/Cu interfaces

Then, we simulated the fracture of LiSn/Cu interface under tension by using the symmetric interface. As shown in Figure 5.23, when strain is less than 0.04, stress increases almost linearly with the increase of strain and then stress fluctuates with rising strain, indicating the appearance of cracks in the interface. The normal stress of LiSn/Cu interface reaches its maximum value of 6.42 GPa at a strain of 0.12, then tension results in fracture of the dense cell within the lithiated Sn slab. Then stress descends largely after its maximum value and interface structure demonstrates brittle fracture, which is due to the brittle property of LiSn. The structure is completely fragmented at $\varepsilon = 0.16$ where the distance between two free surfaces is more than 5 Å.
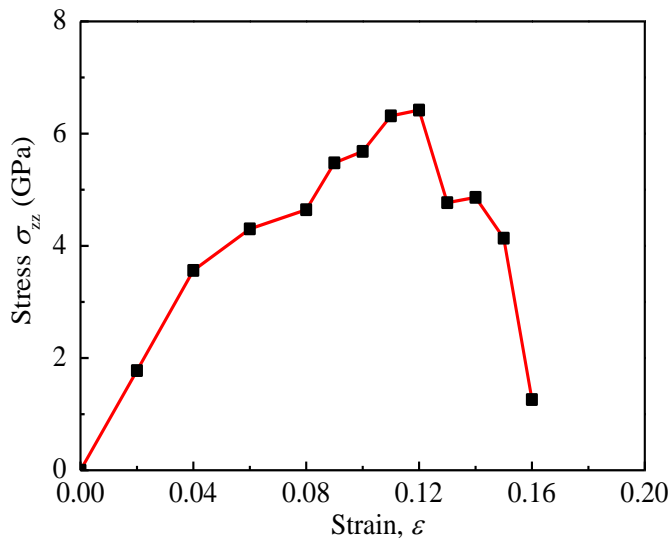
Figure 5.23 The stress-strain curve of LiSn/Cu dense cell.

The failure process is also reflected from the change of interlayer spacing (d_{ij}) with strain. As seen in Figures 5.23, 5.24 and 5.25, when strain is less than 0.02, tension mainly leads to the increase of d_{23}, while d_{12}, d_{34} and d_{45} display minor change. Specially, d_{23} increases continuously with the increase of strain, indicating that the chemical bond strength of LiSn slab near the interface region is the weakest. At $\varepsilon =$

0.02, Sn–Sn bonds between the first and second LiSn layers near the interface region are broken. At $\varepsilon = 0.02$–0.08, d_{12}, d_{23}, d_{34} and d_{45} all increase with the increase of strain and tension makes Sn–Sn bonds between the second and third LiSn layers, the third and fourth LiSn layers, and the fifth and sixth LiSn layers near the interface region gradually fracture (Figure 5.24). At $\varepsilon = 0.08$, most Sn–Sn bonds in LiSn layer break, resulting in a slow increase in stress with strain. The interface structure changes when the strain is 0.09. The d_{12} and d_{34} decrease largely at $\varepsilon = 0.09$, while d_{23} shows a great increase. Further stretching, d_{23}, d_{34} and d_{45} increase gradually with the increase of strain, while d_{12} decreases gradually (Figure 5.25). The fracture and recombination of chemical bonds happen in this process. Stress reaches its maximum value when the strain is 0.12, After that, crystal structure of LiSn layer disintegrates and interface structure begins to distort and deform, and d_{23} increases largely with rising strain. Finally, interface structure is completely fragmented when the strain is 0.16 and the fracture position is in the LiSn layer near the interface region, which is due to the weakening effect of the interfacial segregation of Li-ions on Li–Sn bonds near the interface region.
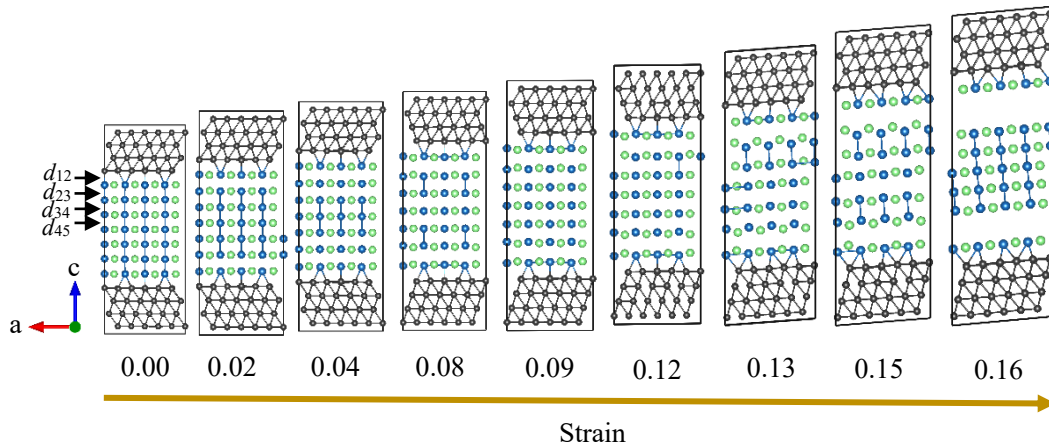
Figure 5.24 Relaxed LiSn/Cu dense cell at different strain.

As seen in Figure 5.24, one-layer LiSn adhered to Cu substrate means the occurrence of adhesive transformation in the fractured interface [225]. The cohesion energy of bulk LiSn ($0.80 \ \mathrm{J \ m^{-2}}$) is approximately twice the γ_s of LiSn(001). W_{sep} of

LiSn/Cu interface (1.47 J m^{-2}) is much larger than the cohesion energy. From the ratio (1.84) of W_{sep} to cohesion energy, adhesive transformation is more likely to happen for LiSn/Cu interface. In addition, the work of decohesion (W_{dec}) (0.69 J m^{-2}) (Figure 5.26) is smaller than W_{sep} and thus fracture within LiSn slab is easier than at interface. Similar cases are found at Sn/Cu, Li$_2$Sn$_5$/Cu and Li$_5$Sn$_2$/Cu interfaces because of the ratios of W_{sep} to cohesion energy of 1.99, 2.21 and 1.27 J m^{-2}, respectively. The fracture of Li$_7$Sn$_2$/Cu interface would appear at interface since its W_{sep} (0.45 J m^{-2}) is smaller than bulk cohesive energy (1.26 J m^{-2}).
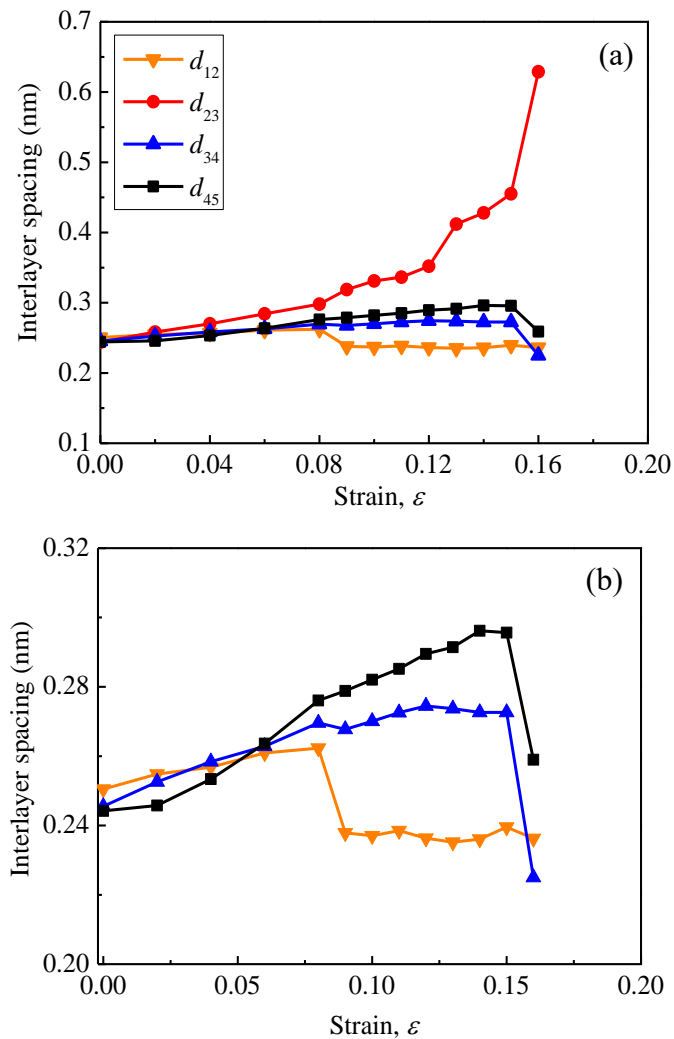
Figure 5.25 The variation of (a) interlayer spacings and (b) amplified d_{12}, d_{34} and d_{45} with the increase of strain.
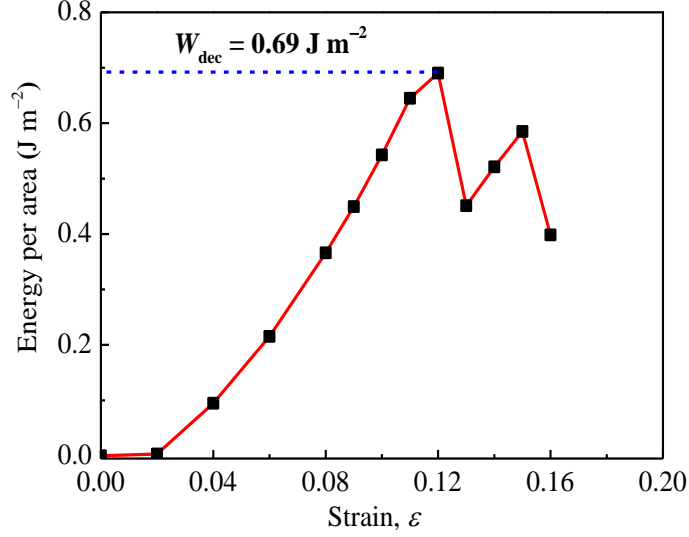
Figure 5.26 Energy per area (J m^{-2}) of LiSn/Cu interface *versus* strain.

5.6 Failure of Sn−Cu core-shell spherical particles

In a hollow core-shell spherical structure, the core and shell respectively undergo compressive and hoop tensile stresses during lithiation. The latter would lead to the fracture of the shell. Upon delithiation, radial tensile stress in both the core and shell may result in debonding between the inner core and outer shell, which seriously influences the electrochemical performance of electrodes [191]. Based on simulation results and theoretical studies[157], fracture and debonding of a hollow Sn−Cu core-shell spherical particle are investigated (see Figure 5.27). To completely fill the hollow space, the structure should satisfy with the following geometric condition, namely

$$\frac{B}{A} = \left(\frac{\beta - 1}{\beta}\right)^{1/3} \, , \tag{5.1}$$

where $\beta = V_f/V_i$ is the volumetric swelling ratio with V_f the fully lithiated volume and V_i the initial volume of a Li-free state. The β of Sn in lithiation is 2.59 [124], that is, $B/A = 0.85$. At a given state, SOC can be expressed by

$$SOC = \frac{B^3 - C^3}{B^3} \, . \tag{5.2}$$

Combining Eqs. (5.1) and (5.2), the inner radius C can be written as

$$C = 0.85A(1 - SOC)^{1/3} \, . \tag{5.3}$$

According to the linear elastic fracture theory, the energy release rate of coating fracture due to the hoop tensile stress in a shell is

$$G_f = 2\frac{\sigma_Y^2}{Y_s}\left(\log\frac{A}{C}\right)^2\frac{A^2}{L} \,, \tag{5.4}$$

where Y_s is Young's modulus of Cu shell, σ_Y is the yield strength of lithiated Sn, and L is shell thickness. Parameters A and C are core and partially lithiated inner radii, respectively, (Figure 5.27(a)). Similarly, due to the radial tensile stress during delithiation, the energy release rate of interface debonding between the Sn core and stiff Cu shell is

$$G_d = 4\pi\frac{\sigma_Y^2}{Y_e}\left(\log\frac{A}{C}\right)^2 \,, \tag{5.5}$$

where Y_e is the effective modulus, indicating the influence of inhomogeneous properties of core and shell, which can be expressed as

$$\frac{1}{Y_e} = \frac{1}{2}\left(\frac{1}{Y_c} + \frac{1}{Y_s}\right) \,, \tag{5.6}$$

where Y_c and Y_s are Young's moduli of core and shell, respectively. The critical condition for shell fracture is that the energy release rate G_f is equal to the γ_s of Cu shell. The critical condition for debonding is $G_d = W_{sep}$. To determine the optimal dimension range of core and shell as a function of SOC, Figure 5.27(b) describes the effect of core size and SOC on interface fracture and debonding for a typical shell thickness L, ranging from 3 to 20 nm. The *ab initio* simulation results were applied, including the fracture energy of Li_7Sn_2/Cu interface (0.45 J m^{-2}) and the γ_s of Cu (1.40 J m^{-2}) [257]. The σ_Y and Y of lithiated Sn are 1.2 GPa [134] and 48.9 GPa [240], respectively, and Y of Cu is 116.5 GPa [262]. It is shown that a thinner shell is easier to fracture, while less likely to debonding. The critical SOC value of debonding increases with the decrease of shell thickness [157]. The core-shell structure with a thin shell could maintain safe cycling for core sizes in a certain range at high SOC. The size-dependent failure of electrode materials has been observed in many studies [148, 157, 188]. Such a finding can be used to explain the observed experimental phenomenon, where Sn−Cu core-shell nanoparticles consisting of 8.65 nm Sn core and

1.35 nm Cu shell demonstrated an excellent charge capacity (620 mAh g^{-1}) and capacity retention (86%) at the current density of 3600 mAh g^{-1} [259]. Based on Figure 5.27(b), these core and shell sizes could avert fracture and debonding during lithiation and delithiation at a high SOC (0.94), which almost reaches a full lithiation state.
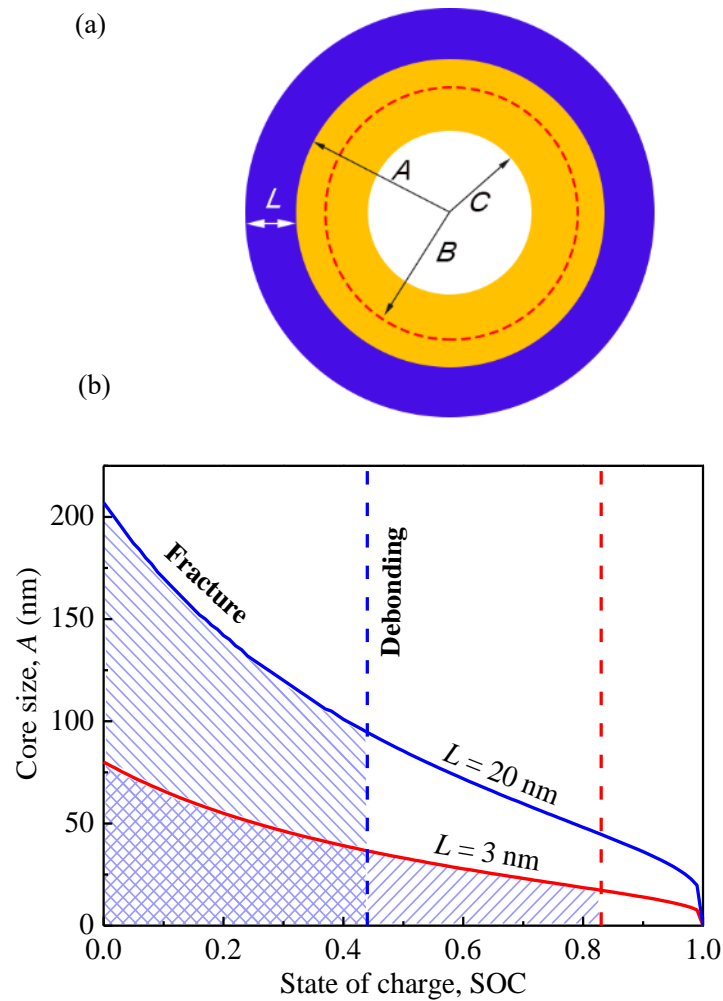
Figure 5.27 (a) The Sn–Cu hollow core-shell structure. The core radius is A, and the inner radii before lithiation and partially lithiated are B and C, respectively. The particle is coated by a stiff Cu shell with a thickness of L; (b) Conditions of fracture and debonding for a hollow core-shell spherical particle. The critical core size for fracture and the SOC value for debonding at a shell thickness of 3 and 20 nm are shown by solid and dash line, respectively.

5.7   Conclusions

First-principles calculations have been performed to study the evolution of interface strength between a Sn electrode and a Cu current collector during the lithiation process. The results show that lithiation severely weakens the interface strength between active materials and current collectors. The W_{sep} decreases from 1.59 J m^{-2} (before lithiation) to 0.45 J m^{-2} (with Li content of 0.78), with a total reduction of about 70%. When Li content is less than 0.5, W_{sep} decreases slowly, and then decreases sharply, which is mainly due to the large anisotropy and ductile-brittle transformation of Li$_x$Sn alloys. Chemical bonding analysis shows that the decrease of interfacial bonding strength is attributed to the transformation of interfacial chemical bond from strong Sn–Cu bonds to weak Li–Cu bonds during lithiation. The study of stress-strain behaviour of LiSn/Cu interface shows that the maximum tensile stress of LiSn/Cu interface is 6.42 GPa at the strain of 0.12. After that, the interface begins to fracture, and the whole interface structure breaks completely at a strain of 0.16. The fracture occurs inside LiSn alloy rather than at interface. This is mainly due to the weakening of chemical bonding near the interface region which is caused by the segregation of Li-ions at interface. Moreover, the interfacial segregation of Li-ions makes the fracture of most Li$_x$Sn/Cu interfaces occur within Li$_x$Sn slabs. Due to the strong anisotropy, it is more likely for Li$_7$Sn$_2$/Cu interface to fracture at interface. Based on the simulation results, an optimal design condition can be determined for a Sn–Cu hollow core-shell spherical structure. This study deepens our understanding of the failure mechanism of the electrode-collector interface during lithiation. The results can be used to determine the interatomic function in molecular dynamics simulations, and further to simulate the deformation and stress fields of electrodes during lithiation and delithiation processes.

Chapter 6

Effects of Cu$_x$Sn alloys on interface properties of electrode-collector

Abstract

The effects of Cu$_x$Sn alloys on the interfacial mechanical properties of electrode-collector have been explored. The results show that the formation of Cu$_x$Sn at the electrode-collector interface enhances the interface strength. The W_{sep} values of Cu$_3$Sn/Cu and Cu$_6$Sn$_5$/Cu interfaces are 1.74 and 1.73 J m^{-2} which are about 9% higher than that of Sn/Cu interface. Besides, Cu$_x$Sn alloys can strengthen the deformation resistance of electrode-collector interface at large strains. Li$_2$CuSn/Cu interface could sustain large stress of 5.81 GPa before fracture starts at the strain of 0.20. The interface is totally fragmented at a strain of 0.28, which is much larger than that (0.16) of LiSn/Cu interface. This work provides a more actual description of the interface properties of electrode-collector. In addition, it explains the micromechanism for the excellent electrochemical performance of Cu$_x$Sn containing composite electrodes.

6.1 Introduction

A small amount of Cu_xSn alloys (Cu_6Sn_5 and Cu_3Sn) would form between active materials and Cu current collector in the preparation process, even for pure Sn active materials without heat treatment [263, 264]. And the formation of Cu_xSn intermetallic compound layers was found to have a large influence on the mechanical behaviours of electrode materials. Kali *et al.*[145] found that the existence of intermetallic phases could largely relieve the mechanical degradation of electrode materials during the repeated lithiation and delithiation processes. The Cu_xSn alloys can also enhance the integrity of electrode materials. The annealed Sn/intermetallic film could remain fairly intact electrode structures with some cracks after 35 charge-discharge cycles while the as-deposited Sn film was completely disintegrated and delaminated from current collector (Figure 6.1). It is believed that Cu_xSn could increase the interface strength between active materials and Cu current collector which leads to the enhanced cyclability and capacity retention [145, 263, 264]. However, accurate values are unavailable and there is limited understanding of the micromechanism.
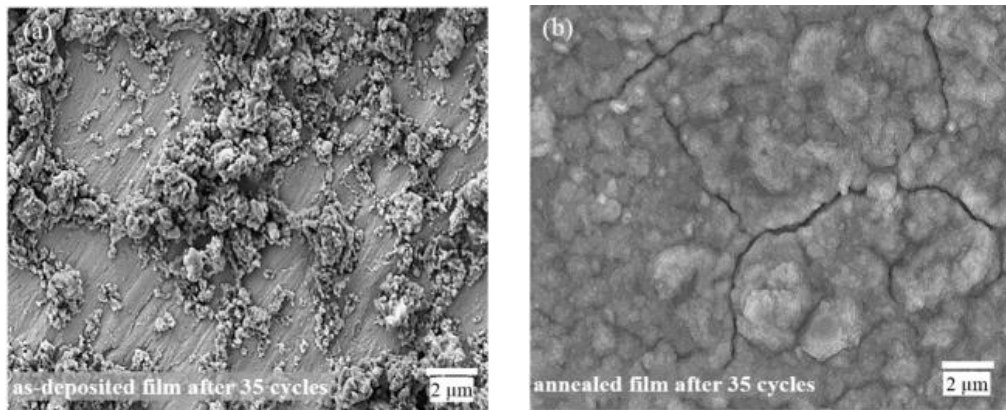
Figure 6.1 Scanning electron microscopy images of (a) as-deposited Sn and (b) annealed Sn/intermetallic film electrodes after 35 cycles with constant current [145].

In this chapter, by using *ab initio* calculation, we have systematically investigated the influence of Cu_xSn alloys on the interfacial mechanical properties of electrode-

collector, including the interface strength, interfacial fracture location as well as fracture energy. Bonding analysis has also been conducted to explain the obtained interfacial properties. This work provides a clear description of the role of Cu_xSn alloys on the interfacial properties of electrode-collector. Besides, Cu_xSn intermetallic compounds and in particular Cu_6Sn_5 have received much attention as alternative electrode materials due to inexpensiveness, environmentally friendly and good structural integrity during the electrochemical cycles [156, 265-267]. Various electrode materials containing Cu_6Sn_5 show excellent electrochemical performance. Studying the interfacial mechanical properties of Cu_xSn/Cu interface will be vital to the further utilization of Cu_xSn alloys as promising electrode materials.
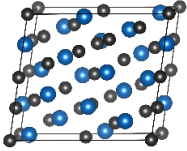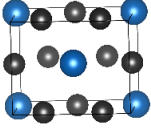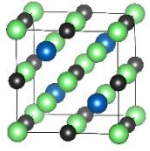
6.2   Surface properties of Cu_xSn alloys

Since the lithiation of Cu_3Sn directly forms Li_xSn, while Cu_6Sn_5 becomes Li_2CuSn before Li_xSn appears [268, 269]. Cu_6Sn_5 and Cu_3Sn alloys are employed to study the influence of Cu_xSn on the interfacial mechanical properties of electrode-collector. Li_2CuSn is used to evaluate the lithiation effect on interfacial properties. The calculation method used in this chapter is the same as Chapter 5. As given in Table 6.1, the obtained lattice constant of Li_2CuSn is 6.323 Å, which agrees well with the experimental value with the gap of ~0.6%. Also, the simulated lattice parameters of Cu_6Sn_5 and Cu_3Sn match well with experimental results.

Based on the optimized bulk structures, surface energy convergence tests are performed to find the stable surfaces to form interfaces with Cu current collector, and the obtained results are given in Table 6.2. For Cu_6Sn_5 and Cu_3Sn, experiments show that their (204) and (001) surfaces are respectively the most stable surface to form interfaces with Cu(111) [270, 271]. $Cu_6Sn_5(204)$ only has one atom termination and there is a little difference (about 0.01 J m^{-2}) of surface energies (γ_s) between models with eight and ten formula units (Figure 6.2). As shown in Figure 6.3, $Cu_3Sn(001)$ has two different terminations with γ_s of 0.81 and 0.76 J m^{-2}, respectively. The (001)

surface with terminal 2 is the most stable. Surface energy convergence test of slabs with terminal 2 shows that models with four and six formula units show almost the same γ_s with a little gap of 0.01 J m^{-2}.

Table 6.1 Crystal structures and obtained lattice constants (Å) of Cu_6Sn_5, Cu_3Sn, and Li_2CuSn. The experimental values are given in the parentheses [272-274].

	η'-Cu_6Sn_5	Cu_3Sn	Li_2CuSn
a	11.103 (11.022)	5.542 (5.529)	6.322 (6.282)
b	7.391 (7.282)	4.344 (4.323)	6.322 (6.282)
c	10.003 (9.827)	4.852 (4.775)	6.322 (6.282)
β	98.765	–	–
k-points	3×5×3	9×11×11	5×5×5
Crystal structures			
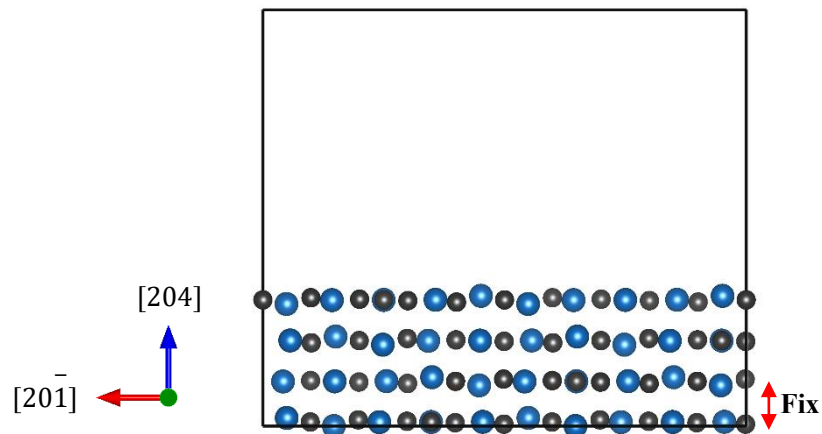
Figure 6.2 Cu_6Sn_5(204) slab with eight formula units.

Table 6.2 Calculated surface energy (γ_s) of main low-index planes of Cu_6Sn_5, Cu_3Sn and Li_2CuSn. Slab thicknesses are given in the parentheses which are indicated by the number of formula units of Cu_xSn alloys in a slab model.

Phases	Plane	γ_s (J m^{-2})	
Cu_6Sn_5	(204)	0.71 (8 Cu_6Sn_5)	0.72 (10 Cu_6Sn_5)
Cu_3Sn	(001)	0.76 (4 Cu_3Sn)	0.77 (6 Cu_3Sn)
Li_2CuSn	(100)	0.86 (3 Li_2CuSn)	0.83 (4 Li_2CuSn)
	(111)	0.52 (3 Li_2CuSn)	0.44 (4 Li_2CuSn)
	(011)	0.78 (3 Li_2CuSn)	0.76 (5Li_2CuSn)
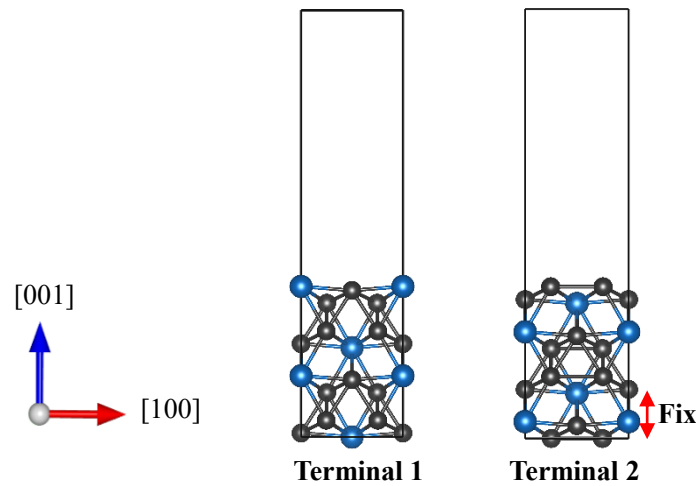
Figure 6.3 Cu_3Sn(001) slabs with two different atom terminations.

For Li_2CuSn, surface energy test is conducted for its (100), (011) and (111) surfaces. As illustrated in Figure 6.4, (111) surface has four kinds of atom terminations. The surface energies of slabs with Li1, Li2, Cu and Sn atom terminations are 0.77, 0.52, 1.36 and 0.98 J m^{-2}, and Li2-terminated slab has the lowest surface energy. The test of slab thickness demonstrates that three formula units are required to form a stable surface (Figure 6.5). According to the periodic atomic stacking along [100] direction, (100) surface has two atom terminations (Figure 6.6) and these two terminations have

almost the same surface energy (about 0.86 J m^{-2}). Similarly, there is one atom termination for (011) surface with a surface energy of 0.78 J m^{-2}, as illustrated in Figure 6.7. Thus, (111) has the lowest surface energy. Since (111) has the lowest lattice mismatch with Cu(111) (0.35%), (111) is the stable surface to form interface.
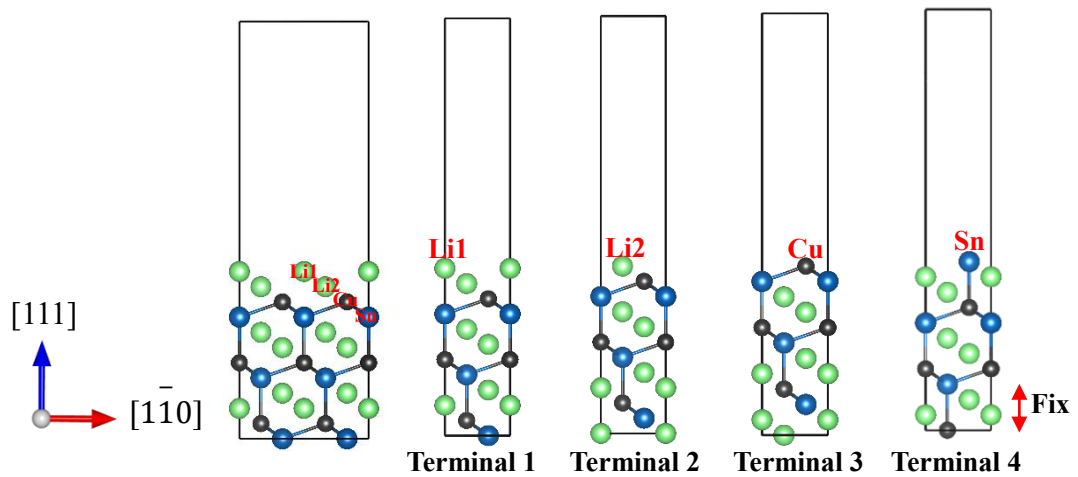
Figure 6.4 Atomic layer stacking of a (2×1) Li$_2$CuSn(111) slab supercell and (111) slabs with four different atom terminations.
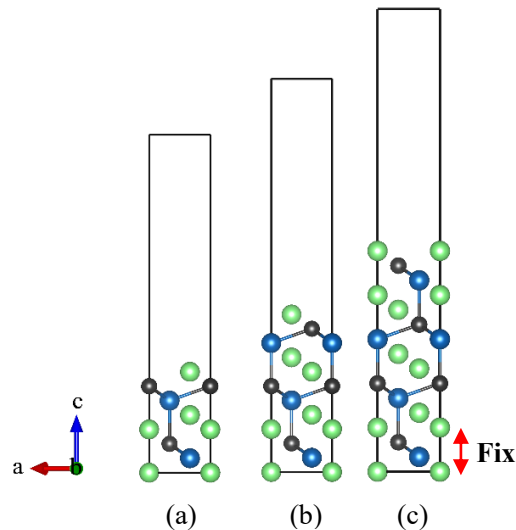
Figure 6.5 Li$_2$CuSn(111) slabs (with Li2 atom termination) with slab thicknesses of (a) two, (b) three and (c) four formula units.
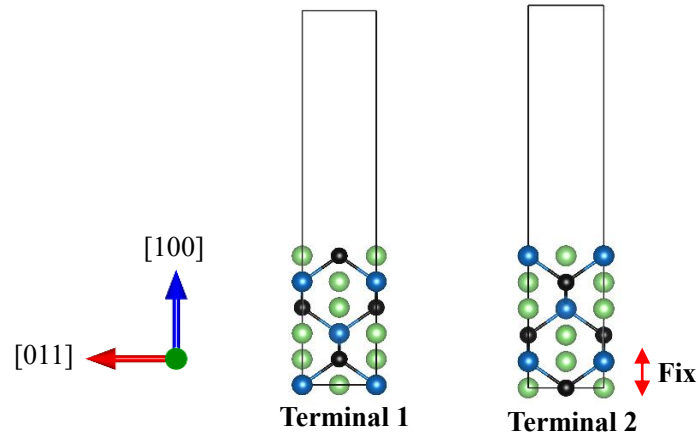
Figure 6.6 Li$_2$CuSn(100) slabs with two different atom terminations.
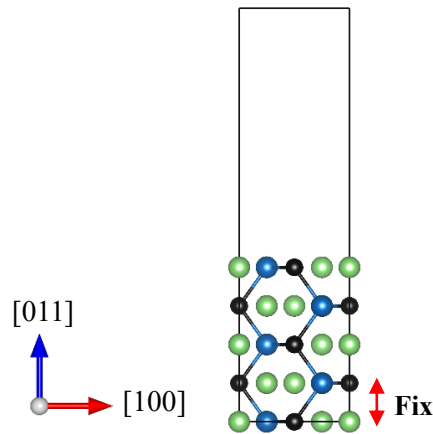
Figure 6.7 Li$_2$CuSn(011) slab with one atom termination.

6.3 Cu$_x$Sn/Cu interface models

Like Li$_x$Sn/Cu interface, based on the obtained stable surfaces, two kinds of interface models are constructed, as shown in Figure 6.8. The lattice mismatches between Cu$_x$Sn or Li$_2$CuSn stable surfaces and Cu(111) are less than 5%. The interfacial orientation relationships of the established interfaces are shown in Figure 6.9, and three possible atomic stacking configurations are taken into consideration (see Figure 6.10). The optimum separations (about 2.40 Å) of original structures are obtained by full relaxation of interface supercells with different separations.
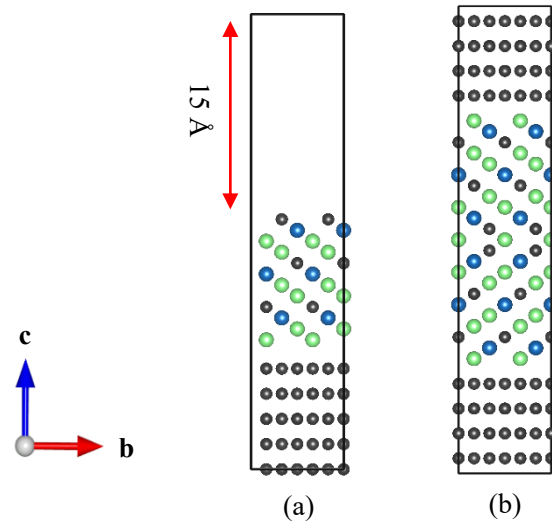
Figure 6.8 (a) Vacuum and (b) dense cells of $Li_2CuSn(111)/Cu(111)$ interface.
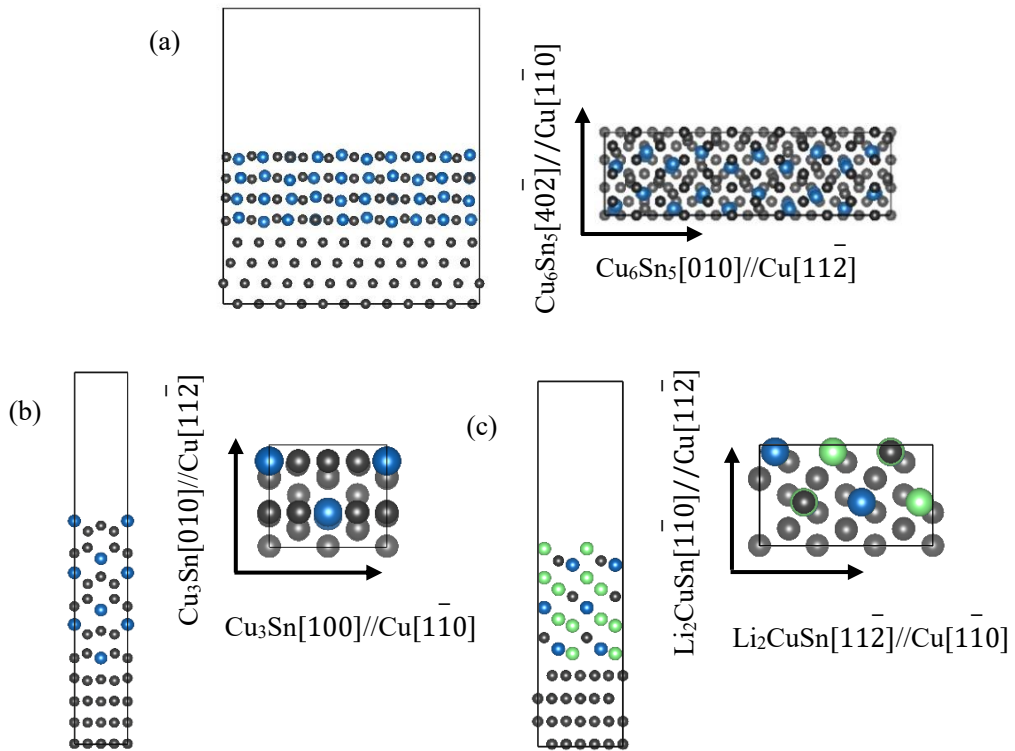
Figure 6.9 Interfacial orientation relationships of (a) $Cu_6Sn_5(204)/Cu(111)$, (b) $Cu_3Sn(001)/Cu(111)$ and (c) $Li_2CuSn(111)/Cu(111)$ interfaces.

Li1
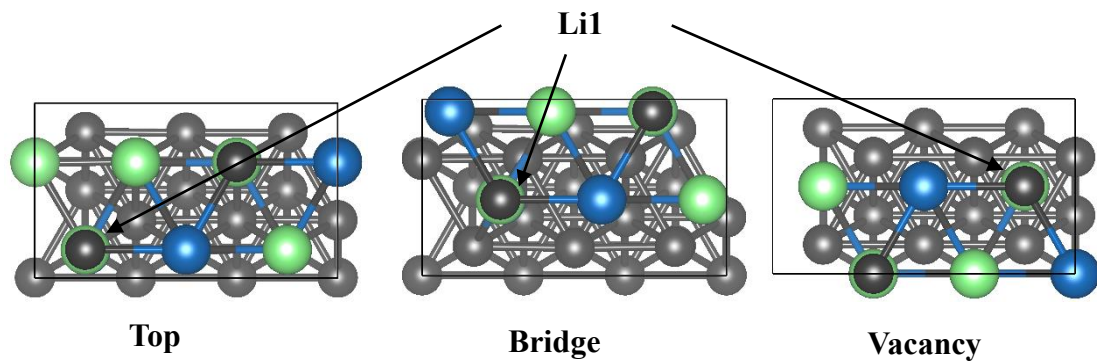
Top   **Bridge**   **Vacancy**

Figure 6.10 Three atomic stacking configurations of $Li_2CuSn(111)/Cu(111)$ interface with interfacial Li atom (Li1) placed on top, bridge and vacancy sites of interfacial Cu atoms.

6.4   Interface strength

The work of separation (W_{sep}) is used to evaluate the interface strength between Cu_xSn alloys and Cu current collectors and its variation upon lithiation. Here, the vacuum interface model is applied here. As seen in Table 6.3, the calculated W_{sep} values of $Cu_3Sn(001)/Cu(111)$ interfaces with top, bridge, and vacancy stacking configurations are 1.79, 1.85, 1.74 J m^{-2}, which agree well with the 1.87 J m^{-2} of $Cu_3Sn(100)/Cu(100)$ interface [275]. Since $Cu_3Sn(001)/Cu(111)$ is the most stable interface between Cu_3Sn and Cu, it has lower W_{sep} value than that of $Cu_3Sn(100)/Cu(100)$ interface. Besides, $Cu_3Sn(001)/Cu(111)$ interface shows a little higher W_{sep} than those of $Cu_6Sn_5(204)/Cu(111)$ interface. This is due to the more Cu–Cu metallic bonds at $Cu_3Sn(001)/Cu(111)$ interface. $Li_2CuSn(111)/Cu(111)$ interface demonstrates lower W_{sep} values than that of $Cu_6Sn_5(204)/Cu(111)$ which suggests that lithiation weakens the interface strength. Comparing the W_{sep} of Cu_xSn/Cu interfaces with that (1.59 J m^{-2}) of Sn/Cu interface [276], it is seen that the formation of Cu_xSn alloys at interface increases the interface strength by about 9%. And like the case of Sn/Cu interface, lithiation deteriorates the interface strength of Cu_xSn/Cu interface.

103

Table 6.3 W_{sep} (J m^{-2}) of relaxed Cu$_x$Sn/Cu interfaces with the three atomic stacking configurations.

W_{sep}	Cu$_6$Sn$_5$(204)/Cu(111)	Li$_2$CuSn(111)/Cu(111)	Cu$_3$Sn(001)/Cu(111)
Top	1.73	1.57	1.79
Bridge	1.75	1.54	1.85
Vacuum	1.74	1.57	1.74

To have an in-depth understanding of interface properties, electron localized function (ELF) is employed to capture the interfacial bonding characteristics. As seen in Figure 6.11, metallic bonds, as displayed by green, are located between neighbouring Sn and Cu atoms in bulk Cu$_x$Sn alloys. As lithiation, Sn–Cu metallic bonds transform into weak Li–Sn, Li–Cu and Li–Li metallic bonds. Similar changes occur in the interfacial zone, with interface bonding changing from Sn–Cu and Cu–Cu metallic bonds (for Cu$_6$Sn$_5$/Cu and Cu$_3$Sn/Cu interface) to Sn–Cu and Li–Cu metallic bonds (for Li$_2$CuSn/Cu interface). This leads to weakened interface strength. There are more Cu–Cu and less Cu–Sn metallic bonds at Cu$_3$Sn(001)/Cu(111) interface comparing to those of Cu$_6$Sn$_5$(204)/Cu(111) interface, which makes Cu$_3$Sn(001)/Cu(111) interface show a little stronger interface strength.

Based on Bader charge analysis, the collective effect of lithiation at interface is further investigated by the variations of the average valence charges on Cu substrate. For Cu$_6$Sn$_5$(204)/Cu(111) and Li$_2$CuSn(111)/Cu(111) interface, the average net charge on Cu atom at the interface region is 0.04 and 0.11, respectively. The average net charge increases largely upon lithiation, indicating that the segregation of Li-ions occurs at Li$_2$CuSn(111)/Cu(111) interface. In bulk Li$_2$CuSn, the valence electrons of Li are distributed among bonds with Cu and Sn. The excess negative charges on Cu atoms at interface implies that Li donates fewer electrons to Sn atoms located near the interface region comparing with the obtained valence electrons from Li in bulk Li$_2$CuSn. Thus, each Sn can coordinate with more Li-ions, which results in a higher

Li/Sn ratio and weaker Li–Sn bonds near the interface. This would induce the fracture of Li$_2$CuSn/Cu interface near the interface region. Besides, Li segregation at interface would lead to the gradual transformation of interfacial bonding from Sn–Cu to weak Li–Cu bonds. This induces the decreased interfacial strength upon lithiation.
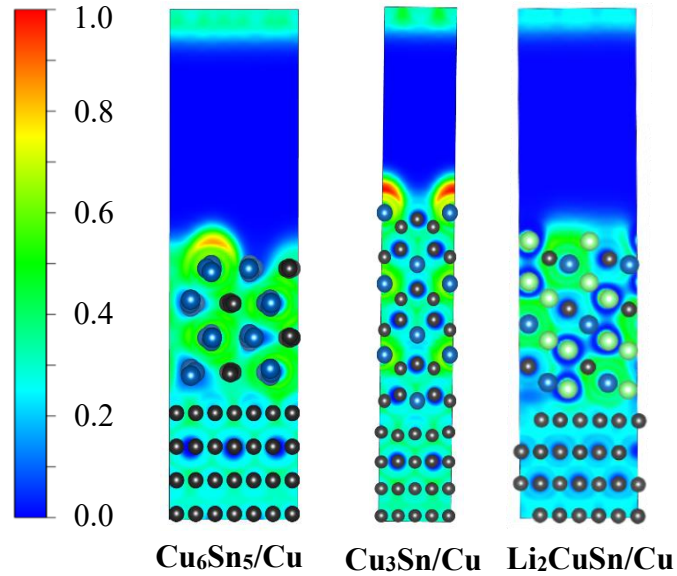
Figure 6.11 ELF of Cu$_6$Sn$_5$(204)/Cu(111), Cu$_3$Sn(001)/Cu(111) and Li$_2$CuSn(111)/Cu(111) interface.

6.5 Fracture of Li$_2$CuSn/Cu interfaces

Fracture of Li$_2$CuSn/Cu interfaces is investigated by using the same method for LiSn/Cu dense cell in chapter 5. As seen in Figure 6.12, when the strain is less than 0.04, the stress increases with strain, and then the stress fluctuates with the increase of strain, which indicates that cracks appear in the interface structure and various metastable structures involving bond rupture and reforming are generated in this process. When the strain is 0.20, the normal stress reaches the maximum (5.81 GPa). Then, the stress decreases gradually. The interface is completely fragmented at the strain of 0.28, which is much larger than that (0.16) of LiSn/Cu interface (as seen in Figure 6.12 and 6.13).
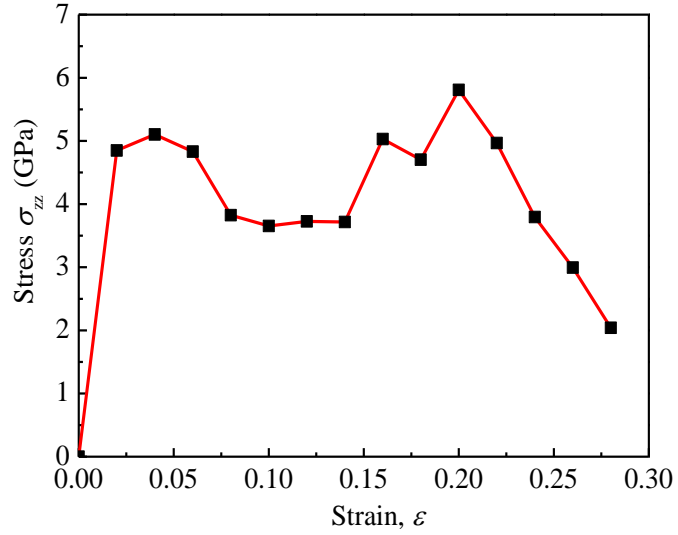
Figure 6.12 The stress-strain curve of Li$_2$CuSn/Cu dense cell.
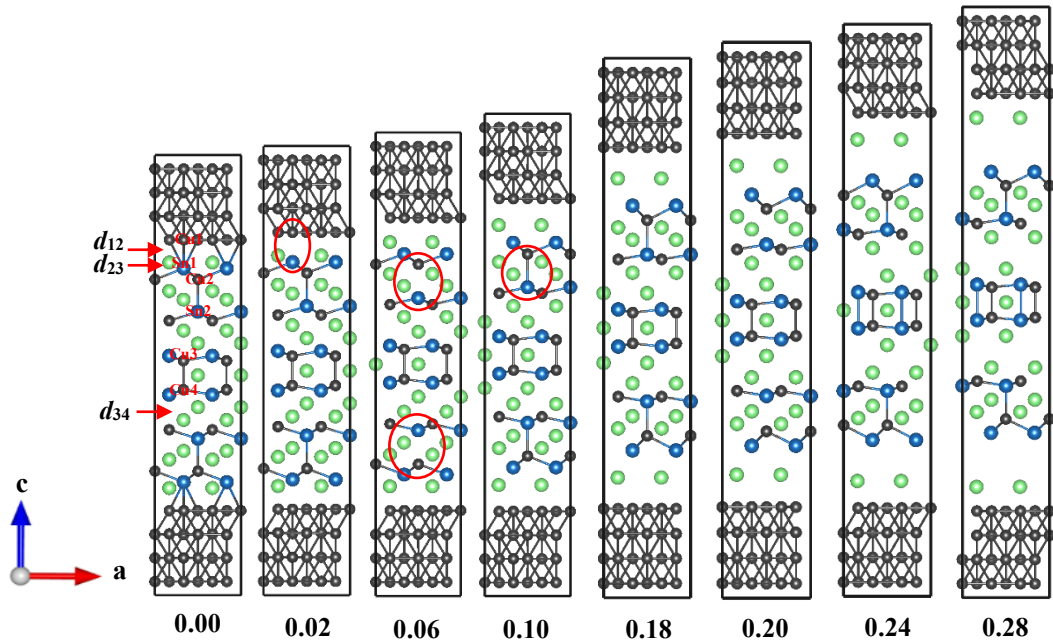
Figure 6.13 Relaxed Li$_2$CuSn/Cu dense cells at various stages of strain.

The fracture of the interface can also be reflected from the variation of main interlayer spacings (d_{12}, d_{23}, d_{34}) and bond lengths with strain. As shown in Figure 6.13 6.14 and 6.15, when the strain is less than 0.02, tension mainly leads to the weakening

of the Cu1–Sn1 bond at the interface and the Cu1–Sn1 bond breaks at the strain of 0.02. Further stretching, the Cu2–Sn2 and Cu3–Cu4 bonds contribute to the increase of the stress. At the strain of 0.06, the fracture of Cu2–Sn2 bond decreases the tension resistance of the system, thus, stress begins to decrease with strain. At the same time, the slope of d_{12} and d_{34} increases. During the strain of 0.02 ~ 0.14, the d_{23} increase rapidly with the rise of strain which indicates that the Li–Sn bond near the interface region is the weakest.
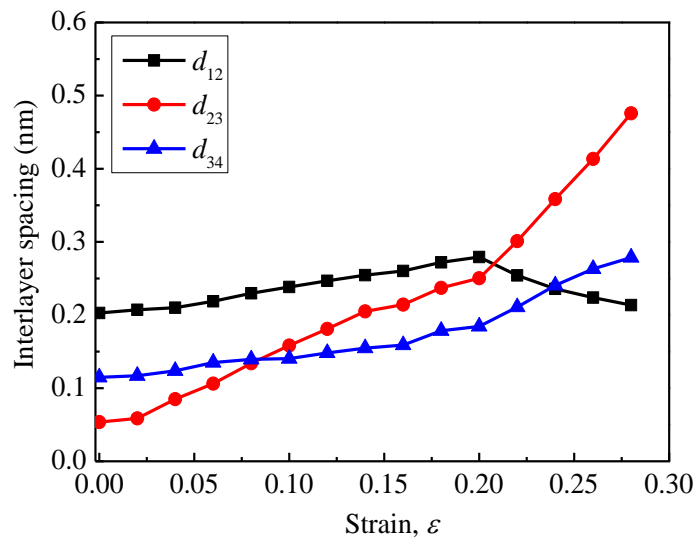
Figure 6.14 The variation of interlayer spacings with the increase of strain.
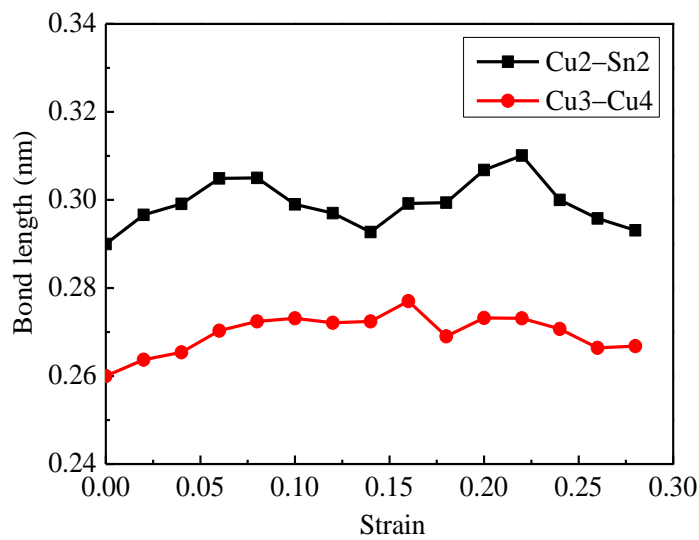
Figure 6.15 The change of bond lengths with increasing strain.

At $\varepsilon = 0.10$, the reformation of Cu2–Sn2 bond strengthens the interface structure which stops the decrease of stress with strain. When $\varepsilon = 0.10 \sim 0.14$, the bond lengths of Cu2–Sn2 and Cu3–Cu4 decrease gradually with strain, while the lengths of d_{ij} increase largely, revealing that Li–Cu and Li–Sn bonds near the interface and Li–Li metallic bonds in Li$_2$CuSn slab play the major roles in this process. The interfacial structure tends to be stable during this strain range which leads to stable stress. When the strain reaches 0.16–0.18, the interfacial structure becomes unstable. The fluctuation of the Cu2–Sn2 and Cu3–Cu4 bond lengths makes the stress vary greatly. When the strain is 0.16, the bond length of Cu2–Sn2 and Cu3–Cu4 bonds increases, unveiling that the increase of stress is mainly contributed by these two chemical bonds. Then, the stress decreases at $\varepsilon = 0.18$. At this strain, the bond lengths of Cu2–Sn2 and Cu3–Cu4 bonds change little, but the slopes of d_{12}, d_{23} and d_{34} increase. Therefore, the Li–Cu and Li–Sn bonds near the interface and the Li–Li metallic bonds in Li$_2$CuSn slab play the leading roles at this strain and their weak bond strength is the reason for the decrease of stress.

Further stretching, Cu2–Sn2 and Cu3–Cu4 bonds contribute to the increase of stress, and the normal stress reaches the maximum when the strain is 0.2. After that, d_{12}, Cu2–Sn2 and Cu3–Cu4 bonds begin to decrease with increasing strain, while d_{23} and d_{34} increase sharply. This indicates that the interface structure begins to break down. Eventually, the fracture near the interface (d_{23}) occurs earlier than inside the bulk Li$_2$CuSn (d_{34}), which suggests that the interfacial segregation of Li-ions makes the Li–Sn bonds near the interface weaker than the Li–Li bonds in bulk Li$_2$CuSn (Figure 6.13).

One-layer Li atoms adhered to Cu substrate suggests the occurrence of adhesive transfer in fractured interface geometries, like the case in Li$_x$Sn/Cu interface. The cohesion energy of bulk Li$_2$CuSn (1.04 J m^{-2}) is approximate twice the surface energy of Li$_2$CuSn(111). The W_{sep} of Li$_2$CuSn/Cu interface (1.54 J m^{-2}) is much larger than

the cohesion energy. From the ratio (1.48) of W_{sep} to the cohesion energy, the adhesive transfer is more likely to happen for Li_2CuSn/Cu interface, which is consistent with simulation results. Similarly, the adhesive transfer would happen for Cu_6Sn_5/Cu and Cu_3Sn/Cu interfaces due to their ratios of 1.22 and 1.14 J m^{-2}, respectively. The value (1.03) of W_{sep}/W_{dec} also confirms the adhesive transfer (see Figure 6.16).
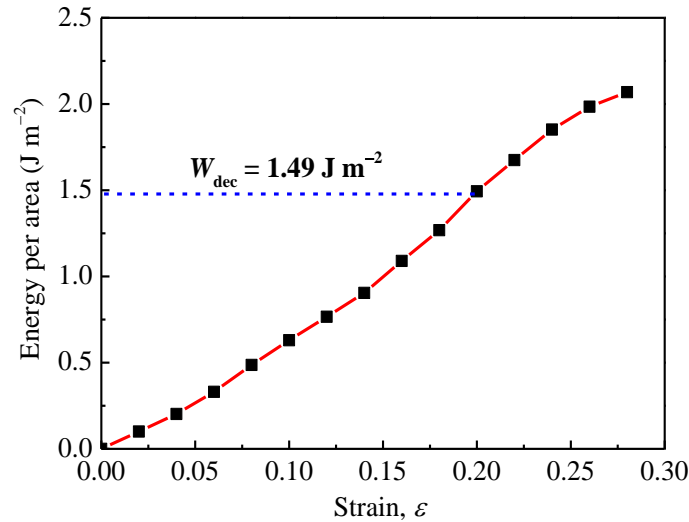
Figure 6.16 Energy per area (J m^{-2}) of Li_2CuSn/Cu interface *versus* strain.

Since actual electrode-collector interface usually contains a small amount of Cu_xSn alloys, thus, a comparison study between Li_xSn/Cu and Cu_xSn/Cu interfaces could provide the more actual interface mechanical properties of electrode-collector. For pure Li_xSn/Cu interfaces, the segregation of Li-ions at interface causes the evolution of interfacial bonding from Cu–Sn to weak Li–Cu metallic bonds and weak Li–Sn bonds near the interface. This leads to the weakened interface strength upon lithiation and fracture of the interfacial structure near the interface region. Due to the brittle properties of Li_xSn alloys, interfacial structures tend to brittle failure during the lithiation process [240]. Similarly, fracture of Cu_xSn/Cu interfaces occurs near the interface region instead of at interface due to the segregation of Li-ions. But the ductile properties of Cu_xSn alloys make Cu_xSn/Cu interface show a ductile fracture. Furthermore, Cu_xSn/Cu interfaces demonstrate enhanced W_{sep} and deformation

resistance at large strains comparing to that of Li_xSn/Cu interfaces. Since a small change of interface properties at the atomic scale could induce a significant change of toughness at the macroscopic scale [277]. Therefore, the enhancement of W_{sep} and stress-strain behaviours can contribute to the increase of interface toughness. This is the reason why the improved electrochemical performance was observed in Cu_xSn containing composite electrodes [263, 264, 278].

6.6 Conclusions

This chapter includes systematic research on the effects of Cu_xSn alloys on the interface strength and fracture behaviour of electrode-collector. The study shows that Cu_xSn alloys formed between Sn active materials and Cu current collector largely strengthen the interface strength. The W_{sep} of Cu_6Sn_5/Cu and Cu_3Sn/Cu interfaces are respectively 1.73 and 1.74 $J\,m^{-2}$, which is 9% higher than that of Sn/Cu interface. This is attributed to the more Cu–Cu metallic bonds in Cu_xSn/Cu interfaces. The W_{sep} of Li_2CuSn/Cu interface also reveals the weakening effects of lithiation on the electrode-collector interface. The stress-strain curve of Li_2CuSn/Cu interface shows that the maximum tensile stress is 5.81 GPa and the corresponding tensile strain is 0.20. The interface structure breaks completely when the strain is 0.28, which is much larger than the fracture strain (0.16) of LiSn/Cu interface. This indicates a stronger deformation resistance to tension. Like Li_xSn/Cu interface, the segregation of Li-ions makes the fracture of Li_2CuSn/Cu interface occur near the interface region, not at interface and Li_2CuSn/Cu interface displays ductile fracture which is different from the brittle fracture of Li_xSn/Cu interface. This study deepens our understanding of the effects of Cu_xSn alloys on the failure of electrode-collector interface. The results have important reference value for further understanding the interfacial failure of Sn anode materials and studying the Cu_xSn alloys containing electrode materials. The higher W_{sep} and stronger deformation resistance of Cu_xSn/Cu interfaces explain the excellent capacity and electrochemical cycling performance of Cu_xSn composite electrode materials.

Chapter 7

Enhancement effects of Co on interface properties of electrode-collector

Abstract

The Co doping effects on the interface strength of Sn electrode-collector interface for lithium-ion batteries are investigated by using first-principles calculations. The results demonstrate that by forming strong chemical bonds with interfacial Sn, Li and Cu atoms, Co doping in the interface region can enhance interface strengths and stabilities during lithiation. With doping, the highest strengths of Sn/Cu (1.74 J m^{-2}) and LiSn/Cu (1.73 J m^{-2}) interfaces are 9.4% and 17.7% higher than those of the corresponding interface systems before doping. Besides, Co doping can reduce interface charge accumulation and offset the decreasing interface strength during lithiation. Furthermore, the interface strength and electronic stability increase with rising Co content, while the increasing formation heat may result in thermodynamic instability. Based on the change of formation heat with Co content, an optimal Co doping content has been provided.

7.1 Introduction

In the previous studies, the effects of lithiation and Cu_xSn alloys on mechanical properties of electrode-collector interface were studied systematically. It is found that the interfacial segregation of Li-ions induced by interfacial charge accumulation is the main reason for the weakened interface strength during lithiation and the strong interface Cu–Sn and Cu–Cu bond are the reasons for enhanced interfacial strengths of Cu_xSn/Cu interface. Therefore, in order to improve the strength of electrode-collector interface and alleviate the weakening of interface strength during lithiation, the interfacial segregation of Li-ions can be weakened by (1) reducing the charge accumulation at interface or (2) forming strong chemical bonds at interface to enhance interfacial bonding strength, or using both methods at the same time. In addition, in the studies of chapters 4 and 5, charge accumulation at interface leads to the weakening of Li–Sn chemical bonds near the interface region, resulting in the fracture of interface structure near the interface region. Therefore, reducing charge accumulation at interface can not only alleviates the attenuation of interface strength of electrode-collector interface during lithiation, but also enhance the Li–Sn bonds near the interface region, thus improving the resistance of interface system to tensile deformation.

Doping, a versatile method to tailor material properties, has been widely used to regulate and control interfacial mechanical properties [279]. Recent studies about interface strength between metal oxides and metals show that interface strength can be enhanced by forming effective chemical bonds or facilitating charge transfer across interface. For example, combining first-principles calculation and scanning tunnelling microscopy, Shao *et al*. [280] elucidated that doping Mo in CaO lattice (by substituting Ca^{2+} with a Mo ion) improves interface strength between CaO and Au due to increased charge transfer at interface. Similarly, Song *et al*. [281] unveiled that doping Y, Nb and Pb can greatly improve the interface strength of $TiAl/TiO_2$ interface. The study of Co-doped SnO_2/Cu interface [282] shows that low valence ions (e.g., Cu^{2+} and Zn^{2+})

strengthen interface strength of SnO_2/Cu interface since these dopants form strong chemical bonds at interface and create defects such as holes in the lattice that help to trap electrons. A similar phenomenon was also found in Sb-doped SnO_2/Pt [283]. Also, Li *et al*. [282] revealed that doping high valence ions (e.g., Mo^{6+} and Sb^{5+}) in SnO_2/Cu interface impairs interface strength. Because these high valence ions produce excess electrons which deteriorate charge accumulation at interface. Besides, isovalence ions (such as Ti^{4+}) have negligible effects on interface strength due to the few charge transfer. Although Li_xSn/Cu interface is different from metal oxides/metals interface, its optimization mechanism is the same. That is, to enhance interface strength/interaction, measures should be taken to relieve charge accumulation at interface, which can be realized by enhancing charge transfer at interface and forming strong chemical bonds at interface.

Here, a low valence ion (Co^{2+}) is chosen to alleviate charge accumulation at interface and strengthen interface bonding. As a popular dopant, Co has been widely applied in electrode materials of LIBs. It is shown that Co doping can reduce particle sizes and suppress aggregation of active materials, and thus, effectively decrease diffusion distances of Li-ions and electrons [284, 285]. Besides, the formation of Co_xSn alloys (e.g., CoSn and $CoSn_2$) in electrode materials contributes cycling stability [286, 287]. The reaction of $CoSn_2$ alloy with Li forms composite electrodes composed of Co particles that act as buffer particles for the volume change during lithiation and delithiation processes. The inert CoSn alloy can help to accommodate volume deformation. Furthermore, Co_xSn alloys demonstrate strong hardness than that of Cu_xSn alloys and Sn metals, which would give a mechanical balance between ductility and brittleness of active materials and make active materials less vulnerable to pulverization. Hence, Co doping is expected to enhance the cycling ability of electrode materials.

In this chapter, Co doping effects on interface stability and strength of electrode-collector interface are fully explored. Firstly, different doping sites of Co are studied.

Then, we evaluate the influence of Co content on interface properties. The interface bonding and electronic structures of doped systems are also investigated to reveal the micromechanism. This work provides a deep understanding of the enhancement mechanism of Co doping on the electrochemical performances of Sn anodes.

7.2 Interface models

Based on our previous research, Sn(100)/Cu(111) interface was selected to explore Co doping effects on interfacial mechanical properties of Sn anodes[276]. The influence of Co doping on interface strength of lithiated electrode-collector interface was explored by using the LiSn(001)/Cu(111) interface. As illustrated in Figure 7.1, three interfacial doping sites were chosen in the Sn/Cu interface. For the LiSn/Cu system, it also contained the substitution of Co at the Li1 site. For the sake of simplicity, Sn/Cu-Co(Sn1) was used to indicate substituting a Co atom of a Sn atom in the first Sn layer near interface, and so on. The relaxed Sn(100)/Cu(111) and LiSn(001)/Cu(111) interface structures were taken from our previous work [276]. The 5×4×1 and 2×6×1 *k*-grids were respectively used for these two interfaces.
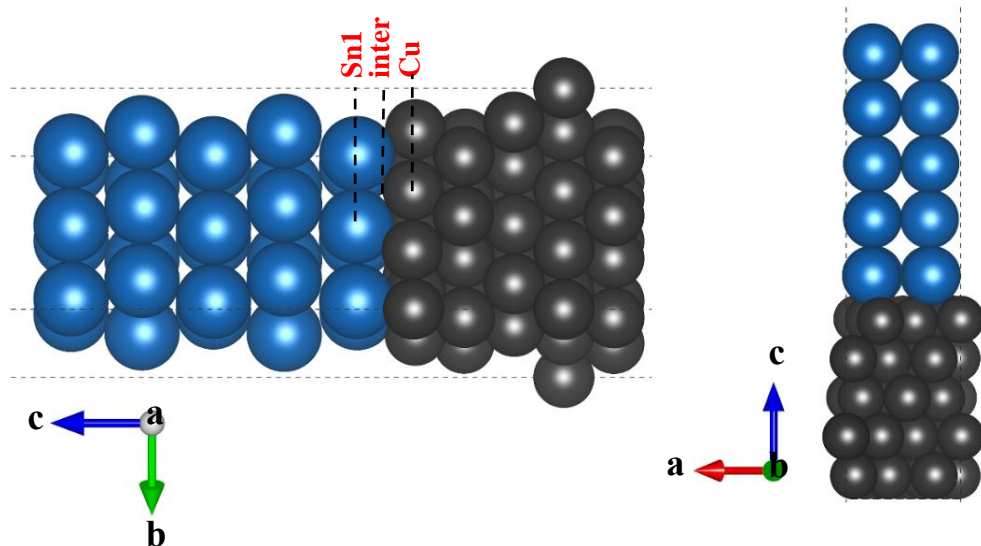
Figure 7.1 Relaxed Sn/Cu interface with three different interfacial doping sites. That is, substituting a Co atom of a Sn atom (or a Cu atom) in the first interfacial Sn (Sn1) or Cu (Cu1) layer, and doping a Co atom in the interfacial site (inter) of Sn/Cu interface.

114

The thermodynamic stabilities of doped interfaces are evaluated by formation heat (ΔH_f), which is defined as

$$\triangle H_\text{f} = (E_\text{Sn-Co-Cu} - E_\text{Sn-Cu} + E_x - E_\text{Co})/N \ , \qquad (7.1)$$

where $E_\text{Sn-Co-Cu}$ and $E_\text{Sn-Cu}$ are the total energies of Sn/Cu interfaces with and without Co doping, respectively, E_x is the total energy of one substituted Sn or Cu atom in bulk Sn or Cu, E_Co is the energy per atom in bulk Co, and N is the total number of atoms in the interface model. The negative ΔH_f corresponds to thermodynamically favourable structures and exothermic reactions while positive values refer to endothermic reactions and thermodynamically unstable structures.

7.3 Structures of Co-doped Sn/Cu and LiSn/Cu interfaces

As seen in Figure 7.2a, Co doping at the interfacial site tends to move to the first Sn layer (Sn1) and it forms strong chemical bonds with its neighbouring Sn and Cu atoms. The strong Sn–Co bonds influence Sn–Sn bonds near the interface region. As highlighted by the red rectangle, obvious distortions of Sn–Sn bonds are observed in the lattice and two holes are created. Based on the study of Cu-doped SnO_2/Cu interface, these holes are helpful to regulate the interface charge distribution, which enhances the interface interaction [282]. The interface spacing (d_{12}) varies from 2.41 Å to 2.37 Å due to newly formed Cu–Co bonds at interface. The strong Sn–Co bonds shorten the interlayer distance (d_{23}) between Sn1 and Sn2 atom layers by 19%. Furthermore, positions of Sn2 atoms are obviously moved along the c direction. d_{34} is decreased by 4% while d_{45} is slightly lengthened from 2.99 Å to 3.07 Å. On Sn/Cu-Co(Sn1) interface (Figure 7.2b), strong Cu–Co and Sn–Co bonds decrease d_{12} and d_{23} by 4% and 1%, respectively, and slightly increase d_{34} and d_{45} (1%). Comparing with Sn/Cu-Co(inter) and Sn/Cu-Co(Sn1) interfaces, substitution of Co at the Cu1 site only slightly shortens d_{12} and lengthens d_{23}, d_{34} and d_{45} by 1% (see Figure 7.2c).
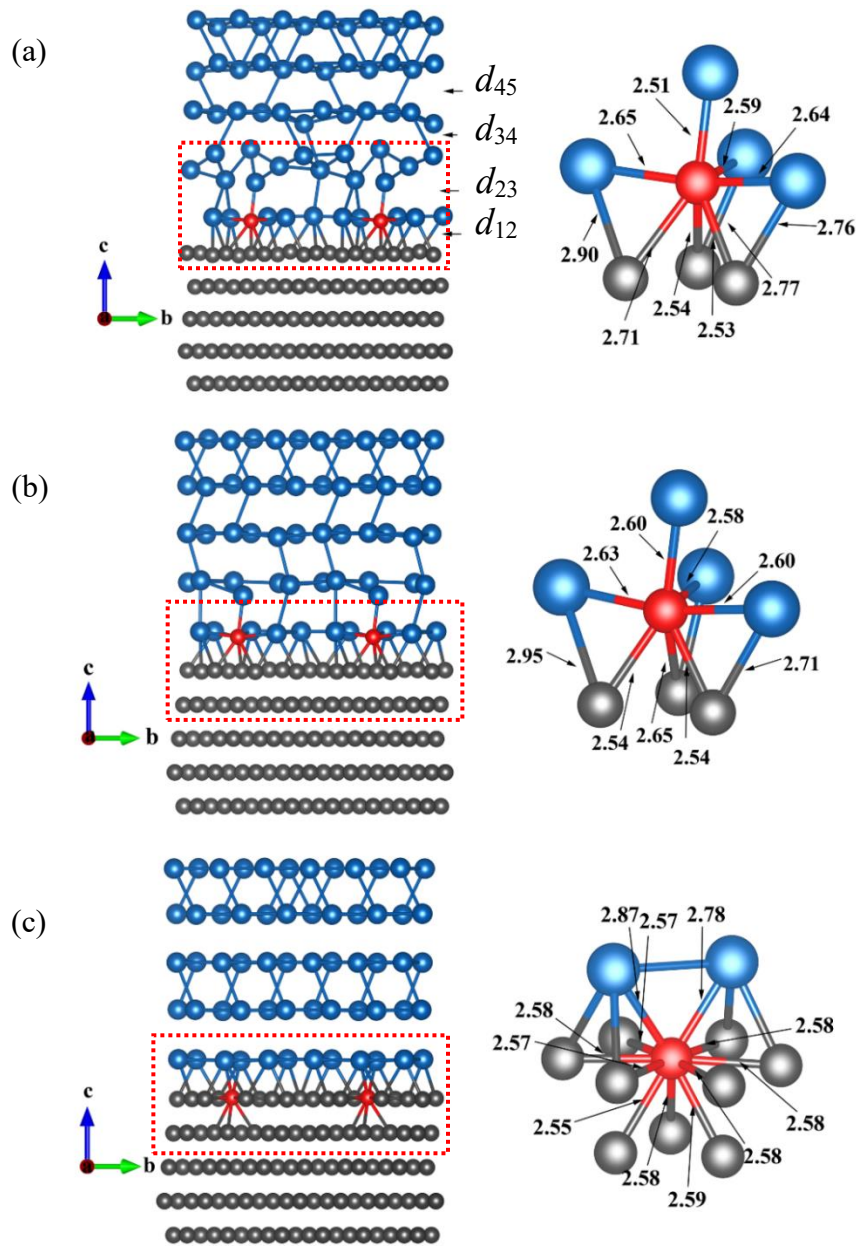
Figure 7.2 Relaxed (a) Sn/Cu-Co(inter), (b) Sn/Cu-Co(Sn1) and (c) Sn/Cu-Co(Cu1) (1×2) interface supercells. The main Sn–Co and Cu–Co bonds formed in these interfaces and their corresponding bond lengths are shown separately in enlarged views.

Comparing with Sn/Cu-Co(inter) and Sn/Cu-Co(Sn1) interfaces, substitution of Co at the Cu1 site only slightly shortens d_{12} and lengthens d_{23}, d_{34}, and d_{45} by 1% (see Figure 7.2c). The average bond lengths of Sn–Co and Cu–Co bonds in Sn/Cu-Co(inter),

Sn/Cu-Co(Sn1) and Sn/Cu-Co(Cu1) are 2.60, 2.60, 2.83 Å and 2.59, 2.58, 2.58 Å, respectively, which show that the Sn–Co bonds in Sn/Cu-Co(Cu1) are relatively weak while the Sn–Co and Cu–Co bonds in Sn/Cu-Co(Sn1) and Sn/Cu-Co(inter) have similar bond lengths. This will result in the similar interface strength of Sn/Cu-Co(Sn1) and Sn/Cu-Co(inter) and slight weak interface strength of Sn/Cu-Co(Cu1).

(a)   (b)   (c)   (d)
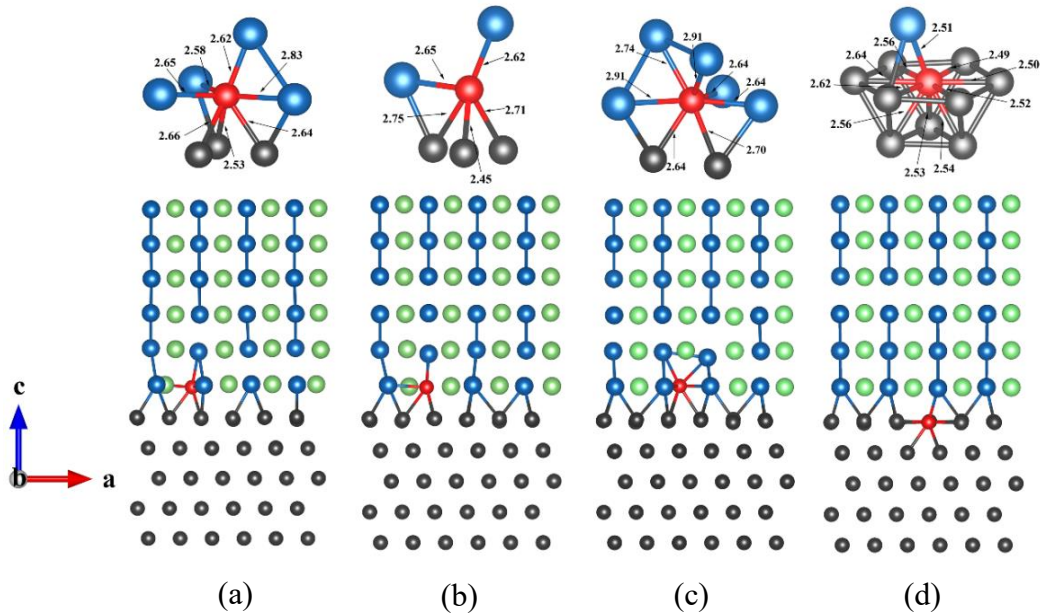
Figure 7.3 Relaxed (a) LiSn/Cu-Co(inter), (b) LiSn/Cu-Co(Sn1), (c) LiSn/Cu-Co(Li1) and (d) LiSn/Cu-Co(Cu1) interfaces. The main Sn–Co and Cu–Co bonds and their bond lengths on these interfaces are illustrated separately.

Similarly, strong Sn–Co and Cu–Co bonds formed on Co-doped LiSn/Cu interfaces reduce the interfacial spacing (d_{12}) (see Figure 7.3). Different from Co-doped Sn/Cu interfaces, doping has less influence on interface structures due to less strong Sn–Co bonds. Co doping at interfacial site also moves to the Sn1 layer, which is similar to the case of Co-doped Sn/Cu interface. From the variations of interlayer distances, only a few chemical bonds in the interior of LiSn slabs were slightly weakened with d_{ij} lengthened by less than 3%, and most chemical bonds were enhanced (d_{ij} shortened by 2% ~ 4%).

7.4 Thermodynamic stability and interface strength

As illustrated in Table 7.1, the negative $\triangle H_f$ (–0.05 kJ mol^{-1}) of Sn/Cu-Co(Sn1) interface means that substituting Co at Sn1 site is thermodynamically favourable. The small positive $\triangle H_f$ at interfacial (0.37 kJ mol^{-1}) and Cu1 (0.08 kJ mol^{-1}) sites indicate that doping in these sites is thermodynamically unstable and endothermic reactions. Similar phenomena are observed on most Co-doped LiSn/Cu interfaces except LiSn/Cu-Co(Cu1) that displays negative $\triangle H_f$. However, the small positive $\triangle H_f$ of these interfaces suggests that Co doping in these sites is easy to happen. Besides, the decreased total energies of these two doped systems imply that Co doping increases the electronic stabilities of interfaces (see Table 7.1).

Then, Co doping effects on interface strength were evaluated by the work of separation (W_{sep}). As summarized in Table 7.1, interface strengths are improved after doping. Co doping at Sn1, interfacial and Cu1 sites enhances the W_{sep} of Sn/Cu interface by 8.8%, 9.4% and 7.5%, respectively. Doping at interfacial site displays the highest W_{sep} (1.74 J mol^{-1}). For LiSn/Cu interface, the enhancement effect is more obvious. Interface is the most favourable doping site with W_{sep} increased by 17.7%. Co doping at Sn1 and Li1 sites strengthens W_{sep} by 17.0% and 11.6%, respectively, while that of Cu1 site demonstrates a slightly weak enhancement effect (5.4%).

To have a systematic description on Co doping effects, we further conducted Co doping in the interior of active materials and Cu current collector by substituting a Co atom of a Sn (or Cu) atom in the second interfacial Sn or Cu layer. On Co-doped LiSn/Cu interface, the substitution of Co at the Li2 site was also made. As shown in Table 7.1, on Co-doped Sn/Cu and LiSn/Cu interfaces, Co doping in the interior of active materials and current collector impairs the interface strength. Doping in Sn2 and Cu2 sites of Sn/Cu interface decreases W_{sep} by –5.7% and –0.6%, respectively. The attenuation of LiSn/Cu interface strengths after doping is in the range of –3.4% ~ –0.7%. In addition, the changes of total energies and $\triangle H_f$ of Sn/Cu-Co(Sn2) and Sn/Cu-

Co(Cu2) interfaces reveal that Co doping in Sn active material and Cu current collector decreases electronic and thermodynamic stability of Sn/Cu system.

Table 7.1 The change of total energies ($\triangle E_{tot}$), formation heat ($\triangle H_f$) and work of separation (W_{sep}) of Co-doped Sn/Cu and LiSn/Cu interfaces. The total energies and W_{sep} of Sn/Cu (-297.73 eV, 1.59 J m^{-2}) and LiSn/Cu (-371.49 eV, 1.47 J m^{-2}) interfaces are used as references to calculate $\triangle E_{tot}$ and $\triangle W_{sep}/W_{sep}$.

Interfaces	$\triangle E_{tot}$ (eV)	$\triangle H_f$ (kJ mol^{-1})	W_{sep} (J m^{-2})	$\triangle W_{sep}/W_{sep}$
Sn/Cu-Co(Sn2)	0.96	4.66	1.50	–5.7%
Sn/Cu-Co(Sn1)	–2.96	–0.05	1.73	8.8%
Sn/Cu-Co(inter)	–6.58	0.37	1.74	9.4%
Sn/Cu-Co(Cu1)	–3.10	0.08	1.71	7.5%
Sn/Cu-Co(Cu2)	1.31	5.38	1.58	–0.6%
LiSn/Cu-Co(Sn2)	–2.00	0.82	1.46	–0.7%
LiSn/Cu-Co(Li2)	–4.27	0.63	1.42	–3.4%
LiSn/Cu-Co(Sn1)	–2.07	0.75	1.72	17.0%
LiSn/Cu-Co(Li1)	–4.41	0.52	1.64	11.6%
LiSn/Cu-Co(inter)	–6.82	0.06	1.73	17.7%
LiSn/Cu-Co(Cu1)	–3.21	–0.04	1.55	5.4%
LiSn/Cu-Co(Cu2)	–3.04	0.12	1.45	–1.4%

7.5 Interface bonding and electronic structures

To understand micromechanism of enhanced interface strengths, Bader charge analysis was applied to evaluate chemical bonding in these interface systems [238]. As seen in Table 7.2, Sn atoms on Sn/Cu interface transfer 0.58 electrons (e) to Cu atoms and there is strong Cu–Sn ionic bonds. When Co doping at Sn1 and interfacial sites, Sn atoms respectively donate 0.49 and 0.47 e to Co atoms in these two systems and they form strong ionic bonds at interface, which slightly weaken Cu–Sn bonds at interface. Similarly, although Cu–Sn ionic bonds at interface are weakened, substituting Co of Cu1 atoms forms strong Cu–Co bonds at interfaces. Thus, strong Sn–Co or Cu–Co bonds are the reason for increased interface strengths. Co doping at Sn2 site has almost the same total charge transfer (~1.0 e) as that of Sn/Cu-Co(inter) interface. However, the strong Sn–Co bonds in Sn slab make little contribution to interface interaction and the formed Sn–Co bonds slightly weaken interfacial Cu–Sn bonds. The total net charges of Cu atoms in Sn/Cu-Co(Sn2) interface drop from –0.58 e (before lithiation) to –0.54 e. In Sn/Cu-Co(Cu2) interface, Sn atoms transfer fewer electrons (0.02 e) to Co and there are weak Sn–Co bonds which slightly decrease the charge transfer between Cu and Sn (~0.02 e). This results in weakened average interface bonding, leading to decreased W_{sep}.

The Bader charges on LiSn/Cu interfaces (see Table 7.2) show that in lithiated electrode-collector interface, Li atoms act as contributors of electrons and Li–Sn and Li–Cu ionic bonds play dominant roles. When doping at Sn1, Li1 and interfacial sites, Co forms strong ionic bonds with Li atoms. Although Li–Co bonds slightly weaken Li–Sn and/or Li–Cu bonds in these systems, the overall interface bonding is strengthened. The slight weak Li–Co bonds in LiSn/Cu-Co(Cu1) interface make W_{sep} increase slightly (5.4%). When Co doping at Sn2 site, the strong Li–Co ionic bonds formed in LiSn alloy weaken interfacial Li–Sn and Li–Cu bonds, resulting in decreased W_{sep} (–0.7%). The substitution of Co at Li2 site decreases the total charge transfer, and the Li–Sn bonds are weakened. Similarly, Co doping in current collector

weakens the interfacial Li–Cu ionic bonds with charge transfer changing from 1.42 e (before doping) to 1.37 e. This decreases the interface strength.

Table 7.2 Total net charges on elements of Co-doped Sn/Cu and LiSn/Cu interfaces. The negative values refer to obtained electrons.

Interface	Total net charge (e)			
	Cu	Sn	Co	Li
Sn/Cu interface	–0.58	0.58	–	–
Sn/Cu-Co(Sn2)	–0.54	1.03	–0.49	–
Sn/Cu-Co(Sn1)	–0.01	0.50	–0.49	–
Sn/Cu-Co(inter)	–0.53	1.00	–0.47	–
Sn/Cu-Co(Cu1)	–1.30	0.51	0.79	–
Sn/Cu-Co(Cu2)	–0.56	0.58	–0.02	–
LiSn/Cu interface	–1.42	–18.89	–	20.31
LiSn/Cu-Co(Sn2)	–1.37	–18.12	–0.79	20.28
LiSn/Cu-Co(Li2)	–1.43	–17.66	–0.38	19.47
LiSn/Cu-Co(Sn1)	–1.50	–18.30	–0.49	20.29
LiSn/Cu-Co(Li1)	–1.21	–17.91	–0.33	19.45
LiSn/Cu-Co(inter)	–1.28	–18.49	–0.46	20.23
LiSn/Cu-Co(Cu1)	–1.33	–18.84	–0.15	20.32
LiSn/Cu-Co(Cu2)	–1.37	–18.91	–0.04	20.32

Comparing the charge transfer from Li to Cu atoms in the LiSn/Cu-Co(inter) system (1.28 e) with that (1.42 e) on LiSn/Cu interface, Co doping at interfacial site alleviates charge accumulation at interface. This can increase the interface interaction and enhance the Sn–Sn bonds near the interface region which will increase the fracture

strength of electrode-collector interface [94, 261, 276]. Furthermore, with the increase of Li content upon lithiation, Co would obtain more electrons. The enhanced Li–Co bonds can offset the decreasing interface strength upon lithiation. In addition, Co doping could enhance the reversibility of alloying/dealloying reaction of Sn and hinder aggregation of Sn and Li_xSn alloys. Electrode materials doped with Co show smaller particle sizes which facilitate the transfer of Li-ions and electrons, thus, Co doping is helpful for fast charging-discharging rate [285]. Furthermore, the buffer effect of Co and its Co_xSn alloys can relieve the volume deformation of Sn anodes[288, 289]. Considering all these merits, we believe that Co interface doping could be effective to decrease the volume change and delamination of Sn anodes during lithiation and delithiation processes, which will improve the cycle stability and capacity retention[285, 288-290].

Considering the highest W_{sep} of Co doping at interfacial sites, we further studied chemical bonding by using the projected Crystal Orbital Hamilton Population (pCOHP) analysis, which can provide detail information on orbital-pair interactions [291-293]. Here, negative values refer to bonding states while positive ones indicate antibonding states. The pCOHP of Sn/Cu interface (Figure 7.4a) illustrates pairwise interaction in bonding and antibonding states, which reflects delocalized Sn–Sn, Cu–Sn and Cu–Cu metallic bonds. The strong antibonding states around E_F reflect an electronic instability. When Co doping on Sn/Cu interface (Figure 7.4b), bonding and antibonding Cu–Cu, Cu–Sn and Sn–Sn levels are pushed up to higher energies. The Sn–Sn and Cu–Sn antibonding states at E_F change into bonding states, which increases the electronic stability of interfaces. From intensities of bonding peaks, Cu–Cu bonds are enhanced after doping while Sn–Sn (Figure 7.4b) and Cu–Sn (Figure 7.5b) bonds are weakened due to a fewer charge transfer, as described in Bader charge analysis. Besides, strong Sn–Co and slightly weak Cu–Co metallic bonds are formed at interface, as shown in amplified pCOHP of interface bonding (Figure 7.5b).
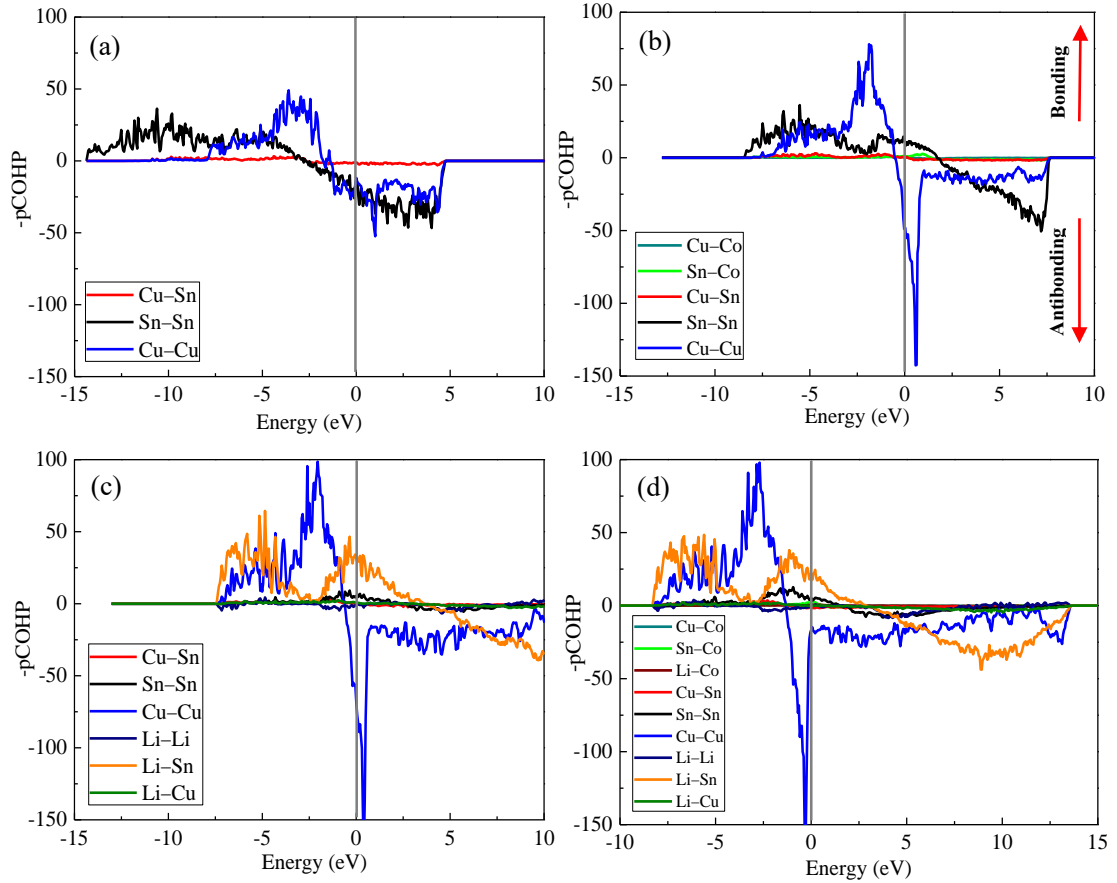
Figure 7.4 pCOHP analysis of (a) Sn/Cu, (b) Sn/Cu-Co(inter), (c) LiSn/Cu and (d) LiSn/Cu-Co(inter) interfaces.

In Figure 7.4c, the pCOHP of LiSn/Cu interface shows that after lithiation, Cu–Cu and Li–Sn bonding states in the valence band play the main roles while Sn–Sn bonding states are largely weakened. The Li–Sn bonding states at E_F imply the strong Li–Sn bonds. The interface bonding evolves from Cu–Sn bonds before lithiation to Cu–Sn and Li–Cu bonds, and Cu–Sn bonds are slightly receded (Figure 7.5c). The E_F falling in Sn–Sn and Cu–Sn bonding states indicates an increased electronic stability after lithiation.

The pCOHP of LiSn/Cu-Co(inter) interface (see Figures 7.4d and 7.5d) illustrates that E_F goes cross the newly formed Sn–Co and Li–Co bonding states, which indicates their strong chemical bonds at interface. In contrast, Li–Sn and Cu–Sn bonding states in the valence band are slightly decreased, and Cu–Sn and Li–Cu bonding and

antibonding levels are moved to lower energies. The Cu–Sn antibonding states at E_F reveal an electronic instability. The reason is that fewer charge transfer caused by formation of Li–Co, Sn–Co and Cu–Co bonds impairs Li–Sn, Li–Cu and Cu–Sn bonds. The decreased Li–Cu and slightly increased Sn–Sn bonding states confirm the reduced charge accumulation at interface [276]. Based on Bader charge and pCOHP analysis, strong Sn–Co, Cu–Co and Li–Co (for Co-doped LiSn/Cu interface) interfacial chemical bonds are the main reason for rising W_{sep}.
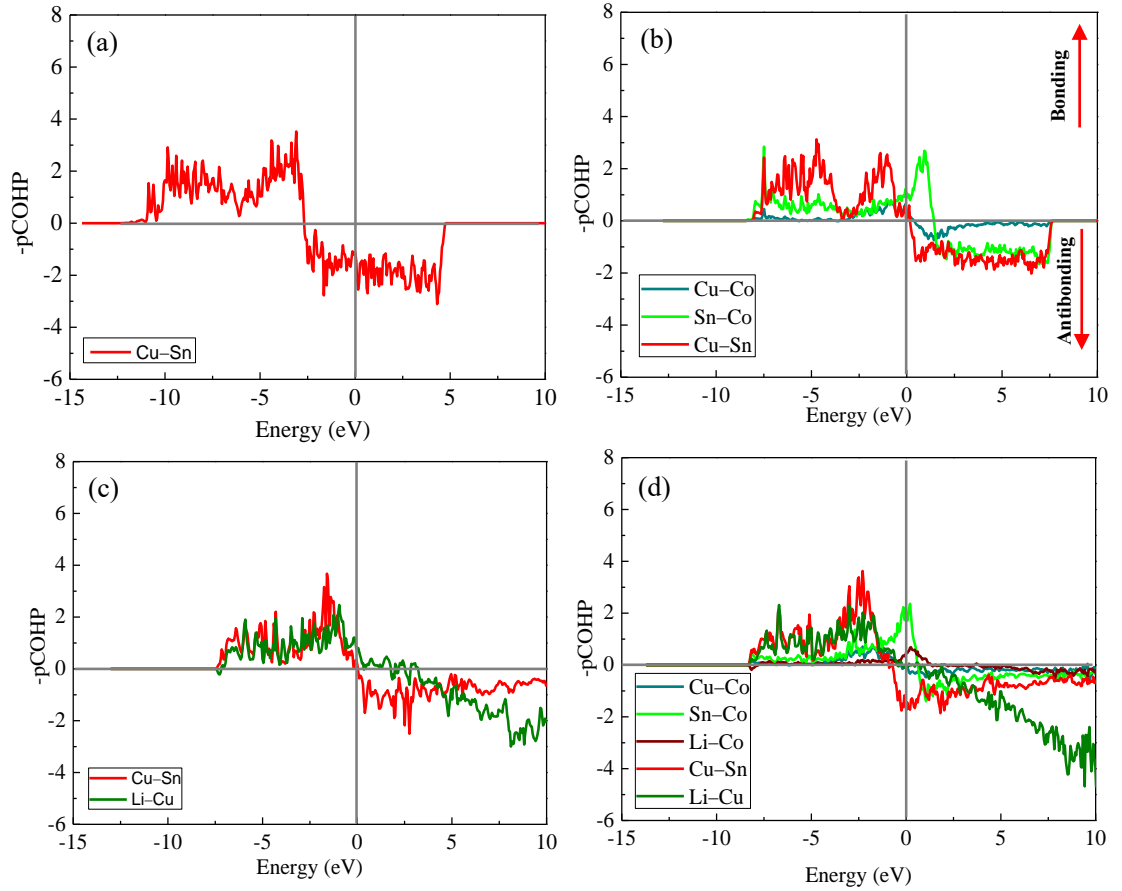
Figure 7.5   Amplified pCOHP of interface bonding for (a) Sn/Cu, (b) Sn/Cu-Co(inter), (c) LiSn/Cu and (d) LiSn/Cu-Co(inter) interfaces.

Then, we further investigated their electronic structures by analysing the total (TDOS) and partial density of states (PDOS). Several features can be revealed from TDOSs and PDOSs.

Firstly, as shown in Figure 7.6, the total DOSs display finite values at E_F, which

reveals metallic bonding in doped Sn/Cu interfaces. This is mainly contributed by Sn *p* states and Cu *d* states.
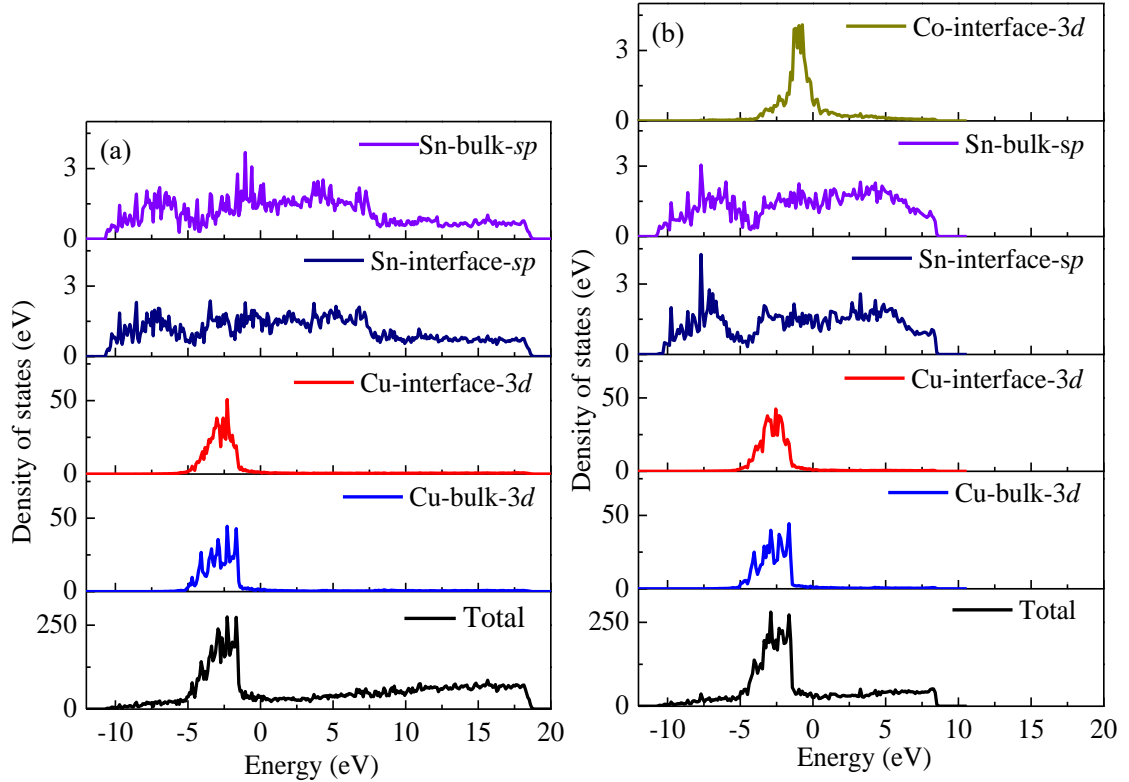
Figure 7.6 TDOS and PDOS of (a) Sn/Cu and (b) Sn/Cu-Co(inter) interfaces.

Secondly, comparing PDOSs of Cu and Sn atoms in interface and bulk layers, charge accumulation and depletion are observed in interfacial atom layers. Thus, interface bonding is mainly related to the interaction between the first interfacial Cu and Sn atom layers. The PDOS of interfacial Cu *d* states shows charge accumulation in the energy range of –5 ~ –1 eV. In contrast, there is some charge depletion in interfacial Sn *sp* states (–6 ~ 5 eV). This reflects the main ionic component of bonding across the interface. Besides, the small mixing of Cu *d* states and Sn *sp* states in the energy range of –10 ~ 18 eV indicates their weak covalent bonds.

Thirdly, Co doping changes interface interaction and a new Co peak appears at around –6 ~ 8 eV. There are small charge depletions in bulk Sn *sp* states from –2 to 5 eV and interfacial Cu *d* states at around –2.5 eV. And obvious charge depletions of interfacial and bulk Sn *sp* states and Cu *d* states are observed at the conduction band.

This indicates the ionic bonding. Besides, there is also small covalent mixing among Sn sp states, Co d states and Cu d states in the energy range of about $-7.5 \sim 8$ eV.
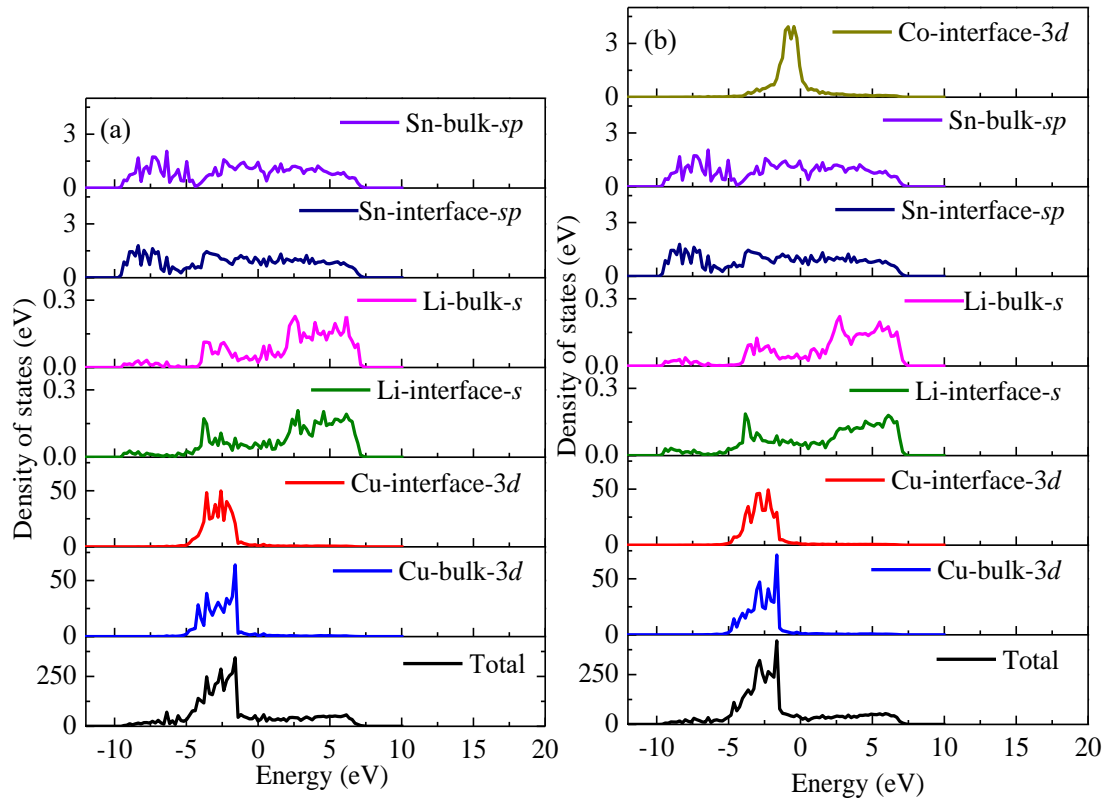
Figure 7.7   TDOS and PDOS of (a) LiSn/Cu and (b) LiSn/Cu-Co(inter) interfaces.

On LiSn/Cu interface, interfacial metallic bonding is also observed from TDOSs, which mainly comes from interfacial Sn p states and Cu d states (Figure 7.7a). The newly formed Li s levels at around -10 and 7.5 eV and the weakened Sn sp states in this energy range reflect Li–Sn ionic bonds. After Co doping, TDOS demonstrates enhanced peak strength in the valence band of $-4 \sim -2$ eV, suggesting the stronger chemical bonds in the interface system (Figure 7.7b). New Co 3d states appear in the energy range of $-7.5 \sim 7$ eV, which contribute metallic bonding at interface. On the contrary, small depleted states are observed in interfacial and bulk Sn sp states ($-7 \sim 6$ eV). For Li s states, charge depletion mainly occurs in the conduction band (at about $1 \sim 6$ eV). Thus, charge transfer from Li s levels to Co d levels enhances interface interaction while weakens Li–Sn bonds. The interfacial Cu d states are slightly weakened (at about $-4 \sim -2$ eV) and move a little to higher energy states due to fewer

charge transfer between Li and Cu atoms. The increased bulk Cu d states at around –3.75 ~ –1.75 eV is because of fewer charge accumulation at interface. Similar covalent hybridization also occurs among these atoms in the energy range from –5 to 7.5 eV.

7.6   Influence of Co contents on interface properties

Co doping effects on the electrode-collector interface were further investigated through the evolution of interface properties with increasing Co content on Sn/Cu interface. The obtained interface structures (Figure 7.8) show that all doped Co atoms at Sn/Cu interfacial site prefer to stay in interfacial Sn1 layer and they form strong chemical bonds with interfacial Sn and Cu atoms. Obvious distortions of chemical bonds and defects (such as holes) can be observed in the lattice, which can regulate interface charge distribution and enhance interface interaction. Rising Cu–Co bonds at interface decrease interface spacing (d_{12}) while d_{45} is slightly lengthened after doping.
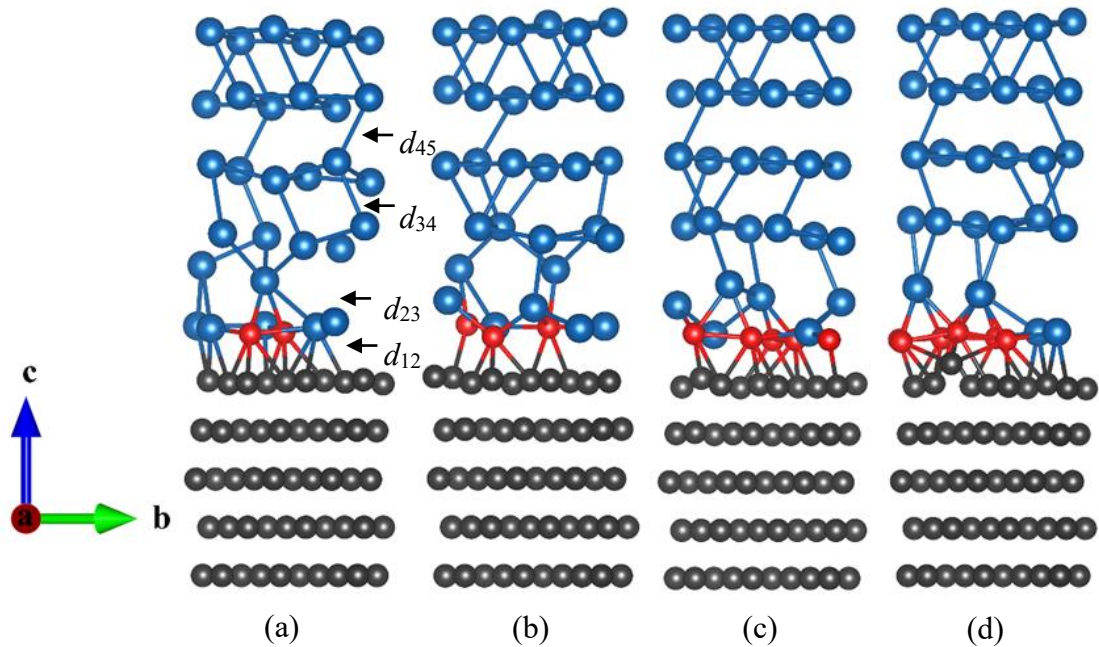
Figure 7.8   Relaxed Sn/Cu-Co(inter) interfaces with Co atom concentration of (a) 2.44%, (b) 3.61%, (c) 5.88% and (d) 6.98%.

Table 7.3 The $\triangle E_{tot}$, $\triangle H_f$, W_{sep} and $\triangle W_{sep}/W_{sep}$ of Sn/Cu-Co(inter) interfaces at different Co atom concentrations.

Co atom %	$\triangle E_{tot}$ (eV)	$\triangle H_f$ (kJ mol^{-1})	W_{sep} (J m^{-2})	$\triangle W_{sep}/W_{sep}$
1.23	−6.58	0.37	1.74	9.4%
2.44	−13.36	0.49	1.92	20.8%
3.61	−19.89	0.90	2.11	32.7%
4.76	−26.65	1.04	2.30	44.7%
5.88	−32.68	1.99	2.51	57.9%
6.98	−38.58	3.07	2.60	63.5%
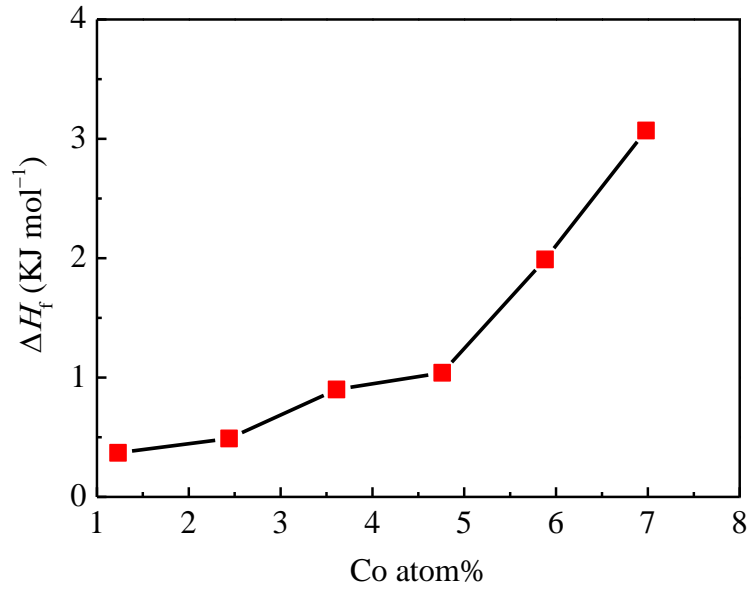
Figure 7.9 The change of $\triangle H_f$ of Sn/Cu-Co(inter) interface with rising Co content.

Besides, increasing Co content enhances the electronic stability and interface strength of the system (see Table 7.3). When Co concentration rises from 1.23% to 6.98%, total energies change from −6.58 to −38.58 eV. The corresponding W_{sep} increases from 1.74 to 2.60 J m^{-2}, with a total increase of 63.5%. However, $\triangle H_f$ keeps increasing with Co content. At Co content of 4.76%, $\triangle H_f$ is 1.04 kJ mol^{-1}, and then it

rises to 3.07 kJ mol^{-1} when the Co concentration reaches 6.98%. This implies that higher Co content makes Sn/Cu interfaces more thermodynamically unstable. Since Co atoms usually act as buffer particles with little contribution to capacity, its content should be small. As shown in Figure 7.9, for Co content less than 4.76%, $\triangle H_f$ increases slowly, and then it rises quickly. The sharp change of $\triangle H_f$ suggests that the doped interface system become thermodynamically unstable, which would seriously affect cyclic stability of electrode materials. Thus, 4.76% is estimated to be an optimal value, and the corresponding Co/Sn molar ratio is 0.13 [285].

Table 7.4 Total net charges on elements of Sn/Cu-Co(inter) interfaces at different Co atom concentrations.

Co atom %	Total net charge (e)		
	Cu	Sn	Co
1.23	–0.53	1.00	–0.47
2.44	–0.52	1.14	–0.62
3.61	–0.35	1.19	–0.84
4.76	–0.18	1.21	–1.02
5.88	–0.16	1.29	–1.13
6.98	–0.14	1.36	–1.22

Bader charge and pCOHP analysis of these interfaces were further conducted. As listed in Table 7.4, with increase of Co content, Sn atoms lose more electrons while Co atoms obtain increasing electrons, rising from 0.47 e at Co content of 1.23% to 1.22 e at Co concentration of 6.98%. This leads to fewer charge transfer between Sn and Cu atoms. Thus, increasing Co contents at interface largely enhance Sn–Co ionic bonds, which strengthen the interface strength but weaken Cu–Sn bonds. Similar results are seen in pCOHP of interface bonding. As seen in Figure 7.10, Cu–Sn bonding states in

the valence bands are gradually weakened while Sn–Co, Cu–Co and Co–Co bonding states become more and more intense. The strong bonding peaks at E_F indicate their strong chemical bonds.
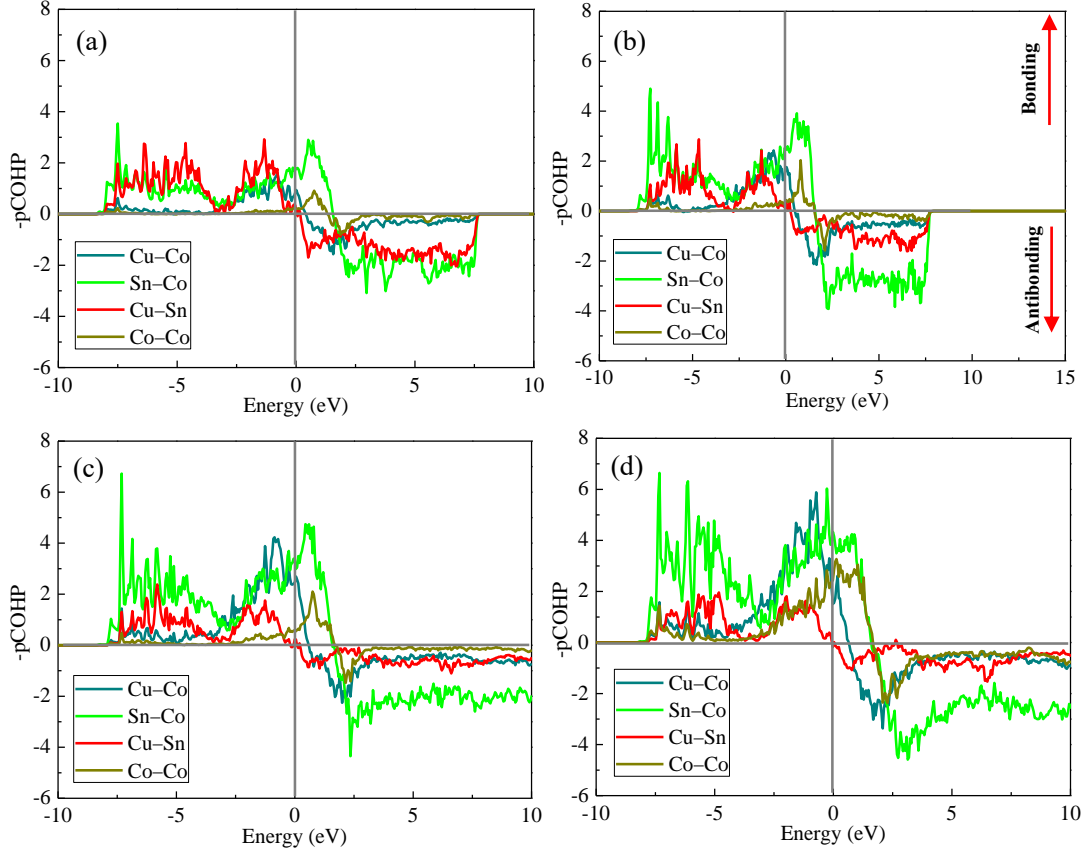
Figure 7.10 pCOHP analysis of interface bonding for Sn/Cu-Co(inter) interfaces with Co atom contents of (a) 2.44%, (b) 3.61%, (c) 5.88 and (d) 6.98%.

Based on previous studies [280-282] and our simulation, forming strong chemical bonds and facilitating charge transfer at interface are two ways to improve interface strength. In the case of Li_xSn/Cu interfaces, other low valence ions (e.g. Ni^{2+}, Cu^{2+}, Ag^+, Fe^{2+}), which can form strong chemical bonds with interfacial Sn, Cu and Li atoms, are expected to be effective to improve interface strength. Defects (e.g., holes with positive valence) induced by doping low valence ions would adjust the charge distribution at interface [282]. It is worth noting that, however, valence states of low valence ions should be lower than the maximum valence states of ions in an interface system. Therefore, valence states of dopants for Li_xSn/Cu interfaces should be less

than that of Sn^{4+}. Isovalence ions (e.g. Ti^{4+}) would have little influence on interface interaction due to few changes of charge distribution. In consideration of the various strengths of chemical bonds, different low valence ions may demonstrate varied enhancement effects. The result shows that substituting Ni and Ag of Sn1 atom respectively increases the interface strength by 5.4% and 2.3%, which confirms the optimization mechanism.

However, using dopants to improve the electrochemical behaviour of electrode-collector interfaces is only valid for interface with rigid current collector. In this kind of interface, the physical constraint of current collector to the large volume deformation of Sn active materials during lithiation and delithiation processes results in high stress at electrode-collector interface [134, 276]. The largely weakened interface strength and buildup of stress may exfoliate active materials from current collector. This causes an early capacity loss and poor cycle performance. Increasing interface strength by doping could relieve delamination of active materials. That is, high stress induced by volume change will be released by plastic deformation of current collector and disintegration of active materials[294, 295]. This avoids the sudden drop of capacity caused by loss of electric contact, and thus increases the capacity retention and cycling stability.

The van der Waals "slippery" interface is a new kind of electrode-collector interface, which is established through adding one or several layers of graphene between active material and current collector. The weak van der Waals force between graphene and current collector is found to be helpful to relieve exfoliation of active materials from current collector [296]. Because weak interface interaction allows slip of active materials during lithiation and delithiation, which largely decreases buildup of stress at electrode-collector interface [297]. However, stress in active materials caused by large volume change could result in cracking or disintegration of active materials. This will form isolated active materials 'islands' which disintegrate gradually with repeated cycles, leading to gradual capacity loss. Furthermore, weak

interaction between graphene and current collector induces 'gaps' between them. Thus, feasibility of such an electrode-collector interface to enhance the overall structural integrity and capacity retention still needs to be verified [296].

7.7 Conclusions

In this chapter, by using first-principles calculations, we have systematically studied Co doping effects on the interface strength of electrode-collector. The results show that Co doping at the interfacial site tends to move to the first Sn layer in the interface region, and Co doping in the interfacial region forms strong chemical bonds with the adjacent Sn, Li and Cu atoms, which regulates the charge distribution and chemical bonding in the interface region. Co doping in the interfacial region enhances the interface strength to different extent. Interface is the most favourable doping site that strengthens W_{sep} of Sn/Cu and LiSn/Cu interfaces by 9.4% and 17.7%, respectively. This is mainly due to strong Sn–Co, Cu–Co or Li–Co bonds formed in the interfacial region. Besides, strong Li–Co bonding could reduce charge accumulation on interface and offset the weakening interface strength during lithiation, which contributes to enhanced interface strength. In addition, increasing Co content leads to higher W_{sep} and electronic stability, but it also results in less thermodynamic stability. Through the change of formation heat with Co content, the optimal Co doping concentration is determined. The interface doping of Co has important reference significance for alleviating the stripping of electrode-collector interface during charge-discharge processes of three-dimensional composite electrodes and further improving the electrochemical cycle performance of Sn anode materials.

Chapter 8

Conclusions and perspectives

8.1　Conclusions

With the increasingly serious environmental problems and the decreasing of non-renewable energy, the development of clean new energy has become a global research upsurge. LIBs are widely used in new energy vehicles, consumer electronics, energy storage devices, aerospace and other fields because of their excellent electrochemical performance. The rapid development of new energy vehicles and the wide popularization of consumer electronic products have put forward higher requirements for the capacity, cycle performance and safety of LIBs. The current battery technology cannot meet the increasing capacity demand. Therefore, the research and development of high-capacity electrode materials have become the focus of researchers. Sn electrode materials have drawn much research attention due to their high theoretical capacities and are considered as promising anode materials for LIBs. However, Sn anode materials suffer from massive volume deformation during the lithiation and delithiation process, which leads to the cracking and crumbling of active materials, the exfoliation between Sn active materials and current collectors, and the repeated formation and fracture of SEI film. This directly results in severe capacity fade and poor cyclability. To make full use of high capacity Sn anode materials and realize the optimal design of electrode structures, it is necessary to deeply understand the failure micromechanism.

Therefore, in this thesis, we explore the evolution of mechanical properties of Sn anode materials during lithiation by using first-principles calculation, which is very important for deeply understanding the macroscopic failure behaviours. We first study the variations of mechanical properties of Sn active materials and electrode-collector interface. Combining the analysis of electronic structures, chemical bonding and charge transfer, this thesis systemically investigates the microscale mechanical degradation

mechanism of Sn anodes. Based on the obtained interface failure mechanism, an optimization to interface properties of electrode-collector is conducted by using dopants. The main conclusions from this thesis are as follows:

(1) bulk moduli of alloys decrease almost linearly with increasing Li content, which indicates that the resistant ability of Li_xSn alloys to volume compression is weakened during the lithiation processes. By contrast, the shear and Young's moduli and Poisson's ratio vary with Li concentration, which is attributed to the change of chemical bond strength with lithiation. In addition, Li_xSn alloys go through a ductile-brittle transformation during the lithiation processes and they demonstrate different anisotropy. When Li content is low, the anisotropy of alloys is small, and it increases slowly with the increase of Li content. At high Li content, the anisotropy of alloys varies largely. The largely weakened bulk moduli, the ductile-brittle transformation and the large difference of anisotropies of alloys at high Li content will result in the appearance of cracks on the surface of lithiated electrode materials. Besides, the difference between crystal structures and mechanical properties of alloys would induce a large mismatch-induced internal stress in electrode material, resulting in the fracture and pulverization of the electrode material.

(2) lithiation severely weakens the interface strength of electrode-collector interface. The W_{sep} decreases from 1.59 J m^{-2} (before lithiation) to 0.45 J m^{-2} where Li content is 0.78, reducing by ~70%. When Li content is low, W_{sep} decreases slowly with the increase of Li content. At Li concentration larger than 0.5, W_{sep} drops sharply due to the large anisotropy and brittleness of Li_xSn alloys. This is mainly due to the interfacial segregation of Li-ions upon lithiation, which leads to the gradual transformation of interfacial chemical bonds from strong Sn–Cu bonds to weak Li–Cu bonds. In addition, we investigate the stress-strain behaviour of LiSn/Cu interface. LiSn/Cu interface could withstand the maximum tensile stress of 6.42 GPa, and the corresponding strain is 0.12. Then, the interface breaks completely at the strain of 0.16. Due to the segregation of Li-

ions at interface, fracture occurs inside LiSn rather than at interface and the failure of most lithiated Sn/Cu interfaces occurs within Li_xSn slabs. Based on simulation results and a linear elastic fracture theory, we determine the relationship between the critical sizes of the core and shell and the state of charge to avoid fracture and debonding for Sn–Cu core-shell electrodes. This provides a reference example for the optimal design of other electrode structures.

(3) Cu_xSn alloys can greatly improve the interface strength of electrode-collector interface. The W_{sep} of Cu_6Sn_5/Cu and Cu_3Sn/Cu interface are 1.73 and 1.74 J m^{-2}, respectively, which increase the interface strength of electrode-collector interface by about 9%. This is mainly due to the existence of more Cu–Cu metallic bonds at Cu_xSn/Cu interface. The W_{sep} of Li_2CuSn/Cu interface shows that lithiation weakens the interface strength of electrode-collector interface. Besides, the stress-strain curve of Li_2CuSn/Cu interface shows that Cu_xSn alloys can increase the deformation resistance of electrode-collector at large strains. The maximum tensile stress of Li_2CuSn/Cu interface is 5.81 GPa at the strain of 0.20. Then, with the increase of strain, the stress decreases gradually. The interface structure is completely fragmented at the strain of 0.28, which is much larger than that (0.16) of LiSn/Cu interface. Similar to Li_xSn/Cu interface, due to the segregation of Li-ions at interface, the fracture of Cu_xSn/Cu interface occurs near the interface region, not at interface. The enhanced W_{sep} and deformation resistance make Cu_xSn containing composite electrodes show good cycle stability. This study deepens the understanding of the effect of Cu_xSn alloys on the failure of electrode-collector interface. The results have important reference value for further understanding the interface failure of Sn anode materials and further studying Cu_xSn containing composite electrodes.

(4) Co doping in the interfacial region can enhance the interface strength of the electrode-collector interface to different extent while Co doping in active materials and current collector deteriorates the interface strength. The interface site is the best doping position for Sn/Cu and LiSn/Cu interfaces. Co doping at interfacial site tends to move to

the first Sn layer at the interface region, and strong Sn–Co, Cu–Co or Li–Co bonds form in the interfacial region, which change the charge distribution and chemical bonding in the interface region, therefore, improving the interface strength. Co doping increases the W_{sep} of Sn/Cu and LiSn/Cu interface by 9.4% and 17.7%, respectively. In addition, the strong Li–Co bonds could reduce the charge accumulation at interface and offset the weakened interface strength during lithiation, which will contribute to enhanced interface strength. The doping of different Co content shows that the W_{sep} and electronic stability of the interface system increase with rising Co content, but the thermodynamic stability decreases. According to the variation of formation heat with Co content, the optimal Co doping content is given.

8.2   Perspectives

By using first-principles calculation, this thesis investigates the evolution of mechanical properties of active materials and the electrode-collector interface, as well as the micromechanical failure mechanism of Sn anode materials. But this thesis only contains some basic theoretical research. In order to make full use of Sn anode materials and control the massive volume deformation, future research should focus on the basic theoretical research of failure mechanism, the optimization design of electrode materials and the improvement of preparation processes. The basic theoretical research that can be carried out in the future is as follows:

(1) previous studies have shown that β-Sn transforms into α-Sn during lithiation, which in turn affects the properties of the formed alloys and electrode materials, however, the conditions under which the transition occurs and the factors affecting the transformation are unknown. Therefore, further study should focus on the lithiation mechanism of Sn anode materials to clarify the phase transitions and the corresponding influencing factors in the process of lithiation;

(2) this thesis investigates the evolution of mechanical properties of electrode

materials during lithiation processes from a microscopic point of view, but the actual battery is affected by the coupling of multiple physical fields (such as electrochemistry, mechanics and thermodynamics) in the processes of charge and discharge. Therefore, future research will focus on the evolution of electrode materials under multi-coupling fields, so as to have an in-depth understanding of the failure mechanism of Sn anode materials;

(3) because the properties of electrode materials can be affected by many factors, that is, electrode materials may exhibit completely different electrochemical behaviour under different external conditions. The future research will also study the influence of external factors such as pressure, temperature and radiation on the mechanical and thermodynamic properties of electrode materials and provide the microscopic mechanism;

(4) through theoretical simulations, this thesis optimizes the interfacial properties of electrode-collector interfaces by doping. But only Co doping is discussed in this thesis. In the next step, the interfacial modification of other elements should be investigated, and the optimization effects will be verified by experiments.

References

[1]   White paper on the development of lithium ion battery industry. China: China Electronic Information Industry Development Research Institute; 2018 (in Chinese).

[2]   Tarascon J-M, Armand M. Issues and challenges facing rechargeable lithium batteries. Nature. 2001; 414:359–369.

[3]   Dunn B, Kamath H, Tarascon J-M. Electrical energy storage for the grid: a battery of choices. Science. 2011; 334(6058):928.

[4]   Whittingham MS, Gamble Jr FR. The lithium intercalates of the transition metal dichalcogenides. Materials Research Bulletin. 1975; 10(5):363–371.

[5]   Kirchhoff B. On chemical analysis by spectrum-observations. Quarterly Journal of the Chemical Society of London. 1861; 13(3):270–289.

[6]   Li Z, Huang J, Liaw BY, Metzler V, Zhang JB. A review of lithium deposition in lithium-ion and lithium metal secondary batteries. Journal of Power Sources. 2014; 254:168–182.

[7]   Godshall NA, Raistrick ID, Huggins RA. Thermodynamic investigations of ternary lithium-transition metal-oxygen cathode materials. Materials Research Bulletin. 1980; 15(5):561–570.

[8]   Mizushima K, Jones PC, Wiseman PJ, Goodenough JB. Li_xCoO_2 ($0<x\leq1$): a new cathode material for batteries of high energy density. Materials Research Bulletin. 1980; 15(6):783–789.

[9]   Yazami R, Touzain P. A reversible graphite-lithium negative electrode for electrochemical generators. Journal of Power Sources. 1983; 9(3):365–371.

[10]   Thackeray MM, David WIF, Bruce PG, Goodenough JB. Lithium insertion into manganese spinels. Materials Research Bulletin. 1983; 18(4):461–472.

[11]   Nazri G-A, Pistoia G. Lithium batteries: science and technology: Springer Science & Business Media; 2008.

[12]   Voelcker J. Lithium batteries take to the road. IEEE Spectrum. 2007; 44(9):26–31.

[13]   Padhi AK, Nanjundaswamy KS, Goodenough JB. Phospho-olivines as positive-electrode materials for rechargeable lithium batteries. Journal of the Electrochemical Society. 1997; 144(4):1188–1194.

[14]   Padhi AK, Nanjundaswamy KS, Masquelier C, Okada S, Goodenough JB. Effect of structure on the Fe^{3+}/Fe^{2+} redox couple in iron phosphates. Journal of the Electrochemical Society. 1997; 144(5):1609–1613.

[15]   Armand M, Tarascon J-M. Building better batteries. Nature. 2008; 451(7179):652–657.

[16]   Mukhopadhyay A, Sheldon BW. Deformation and stress in electrode materials for Li-ion batteries. Progress in Materials Science. 2014; 63:58–116.

[17]   Arora P, Zhang Z. Battery separators. Chemical Reviews. 2004; 104(10):4419–4462.

[18]   Wang CP. Failure prediction of high-capacity electrode materials in lithium-ion batteries [dissertation]. Hunan (China): Xiangtan University; 2016 (in Chinese).

[19]   Guo BK, Li XH, Yang SQ. Chemical power supply: principle and manufacturing technology of battery. Changsha (China): Central South University Press 2009 (in Chinese).

[20]   Guo BK, Xu W, Wang XY, Xiao LX. Lithium-ion batteries. Changsha (China): Central South University Press 2005 (in Chinese).

[21]   Scrosati B, Garche J. Lithium batteries: status, prospects and future. Journal of Power Sources. 2010; 195(9):2419–2430.

[22]   Ellis BL, Lee KT, Nazar LF. Positive electrode materials for Li-ion and Li-batteries. Chemistry of Materials. 2010; 22(3):691–714.

[23]   Aifantis KE, Hackney SA, Kumar RV. High energy density lithium batteries: materials, engineering, applications: John Wiley & Sons; 2010.

[24]   Ashuri M, He Q, Shaw LL. Silicon as a potential anode material for Li-ion batteries: where size, geometry and structure matter. Nanoscale. 2016; 8(1):74–103.

[25]   Balbuena PB, Wang Y. Lithium-ion batteries: solid-electrolyte interphase: Imperial College Press; 2004.

[26]   Prosini PP, Lisi M, Zane D, Pasquali M. Determination of the chemical diffusion coefficient of lithium in $LiFePO_4$. Solid State Ionics. 2002; 148:45–51.

[27]   Yazami R, Lebrun N, Bonneau M, Molteni M. High performance $LiCoO_2$ positive electrode material. Journal of Power Sources. 1995; 54(2):389–392.

[28]   Nitta N, Wu F, Lee JT, Yushin G. Li-ion battery materials: present and future. Materials Today. 2015; 18(5):252−264.

[29]   Whittingham MS. Lithium batteries and cathode materials. Chemical Reviews. 2004; 104(10):4271–4302.

[30]   Daniel C, Mohanty D, Li J, Wood DL. Cathode materials review. AIP Conference Proceedings. 2014; 1597(1):26–43.

[31]   Nohma T, Kurokawa H, Uehara M, Takahashi M, Nishio K, Saito T. Electrochemical characteristics of $LiNiO_2$ and $LiCoO_2$ as a positive material for lithium secondary batteries. Journal of Power Sources. 1995; 54(2):522–524.

[32]   Rougier A, Gravereau P, Delmas C. Optimization of the composition of the $Li_{1-z}Ni_{1+z}O_2$ electrode materials: structural, magnetic, and electrochemical studies. Journal of the Electrochemical Society. 1996; 143(4):1168–1175.

[33]   Chen CH, Liu J, Stoll ME, Henriksen G, Vissers DR, Amine K. Aluminum-doped lithium nickel cobalt oxide electrodes for high-power lithium-ion batteries. Journal of Power Sources. 2004; 128(2):278−285.

[34]   Aurbach D, Levi MD, Gamulski K, Markovsky B, Salitra G, Levi E, Heider U, Heider L, Oesten R. Capacity fading of $Li_xMn_2O_4$ spinel electrodes studied by XRD and electroanalytical techniques. Journal of Power Sources. 1999; 81–82:472–479.

[35]   Xia Y, Zhou Y, Yoshio M. Capacity fading on cycling of 4 V $Li/LiMn_2O_4$ cells. Journal of the Electrochemical Society. 1997; 144(8):2593–2600.

[36]   Lee YJ, Park SH, Eng C, Parise JB, Grey CP. Cation ordering and electrochemical properties of the cathode materials $LiZn_xMn_{2-x}O_4$, $0<x\leq0.5$: a ^6Li magic-angle spinning NMR spectroscopy and diffraction study. Chemistry of Materials. 2002; 14(1):194–205.

[37] Lee KS, Myung ST, Bang HJ, Chung S, Sun YK. Co-precipitation synthesis of spherical $Li_{1.05}M_{0.05}Mn_{1.9}O_4$ (M = Ni, Mg, Al) spinel and its application for lithium secondary battery cathode. Electrochimica Acta. 2007; 52(16):5201–5206.

[38] Xu B, Qian D, Wang Z, Meng YS. Recent progress in cathode materials research for advanced lithium ion batteries. Materials Science and Engineering: R. 2012; 73:51–65.

[39] Ohzuku T, Makimura Y. Layered lithium insertion material of $LiCo_{1/3}Ni_{1/3}Mn_{1/3}O_2$ for lithium-ion batteries. Chemistry Letters. 2001; 30(7):642–643.

[40] Belharouak I, Sun Y-K, Liu J, Amine K. $Li(Ni_{1/3}Co_{1/3}Mn_{1/3})O_2$ as a suitable cathode for high power applications. Journal of Power Sources. 2003; 123(2):247–252.

[41] Shaju KM, Bruce PG. Macroporous $Li(Ni_{1/3}Co_{1/3}Mn_{1/3})O_2$: a high-power and high-energy cathode for rechargeable lithium batteries. Advanced Materials. 2006; 18(17):2330–2334.

[42] Yabuuchi N, Ohzuku T. Electrochemical behaviors of $LiCo_{1/3}Ni_{1/3}Mn_{1/3}O_2$ in lithium batteries at elevated temperatures. Journal of Power Sources. 2005; 146(1–2):636–639.

[43] Goriparti S, Miele E, De Angelis F, Di Fabrizio E, Proietti Zaccaria R, Capiglia C. Review on recent progress of nanostructured anode materials for Li-ion batteries. Journal of Power Sources. 2014; 257:421–443.

[44] Wu YP, Rahm E, Holze R. Carbon anode materials for lithium ion batteries. Journal of Power Sources. 2003; 114(2):228–236.

[45] Roy P, Srivastava SK. Nanostructured anode materials for lithium ion batteries. Journal of Materials Chemistry A. 2015; 3(6):2454–2484.

[46] Haik O, Ganin S, Gershinsky G, Zinigrad E, Markovsky B, Aurbach D, Halalay I. On the thermal behavior of lithium intercalated graphites. Journal of the Electrochemical Society. 2011; 158(8):A913–A923.

[47] Li H, Zhou H. Enhancing the performances of Li-ion batteries by carbon-coating: present and future. Chemical Communications. 2012; 48(9):1201–1217.

[48]   Fujimoto H, Tokumitsu K, Mabuchi A, Chinnasamy N, Kasuh T. The anode performance of the hard carbon for the lithium ion battery derived from the oxygen-containing aromatic precursors. Journal of Power Sources. 2010; 195(21):7452–7456.

[49]   Treacy MMJ, Ebbesen TW, Gibson JM. Exceptionally high Young's modulus observed for individual carbon nanotubes. Nature. 1996; 381(6584):678−680.

[50]   Yu M-F, Lourie O, Dyer MJ, Moloni K, Kelly TF, Ruoff RS. Strength and breaking mechanism of multiwalled carbon nanotubes under tensile load. Science. 2000; 287(5453):637−640.

[51]   Yang S, Huo J, Song H, Chen X. A comparative study of electrochemical properties of two kinds of carbon nanotubes as anode materials for lithium ion batteries. Electrochimica Acta. 2008; 53(5):2238−2244.

[52]   Morris RS, Dixon BG, Gennett T, Raffaelle R, Heben MJ. High-energy, rechargeable Li-ion battery based on carbon nanotube technology. Journal of Power Sources. 2004; 138(1):277−280.

[53]   DiLeo RA, Castiglia A, Ganter MJ, Rogers RE, Cress CD, Raffaelle RP, Landi BJ. Enhanced capacity and rate capability of carbon nanotube based anodes with titanium contacts for lithium ion batteries. ACS Nano. 2010; 4(10):6121–6131.

[54]   De Las Casas C, Li WZ. A review of application of carbon nanotubes for lithium ion battery anode material. Journal of Power Sources. 2012; 208:74−85.

[55]   Mauger A, Xie H, Julien CM. Composite anodes for lithium-ion batteries: status and trends. AIMS Materials Science. 2016; 3(3):1054–1106.

[56]   Pharr M, Zhao KJ, Wang XW, Suo ZG, Vlassak JJ. Kinetics of initial lithiation of crystalline silicon electrodes of lithium-ion batteries. Nano Letters. 2012; 12(9):5039−5047.

[57]   Lee SW, McDowell MT, Choi JW, Cui Y. Anomalous shape changes of silicon nanopillars by electrochemical lithiation. Nano Letters. 2011; 11(7):3034−3039.

[58]   Liu XH, Wang JW, Huang S, Fan F, Huang X, Liu Y, Krylyuk S, Yoo J, Dayeh SA, Davydov AV. In situ atomic-scale imaging of electrochemical lithiation in silicon. Nature Nanotechnology. 2012; 7(11):749−756.

[59]   Yoon S, Park C-M, Sohn H-J. Electrochemical characterizations of germanium and carbon-coated germanium composite anode for lithium-ion batteries. Electrochemical and Solid-State Letters. 2008; 11(4):A42−A45.

[60]   Baggetto L, Notten PH. Lithium-ion (de) insertion reaction of germanium thin-film electrodes: an electrochemical and in situ XRD study. Journal of the Electrochemical Society. 2009; 156(3):A169−A175.

[61]   Chen C-H, Chason E, Guduru PR. Numerical solution of moving phase boundary and diffusion-induced stress of Sn anode in the lithium-ion battery. Journal of the Electrochemical Society. 2017; 164(11):E3661−E3670.

[62]   Qaiser N, Kim YJ, Hong CS, Han SM. Numerical modeling of fracture-resistant Sn micropillars as anode for lithium ion batteries. The Journal of Physical Chemistry C. 2016; 120(13):6953–6962.

[63]   Hulikal S, Chen C-H, Chason E, Bower A. Experimental calibration of a Cahn-Hilliard phase-field model for phase transformations in Li−Sn electrodes. Journal of the Electrochemical Society. 2016; 163(13):A2647−A2659.

[64]   Benson J, Boukhalfa S, Magasinski A, Kvit A, Yushin G. Chemical vapor deposition of aluminum nanowires on metal substrates for electrical energy storage applications. ACS Nano. 2011; 6(1):118−125.

[65]   Liu Y, Hudak NS, Huber DL, Limmer SJ, Sullivan JP, Huang JY. In situ transmission electron microscopy observation of pulverization of aluminum nanowires and evolution of the thin surface Al_2O_3 layers during lithiation–delithiation cycles. Nano Letters. 2011; 11(10):4188−4194.

[66]   Obrovac MN, Chevrier VL. Alloy negative electrodes for Li-ion batteries. Chemical Reviews. 2014; 114(23):11444–11502.

[67]   Li WH, Sun XL, Yu Y. Si-, Ge-, Sn-based anode materials for lithium-ion batteries: from structure design to electrochemical performance. Small Methods. 2017; 1(3):1600037.

[68]   Zhang SL, Zhao KJ, Zhu T, Li J. Electrochemomechanical degradation of high-capacity battery electrode materials. Progress in Materials Science. 2017; 89:479–521.

[69]   McDowell MT, Ryu I, Lee SW, Wang C, Nix WD, Cui Y. Studying the kinetics of crystalline silicon nanoparticle lithiation with in situ transmission electron microscopy. Advanced Materials. 2012; 24(45):6034–6041.

[70]   Zhao KJ, Pharr M, Wan Q, Wang WL, Kaxiras E, Vlassak JJ, Suo ZG. Concurrent reaction and plasticity during initial lithiation of crystalline silicon in lithium-ion batteries. Journal of the Electrochemical Society. 2012; 159(3):A238–A243.

[71]   Chan CK, Peng H, Liu G, Mcilwrath K, Zhang XF, Huggins RA, Cui Y. High-performance lithium battery anodes using silicon nanowires. Nature Nanotechnology. 2008; 3(1):31–35.

[72]   Lee SW, McDowell MT, Berla LA, Nix WD, Cui Y. Fracture of crystalline silicon nanopillars during electrochemical lithium insertion. Proceedings of the National Academy of Sciences. 2012; 109(11):4080–4085.

[73]   Xie XQ, Kretschmer K, Zhang JQ, Sun B, Su DW, Wang GX. Sn@CNT nanopillars grown perpendicularly on carbon paper: a novel free-standing anode for sodium ion batteries. Nano Energy. 2015; 13:208−217.

[74]   Liang WT, Yang H, Fan FF, Liu Y, Liu XH, Huang JY, Zhu T, Zhang SL. Tough germanium nanoparticles under electrochemical cycling. ACS Nano. 2013; 7(4):3427–3433.

[75]   Ma H, Cheng F, Chen JY, Zhao JZ, Li CS, Tao ZL, Liang J. Nest-like silicon nanospheres for high-capacity lithium storage. Advanced Materials. 2007; 19(22):4067–4070.

[76] Nadimpalli SP, Sethuraman VA, Bucci G, Srinivasan V, Bower AF, Guduru PR. On plastic deformation and fracture in Si films during electrochemical lithiation/delithiation cycling. Journal of the Electrochemical Society. 2013; 160(10):A1885–A1893.

[77] Chen J. Recent progress in advanced materials for lithium ion batteries. Materials. 2013; 6(1):156–183.

[78] Wang JZ, Du N, Zhang H, Yu JX, Yang DR. Cu–Sn core-shell nanowire arrays as three-dimensional electrodes for lithium-ion batteries. The Journal of Physical Chemistry C. 2011; 115(47):23620−23624.

[79] Li L, Raji ARO, Tour JM. Graphene-wrapped MnO_2-graphene nanoribbons as anode materials for high-performance lithium ion batteries. Advanced Materials. 2013; 25(43):6298−6302.

[80] Reddy M, Yu T, Sow C-H, Shen ZX, Lim CT, Subba Rao G, Chowdari B. α-Fe_2O_3 nanoflakes as an anode material for Li-ion batteries. Advanced Functional Materials. 2007; 17(15):2792−2799.

[81] Chen JS, Zhu T, Yang XH, Yang HG, Lou XW. Top-down fabrication of α-Fe_2O_3 single-crystal nanodiscs and microparticles with tunable porosity for largely improved lithium storage properties. Journal of the American Chemical Society. 2010; 132(38):13162−13164.

[82] Reddy MV, Subba Rao GV, Chowdari BVR. Metal oxides and oxysalts as anode materials for Li ion batteries. Chemical Reviews. 2013; 113(7):5364–5457.

[83] Hu YS, Kienle L, Guo YG, Maier J. High lithium electroactivity of nanometer-sized rutile TiO_2. Advanced Materials. 2006; 18(11):1421−1426.

[84] Chen Z, Belharouak I, Sun YK, Amine K. Titanium-based anode materials for safe lithium-ion batteries. Advanced Functional Materials. 2013; 23(8):959–969.

[85] Wang B, Chen JS, Wu HB, Wang ZY, Lou XW. Quasiemulsion-templated formation of α-Fe_2O_3 hollow spheres with enhanced lithium storage properties. Journal of the American Chemical Society. 2011; 133(43):17146–17148.

[86]   Zhang LJ, Hu P, Zhao XY, Tian RL, Zou RQ, Xia DG. Controllable synthesis of core-shell Co@CoO nanocomposites with a superior performance as an anode material for lithium-ion batteries. Journal of Materials Chemistry. 2011; 21(45):18279–18283.

[87]   Nishi Y. Lithium ion secondary batteries; past 10 years and the future. Journal of Power Sources. 2001; 100(1–2):101–106.

[88]   Chon MJ, Sethuraman VA, McCormick A, Srinivasan V, Guduru PR. Real-time measurement of stress and damage evolution during initial lithiation of crystalline silicon. Physical Review Letters. 2011; 107(4):045503.

[89]   Limthongkul P, Jang Y-I, Dudney NJ, Chiang Y-M. Electrochemically-driven solid-state amorphization in lithium-silicon alloys and implications for lithium storage. Acta Materialia. 2003; 51(4):1103−1113.

[90]   Obrovac MN, Krause LJ. Reversible cycling of crystalline silicon powder. Journal of the Electrochemical Society. 2007; 154(2):A103–A108.

[91]   Li J, Dahn JR. An in situ X-ray diffraction study of the reaction of Li with crystalline Si. Journal of the Electrochemical Society. 2007; 154(3):A156–A161.

[92]   Wang Y, Zhang QL, Li DW, Hu JZ, Xu JG, Dang DY, Xiao XC, Cheng YT. Mechanical property evolution of silicon composite electrodes studied by environmental nanoindentation. Advanced Energy Materials. 2018; 8(10):1702578.

[93]   Shenoy VB, Johari P, Qi Y. Elastic softening of amorphous and crystalline Li–Si phases with increasing Li concentration: a first-principles study. Journal of Power Sources. 2010; 195(19):6825–6830.

[94]   Stournara ME, Xiao XC, Qi Y, Johari P, Lu P, Sheldon BW, Gao HJ, Shenoy VB. Li segregation induces structure and strength changes at the amorphous Si/Cu interface. Nano Letters. 2013; 13(10):4759–4768.

[95]   Wang H, Hou B, Wang X, Xia S, Chew HB. Atomic-scale mechanisms of sliding along an interdiffused Li–Si–Cu interface. Nano Letters. 2015; 15(3):1716–1721.

[96]   Chou C-Y, Kim H, Hwang GS. A comparative first-principles study of the structure, energetics, and properties of Li–M (M = Si, Ge, Sn) alloys. The Journal of Physical Chemistry C. 2011; 115(40):20018–20026.

[97]   Brassart L, Suo Z. Reactive flow in solids. Journal of the Mechanics and Physics of Solids. 2013; 61(1):61–77.

[98]   Ryu I, Choi JW, Cui Y, Nix WD. Size-dependent fracture of Si nanowire battery anodes. Journal of the Mechanics and Physics of Solids. 2011; 59(9):1717–1730.

[99]   Bucci G, Nadimpalli SP, Sethuraman VA, Bower AF, Guduru PR. Measurement and modeling of the mechanical and electrochemical response of amorphous Si thin film electrodes during cyclic lithiation. Journal of the Mechanics and Physics of Solids. 2014; 62:276–294.

[100]   Lu B, Song YC, Guo ZS, Zhang JQ. Modeling of progressive delamination in a thin film driven by diffusion-induced stresses. International Journal of Solids and Structures. 2013; 50(14–15):2495–2507.

[101]   Lu B. Diffusion induced stresses and delamination in thin film Li-ion batteries [dissertation on the internet]. Shanghai (China): Shanghai University; 2013 (in Chinese)

[102]   Zhang JQ, Lu B, Song YC. Fracture phenomenon and research progress of electrode materials for lithium ion batteries. Advances in Mechanics. 2017; 38(1):14–33 (in Chinese).

[103]   Wang PD, Zhang XY, Yang L, Zhang XY, Yang M, Chen HS, Fang DN. Real-time monitoring of internal temperature evolution of the lithium-ion coin cell battery during the charge and discharge process. Extreme Mechanics Letters. 2016; 9:459–466.

[104]   Lu YY, Ni Y. Effects of particle shape and concurrent plasticity on stress generation during lithiation in particulate Li-ion battery electrodes. Mechanics of Materials. 2015; 91:372–381.

[105] Li W, Cao K, Wang H, Liu J, Zhou L, Yao H. Carbon coating may expedite the fracture of carbon-coated silicon core-shell nanoparticles during lithiation. Nanoscale. 2016; 8(9):5254–5259.

[106] Zuo P, Zhao YP. Phase field modeling of lithium diffusion, finite deformation, stress evolution and crack propagation in lithium ion battery. Extreme Mechanics Letters. 2016; 9:467–479.

[107] Li H, Wang ZX, Huang XJ, Chen LQ. Size effects and surface/interface issues in lithium ion batteries. Physics. 2008; 37(6):416–420 (in Chinese).

[108] Cheng J, Li J, Jia M, Tang YW, Du SL, Ai LH, Yin BH, Ai L. Application status and future of multi-scale numerical models for lithium ion battery. Acta Physica Sinica. 2015; 64:210202 (in Chinese).

[109] Tang YW, Ai L, Cheng Y, Wang AA, Li SG, Jia M. Relaxation behavior simulation of power lithium-ion battery in high-rate charging-discharging process. Acta Physica Sinica. 2016; 65(5):058201 (in Chinese).

[110] Jiang YH, Ai L, Jia M, Cheng Y, Du SL, Li SG. Cyclic capacity fading of the power lithium ion battery based on a numerical modelling with dynamic responses. Acta Physica Sinica. 2017; 66(11):118202 (in Chinese).

[111] Peng YZ, Zhang K, Zheng BL, Li Y. Stress analysis of a cylindrical composition-gradient electrode of lithium-ion battery in generalized plane strain condition. Acta Physica Sinica. 2016; 65:100201 (in Chinese).

[112] Peng YZ, Li Y, Zhen BL, Zhang K, Xu YC. Influence of local velocity on diffusion-induced stress and axial reaction force in a hollow cylindrical electrode of lithium-ion batteries with cosidering expasion rate of medium. Acta Physica Sinica. 67(7):070203.

[113] Xie HM, Zhang Q, Song HB, Shi BQ, Kang YL. Modeling and in situ characterization of lithiation-induced stress in electrodes during the coupled mechano-electro-chemical process. Journal of Power Sources. 2017; 342:896–903.

[114] Ma Z, Wu H, Wang Y, Pan Y, Lu C. An electrochemical-irradiated plasticity model for metallic electrodes in lithium-ion batteries. International Journal of Plasticity. 2017; 88:188–203.

[115] Hu B. The thermal-chemo-mechanical coupled theory and finite element analysis of electrode materials in lithium-ion batteries [dissertation]. Hunan (China): Xiangtan University; 2017 (in Chinese).

[116] Zhang M, Wang T, Cao G. Promises and challenges of tin-based compounds as anode materials for lithium-ion batteries. International Materials Reviews. 2015; 60(6):330–352.

[117] Reichmann TL, Gebert C, Cupid DM. Investigation of the Li solubility in the intermediate phase $Li_{17}Sn_4$ relevant to understanding lithiation mechanisms in Sn-based anode materials. Journal of Alloys and Compounds. 2017; 714:593–602.

[118] Ma ZS, Zhou YC, Liu J, Xue DF, Yang QS, Pan Y. Research progress in degradation mechanism of silicon anode materials for lithium-ion batteries. Advances in Mechanics. 2013; 43(6):581–599 (in Chinese).

[119] Winter M, Besenhard JO. Electrochemical lithiation of tin and tin-based intermetallics and composites. Electrochimica Acta. 1999; 45(1):31–50.

[120] Courtney IA, Tse JS, Mao O, Hafner J, Dahn JR. Ab initio calculation of the lithium-tin voltage profile. Physical Review B. 1998; 58(23):15583.

[121] Goward GR, Taylor NJ, Souza DCS, Nazar LF. The true crystal structure of $Li_{17}M_4$ (M = Ge, Sn, Pb)-revised from $Li_{22}M_5$. Journal of Alloys and Compounds. 2001; 329(1–2):82–91.

[122] Hirai K, Ichitsubo T, Uda T, Miyazaki A, Yagi S, Matsubara E. Effects of volume strain due to Li–Sn compound formation on electrode potential in lithium-ion batteries. Acta Materialia. 2008; 56(7):1539–1545.

[123] Gonzalez J, Sun K, Huang M, Dillon S, Chasiotis I, Lambros J. X-ray microtomography characterization of Sn particle evolution during

lithiation/delithiation in lithium ion batteries. Journal of Power Sources. 2015; 285:205–209.

[124] Wang JW, Fan FF, Liu Y, Jungjohann KL, Lee SW, Mao SX, Liu XH, Zhu T. Structural evolution and pulverization of tin nanoparticles during lithiation-delithiation cycling. Journal of the Electrochemical Society. 2014; 161(11):F3019–F3024.

[125] Li QQ, Wang P, Feng Q, Mao MM, Liu JB, Mao SX, Wang HT. In situ TEM on the reversibility of nanosized Sn anodes during the electrochemical reaction. Chemistry of Materials. 2014; 26(14):4102–4108.

[126] Cui Y, Li T, Zhou X, Mosey A, Guo W, Cheng R, Fu Y, Zhu L. Electrochemical behavior of tin foil anode in half cell and full cell with sulfur cathode. Electrochimica Acta. 2019; 294:60–67.

[127] Sun F, Markoetter H, Zhou D, Alrwashdeh SSS, Hilger A, Kardjilov N, Manke I, Banhart J. In situ radiographic investigation of (de)lithiation mechanisms in a tin-electrode lithium-ion battery. ChemSusChem. 2016; 9(9):946–950.

[128] Wang JJ, Chen-Wiegart YC, Wang J. In situ three-dimensional synchrotron X-ray nanotomography of the (de)lithiation processes in tin anodes. Angewandte Chemie International Edition. 2014; 53(17):4460–4464.

[129] Qi Y, Harris SJ. In situ observation of strains during lithiation of a graphite electrode. Journal of the Electrochemical Society. 2010; 157(6):A741–A747.

[130] Ui K, Kikuchi S, Kadoma Y, Kumagai N, Ito S. Electrochemical characteristics of Sn film prepared by pulse electrodeposition method as negative electrode for lithium secondary batteries. Journal of Power Sources. 2009; 189(1):224–229.

[131] Im HS, Cho YJ, Lim YR, Jung CS, Jang DM, Park J, Shojaei F, Kang HS. Phase evolution of tin nanocrystals in lithium ion batteries. ACS Nano. 2013; 7(12):11103–11111.

[132] Yang FQ. Analysis of charging-induced structural damage in electrochemical systems. Physical Chemistry Chemical Physics. 2017; 19(10):7072–7077.

[133] Cook JB, Lin TC, Detsi E, Weker J, Tolbert SH. Using X-ray microscopy to understand how nanoporous materials can be used to reduce the large volume change in alloy anodes. Nano Letters. 2017; 17:870–877.

[134] Mukhopadhyay A, Kali R, Badjate S, Tokranov A, Sheldon BW. Plastic deformation associated with phase transformations during lithiation/delithiation of Sn. Scripta Materialia. 2014; 92:47–50.

[135] Liu DX, Wang JH, Pan K, Qiu J, Canova M, Cao LR, Co AC. In situ quantification and visualization of lithium transport with neutrons. Angewandte Chemie International Edition. 2014; 53(36):9498–9502.

[136] Christensen J. Modeling diffusion-induced stress in Li-ion cells with porous electrodes. Journal of the Electrochemical Society. 2010; 157(3):A366–A380.

[137] Woodford WH, Chiang Y-M, Carter WC. "Electrochemical shock" of intercalation electrodes: a fracture mechanics analysis. Journal of the Electrochemical Society. 2010; 157(10):A1052–A1059.

[138] Cheng Y-T, Verbrugge MW. Diffusion-induced stress, interfacial charge transfer, and criteria for avoiding crack initiation of electrode particles. Journal of the Electrochemical Society. 2010; 157(4):A508–A516.

[139] Rhodes KJ, Meisner R, Kirkham M, Dudney N, Daniel C. In situ XRD of thin film tin electrodes for lithium ion batteries. Journal of the Electrochemical Society. 2012; 159(3):A294–A299.

[140] Huang S, Fan F, Li J, Zhang S, Zhu T. Stress generation during lithiation of high-capacity electrode particles in lithium ion batteries. Acta Materialia. 2013; 61(12):4354–4364.

[141] Bhandakkar TK, Johnson HT. Diffusion induced stresses in buckling battery electrodes. Journal of the Mechanics and Physics of Solids. 2012; 60(6):1103–1121.

[142] Liu M. Finite element analysis of lithiation-induced decohesion of a silicon thin film adhesively bonded to a rigid substrate under potentiostatic operation. International Journal of Solids and Structures. 2015; 67–68:263–271.

[143] Wu H, Xie ZC, Wang Y, Lu CS, Ma ZS. Modeling diffusion-induced stress on two-phase lithiation in lithium-ion batteries. European Journal of Mechanics-A/Solids. 2018; 71:320–325.

[144] Chon MJ, Sethuraman VA, McCormick A, Srinivasan V, Guduru PR. Real-time measurement of stress and damage evolution during initial lithiation of crystalline silicon. Physical Review Letters. 107(4):045503.

[145] Kali R, Krishnan Y, Mukhopadhyay A. Effects of phase assemblage and microstructure-type for Sn/intermetallic 'composite' films on stress developments and cyclic stability upon lithiation/delithiation. Scripta Materialia. 2017; 130:105–109.

[146] Gonzalez JF, Antartis DA, Chasiotis I, Dillon SJ, Lambros J. In situ X-ray micro-CT characterization of chemo-mechanical relaxations during Sn lithiation. Journal of Power Sources. 2018; 381:181–189.

[147] Nam DH, Kim RH, Han DW, Kwon HS. Electrochemical performances of Sn anode electrodeposited on porous Cu foam for Li-ion batteries. Electrochimica Acta. 2012; 66:126–132.

[148] Liu XH, Zhong L, Huang S, Mao SX, Zhu T, Huang JY. Size-dependent fracture of silicon nanoparticles during lithiation. ACS Nano. 2012; 6(2):1522–1531.

[149] Cao K, Li PF, Zhang YZ, Chen TW, Wang X, Zhang SL, Liu JB, Wang HT. In situ TEM investigation on ultrafast reversible lithiation and delithiation cycling of Sn@C yolk-shell nanoparticles as anodes for lithium ion batteries. Nano Energy. 2017; 40:187–194.

[150] Zhang LQ, Liu XH, Liu Y, Huang S, Zhu T, Gui LJ, Mao SX, Ye ZZ, Wang CM, Sullivan JP, Huang JY. Controlling the lithiation-induced strain and charging rate in nanowire electrodes by coating. ACS Nano. 2011; 5(6):4800–4809.

[151] Barai P, Huang B, Dillon SJ, Mukherjee PP. Mechano-electrochemical interaction gives rise to strain relaxation in Sn electrodes. Journal of the Electrochemical Society. 2016; 163(14):A3022–A3035.

[152] Chen Q, Sieradzki K. Spontaneous evolution of bicontinuous nanostructures in dealloyed Li-based systems. Nature Materials. 2013; 12(12):1102.

[153] Huang JY, Zhong L, Wang CM, Sullivan JP, Xu W, Zhang LQ, Mao SX, Hudak NS, Liu XH, Subramanian A, Fan HY, Qi LA, Kushima A, Li J. In situ observation of the electrochemical lithiation of a single SnO_2 nanowire electrode. Science. 2010; 330(6010):1515–1520.

[154] Wu M, Li X, Zhou Q, Ming H, Adkins J, Zheng J. Fabrication of Sn film via magnetron sputtering towards understanding electrochemical behavior in lithium-ion battery application. Electrochimica Acta. 2014; 123:144–150.

[155] Guo M, Zhang X, Meng W, Liu X, Wang G, Bai Z, Wang Z, Yang F. Electrochemical performance and morphological evolution of hollow Sn microspheres. Solid State Ionics. 2018; 325:120−127.

[156] Wang ZD, Shan ZQ, Tian JH, Huang WL, Luo DD, Zhu X, Meng SX. Immersion-plated Cu_6Sn_5/Sn composite film anode for lithium ion battery. Journal of Materials Science. 2017; 52(10):6020–6033.

[157] Zhao KJ, Pharr M, Hartle L, Vlassak JJ, Suo ZG. Fracture and debonding in lithium-ion batteries with electrodes of hollow core-shell nanostructures. Journal of Power Sources. 2012; 218:6–14.

[158] Deshpande RD, Bernardi DM. Modeling solid-electrolyte interphase (SEI) fracture: coupled mechanical/chemical degradation of the lithium ion battery. Journal of the Electrochemical Society. 2017; 164(2):A461–A474.

[159] Luo F, Chu G, Xia XX, Liu B, Zheng JY, Li JJ, Li H, Gu CZ, Chen LQ. Thick solid electrolyte interphases grown on silicon nanocone anodes during slow cycling and their negative effects on the performance of Li-ion batteries. Nanoscale. 2015; 7(17):7651–7658.

[160] Nie MY, Chalasani D, Abraham DP, Chen YJ, Bose A, Lucht BL. Lithium ion battery graphite solid electrolyte interphase revealed by microscopy and spectroscopy. The Journal of Physical Chemistry C. 2013; 117(3):1257–1267.

[161] Szczech JR, Jin S. Nanostructured silicon for high capacity lithium battery anodes. Energy & Environmental Science. 2011; 4(1):56–72.

[162] Jung YS, Lee KT, Oh SM. Si-carbon core-shell composite anode in lithium secondary batteries. Electrochimica Acta. 2007; 52(24):7061–7067.

[163] Peled E, Menkin S. Review-SEI: past, present and future. Journal of the Electrochemical Society. 2017; 164(7):A1703–A1719.

[164] Liu XH, Fan FF, Yang H, Zhang SL, Huang JY, Zhu T. Self-limiting lithiation in silicon nanowires. ACS Nano. 2013; 7(2):1495–1503.

[165] Ichitsubo T, Yukitani S, Hirai K, Yagi S, Uda T, Matsubara E. Mechanical-energy influences to electrochemical phenomena in lithium-ion batteries. Journal of Materials Chemistry. 2011; 21(8):2701–2708.

[166] Zhang F, Wang JC, Liu SH, Du Y. Effects of the volume changes and elastic-strain energies on the phase transition in the Li–Sn battery. Journal of Power Sources. 2016; 330:111–119.

[167] Yang H, Liang WT, Guo X, Wang CM, Zhang SL. Strong kinetics-stress coupling in lithiation of Si and Ge anodes. Extreme Mechanics Letters. 2015; 2:1–6.

[168] Wang B, Luo B, Li X, Zhi L. The dimensionality of Sn anodes in Li-ion batteries. Materials Today. 2012; 15(12):544–552.

[169] Xu L, Kim C, Shukla AK, Dong A, Mattox TM, Milliron DJ, Cabana J. Monodisperse Sn nanocrystals as a platform for the study of mechanical damage during electrochemical reactions with Li. Nano Letters. 2013; 13(4):1800–1805.

[170] Guo YY, Zeng XQ, Zhang Y, Dai ZF, Fan HS, Huang Y, Zhang WN, Zhang H, Lu J, Huo F, Yan QY. Sn nanoparticles encapsulated in 3D nanoporous carbon derived from a metal-organic framework for anode material in lithium-ion batteries. ACS Applied Materials & Interfaces. 2017; 9(20):17172–17177.

[171] Yin LX, Chai SM, Wang FF, Huang JF, Li JY, Liu CQ, Kong XG. Ultrafine SnO_2 nanoparticles as a high performance anode material for lithium ion battery. Ceramics International. 2016; 42(8):9433–9437.

[172] Fang D, Li LC, Xu WL, Zheng HX, Xu J, Jiang M, Liu RN, Jiang XS, Luo ZP, Xiong CX, Wang Q. High capacity lithium ion battery anodes using Sn nanowires encapsulated Al_2O_3 tubes in carbon matrix. Advanced Materials Interfaces. 2016; 3(5):1500491.

[173] Zhao Y, Li XF, Yan B, Li DJ, Lawes S, Sun XL. Significant impact of 2D graphene nanosheets on large volume change tin-based anodes in lithium-ion batteries: a review. Journal of Power Sources. 2015; 274:869–884.

[174] Guan C, Wang XH, Zhang Q, Fan ZX, Zhang H, Fan HJ. Highly stable and reversible lithium storage in SnO_2 nanowires surface coated with a uniform hollow shell by atomic layer deposition. Nano Letters. 2014; 14(8):4852–4858.

[175] Liu CJ, Huang H, Cao GZ, Xue FH, Camacho RAP, Dong XL. Enhanced electrochemical stability of Sn-carbon nanotube nanocapsules as lithium-ion battery anode. Electrochimica Acta. 2014; 144:376–382.

[176] Luo B, Zhi L. Design and construction of three dimensional graphene-based composites for lithium ion battery applications. Energy & Environmental Science. 2015; 8(2):456–477.

[177] Luo B, Fang Y, Wang B, Zhou JS, Song HH, Zhi LJ. Two dimensional graphene-SnS_2 hybrids with superior rate capability for lithium ion storage. Energy & Environmental Science. 2012; 5(1):5226–5230.

[178] Du FH, Liu YS, Long J, Zhu QC, Wang KX, Wei X, Chen JS. Incorporation of heterostructured Sn/SnO nanoparticles in crumpled nitrogen-doped graphene nanosheets for application as anodes in lithium-ion batteries. Chemical Communications. 2014; 50(69):9961–9964.

[179] Li X, Dhanabalan A, Gu L, Wang C. Three-dimensional porous core-shell Sn@carbon composite anodes for high-performance lithium-ion battery applications. Advanced Energy Materials. 2012; 2(2):238–244.

[180] Ebner M, Marone F, Stampanoni M, Wood V. Visualization and quantification of electrochemical and mechanical degradation in Li ion batteries. Science. 2013; 342:716–720.

[181] Janish MT, Mackay DT, Liu Y, Jungjohann KL, Carter CB, Norton MG. TEM in situ lithiation of tin nanoneedles for battery applications. Journal of Materials Science. 2016; 51(1):589–602.

[182] Noh KW, Dillon SJ. Morphological changes in and around Sn electrodes during Li ion cycling characterized by in situ environmental TEM. Scripta Materialia. 2013; 69(9):658–661.

[183] Chao S-C, Song Y-F, Wang C-C, Sheu H-S, Wu H-C, Wu N-L. Study on microstructural deformation of working Sn and SnSb anode particles for Li-ion batteries by in situ transmission X-ray microscopy. The Journal of Physical Chemistry C. 2011; 115(44):22040–22047.

[184] Chao S-C, Yen Y-C, Song Y-F, Chen Y-M, Wu H-C, Wu N-L. A study on the interior microstructures of working Sn particle electrode of Li-ion batteries by in situ X-ray transmission microscopy. Electrochemistry Communications. 2010; 12(2):234–237.

[185] Beaulieu L, Beattie S, Hatchard T, Dahn J. The electrochemical reaction of lithium with tin studied by in situ AFM. Journal of the Electrochemical Society. 2003; 150(4):A419–A424.

[186] Chen C-H, Chason E, Guduru PR. Measurements of the phase and stress evolution during initial lithiation of Sn electrodes. Journal of the Electrochemical Society. 2017; 164(4):A574–A579.

[187] Gao X, Ma ZS, Jiang WJ, Zhang PP, Wang Y, Pan Y, Lu CS. Stress–strain relationships of $Li_x Sn$ alloys for lithium ion batteries. Journal of Power Sources. 2016; 311:21–28.

[188] Wang CP, Ma ZS, Wang Y, Lu CS. Failure prediction of high-capacity electrode materials in lithium-ion batteries. Journal of the Electrochemical Society. 2016; 163(7):A1157–A1163.

[189] Ma ZS, Wu H, Wang Y, Pan Y, Lu CS. An electrochemical-irradiated plasticity model for metallic electrodes in lithium-ion batteries. International Journal of Plasticity. 2017; 88:188–203.

[190] Meng YS, Arroyo-de Dompablo ME. First principles computational materials design for energy storage materials in lithium ion batteries. Energy & Environmental Science. 2009; 2(6):589–609.

[191] Ma ZS, Xie ZC, Wang Y, Zhang PP, Pan Y, Zhou YC, Lu CS. Failure modes of hollow core–shell structural active materials during the lithiation–delithiation process. Journal of Power Sources. 2015; 290:114–122.

[192] Lu B, Song YC, Zhang JQ. Time to delamination onset and critical size of patterned thin film electrodes of lithium ion batteries. Journal of Power Sources. 2015; 289:168–183.

[193] Lu B, Song YC, Guo ZS, Zhang JQ. Analysis of delamination in thin film electrodes under galvanostatic and potentiostatic operations with Li-ion diffusion from edge. Acta Mechanica Sinica. 2013; 29(3):348–356.

[194] Mayo M, Morris AJ. Structure prediction of Li–Sn and Li–Sb intermetallics for lithium-ion batteries anodes. Chemistry of Materials. 2017; 29(14):5787–5795.

[195] Sen R, Johari P. Understanding the lithiation of the Sn anode for high-performance Li-ion batteries with exploration of novel Li–Sn compounds at ambient and moderately high pressure. ACS Applied Materials & Interfaces. 2017; 9(46):40197–40206.

[196] Shi JJ, Shi WW, Jin W, Yin GQ. Diffusion of lithium in α-Sn and β-Sn as anode materials for lithium ion batteries. International Journal of Electrochemical Science. 2015; 10:4793–4800.

[197] Cheng YC. First-principles studies on ionic dynamic properties in lithium ion secondary batteries [dissertation on the internet]. Lanzhou (China): Lanzhou University; 2012 (in Chinese).

[198] Born M, Oppenheimer R. Zur quantentheorie der molekeln. Annalen Der Physik. 1927; 389(20):457–484.

[199] Hartree DR. The wave mechanics of an atom with a non-coulomb central field. part I. theory and methods. Mathematical Proceedings of the Cambridge Philosophical Society. 2008; 24(1):89–110.

[200] Fock V. Näherungsmethode zur Lösung des quantenmechanischen Mehrkörperproblems. Zeitschrift für Physik. 1930; 61(1–2):126–148.

[201] Thomas LH. The calculation of atomic fields. Mathematical Proceedings of the Cambridge Philosophical Society. 2008; 23(5):542–548.

[202] Fermi E. Application of statistical gas methods to electronic systems. Rendiconti dell'Accademia Nazionale dei Lincei. 1927; 6:602–607.

[203] Hohenberg P, Kohn W. Inhomogeneous electron gas. Physical Review. 1964; 136(3B):B864–B871.

[204] Kohn W, Sham L. Quantum density oscillations in an inhomogeneous electron gas. Physical Review. 1965; 137(6A):A1697–A1705.

[205] Slater JC. A simplification of the Hartree-Fock method. Physical Review. 1951; 81(3):385–390.

[206] Jones RO, Gunnarsson O. The density functional formalism, its applications and prospects. Reviews of Modern Physics. 1989; 61(3):689–746.

[207] Ceperley DM, Alder B. Ground state of the electron gas by a stochastic method. Physical Review Letters. 1980; 45(7):566–569.

[208] Vosko SH, Wilk L, Nusair M. Accurate spin-dependent electron liquid correlation energies for local spin density calculations: a critical analysis. Canadian Journal of Physics. 1980; 58(8):1200–1211.

[209] Perdew JP, Burke K, Ernzerhof M. Generalized gradient approximation made simple. Physical Review Letters. 1996; 77(7):3865–3868.

[210] Becke AD. Density-functional exchange-energy approximation with correct asymptotic behavior. Physical Review A. 1988; 38(6):3098–3100.

[211] Perdew JP. Unified theory of exchange and correlation beyond the local density approximation. Electronic Structure of Solids. 1991; 91:11–20.

[212] Perdew JP, Wang Y. Accurate and simple analytic representation of the electron-gas correlation energy. Physical Review B. 1992; 45(23):13244–13249.

[213] Perdew JP, Chevary JA, Vosko SH, Jackson KA, Pederson MR, Singh DJ, Fiolhais C. Atoms, molecules, solids, and surfaces: applications of the generalized gradient approximation for exchange and correlation. Physical Review B. 1992; 46(11):6671–6687.

[214] Hamann DR, Schlüter M, Chiang C. Norm-conserving pseudopotentials. Physical Review Letters. 1979; 43(20):1494–1497.

[215] Bachelet G, Hamann D, Schlüter M. Pseudopotentials that work: from H to Pu. Physical Review B. 1982; 26(8):4199–4228.

[216] Vanderbilt D. Soft self-consistent pseudopotentials in a generalized eigenvalue formalism. Physical Review B. 1990; 41(11):7892–7895.

[217] Bengone O, Alouani M, Blöchl P, Hugel J. Implementation of the projector augmented-wave LDA+U method: application to the electronic structure of NiO. Physical Review B. 2000; 62(24):16392–16401.

[218] Kresse G, Hafner J. Ab initio molecular dynamics for liquid metals. Physical Review B. 1993; 47(1):558–561.

[219] Kresse G, Furthmüller J. Efficient iterative schemes for ab initio total-energy calculations using a plane-wave basis set. Physical Review B. 1996; 54(16):11169–11186.

[220] Monkhorst HJ, Pack JD. Special points for Brillouin-zone integrations. Physical Review B. 1976; 13(12):5188–5192.

[221] Chung DH, Buessem WR. The Voigt-Reuss-Hill (VRH) approximation and the elastic moduli of polycrystalline ZnO, TiO_2 (Rutile), and α-Al_2O_3. Journal of Applied Physics. 1968; 39(6):2777–2782.

[222] Hill R. The elastic behaviour of a crystalline aggregate. Proceedings of the Physical Society Section A. 1952; 65(5):349–354.

[223] Brenner SS. Tensile strength of whiskers. Journal of Applied Physics. 1956; 27(12):1484–1491.

[224] Brenner S. Plastic deformation of copper and silver whiskers. Journal of Applied Physics. 1957; 28(9):1023−1026.

[225] Qi Y, Hector Jr LG. Adhesion and adhesive transfer at aluminum/diamond interfaces: a first-principles study. Physical Review B. 2004; 69(23):235401.

[226] Maxisch T, Ceder G. Elastic properties of olivine Li_xFePO_4 from first principles. Physical Review B. 2006; 73(17):174112.

[227] Barrett CS, Massalski TB. Structure of metals: McGraw-Hill Book Company, Inc.; New York; 1966.

[228] Hansen DA, Chang LJ. Crystal structure of Li_2Sn_5. Acta Crystallographica Section B. 1969; 25(11):2392–2395.

[229] Muller W, Schafer H. The crystal structure of LiSn. Zeitschrift für Naturforschung B. 1973; 28:246–248.

[230] Müller W. Preparation and crystal structure of Li_7Sn_3. Zeitschrift für Naturforschung B. 1974; 29(5–6):304–311.

[231] Frank U, Müller W, Schäfer H. The crystal structure of Li_5Sn_2. Zeitschrift für Naturforschung B. 1975; 30(1–2):1–5.

[232] Frank U, Müller W. The preparation and crystal structure of $Li_{13}Sn_5$ and the structural relations between the phases of the systems Li–Sn and Li–Pb. Zeitschrift für Naturforschung B. 1975; 30(5–6):316–322.

[233] Frank U, Müller W, Schäfer H. The crystal structure of Li_7Sn_2. Zeitschrift für Naturforschung B. 1975; 30(1–2):6–9.

[234] Lupu C, Mao J-G, Rabalais JW, Guloy AM, Richardson JW. X-ray and neutron diffraction studies on "$Li_{4.4}Sn$". Inorganic Chemistry. 2003; 42(12):3765–3771.

[235] Gersten JI, Smith FW. The physics and chemistry of materials: Wiley New York; 2001.

[236] Tian DC, Wang XB. Electronic structure and equation of state of TiB_2. Journal of Physics: Condensed Matter. 1992; 4:8765–8772.

[237] Ravindran P, Subramoniam G, Asokamani R. Ground-state properties and relative stability between the $L1_2$ and DO_a phases of Ni_3Al by Nb substitution. Physical Review B. 1996; 53(3):1129–1137.

[238] Henkelman G, Arnaldsson A, Jónsson H. A fast and robust algorithm for Bader decomposition of charge density. Computational Materials Science. 2006; 36(3):354–360.

[239] Savin A, Jepsen O, Flad J, Andersen OK, Preuss H, von Schnering HG. Electron localization in solid-state structures of the elements: the diamond structure. Angewandte Chemie International Edition. 1992; 31(2):187–188.

[240] Zhang PP, Ma ZS, Wang Y, Zou YL, Lei WX, Pan Y, Lu CS. A first principles study of the mechanical properties of Li–Sn alloys. RSC Advances. 2015; 5(45):36022–36029.

[241] Gale WF, Totemeier TC. Smithells metals reference book: Butterworth-Heinemann; 2003.

[242] Mouhat F, Coudert F-X. Necessary and sufficient elastic stability conditions in various crystal systems. Physical Review B. 2014; 90(22):224104.

[243] Chen J, Bull S, Roy S, Mukaibo H, Nara H, Momma T, Osaka T, Shacham-Diamand Y. Mechanical analysis and in situ structural and morphological evaluation of Ni–Sn alloy anodes for Li ion batteries. Journal of Physics D: Applied Physics. 2008; 41(2):025302.

[244] Li KY, Xie H, Liu J, Ma ZS, Zhou YC, Xue DF. From chemistry to mechanics: bulk modulus evolution of Li–Si and Li–Sn alloys via the metallic electronegativity scale. Physical Chemistry Chemical Physics. 2013; 15(40):17658–17663.

[245] Hao YL, Li SJ, Sun BB, Sui ML, Yang R. Ductile titanium alloy with low Poisson's ratio. Physical Review Letters. 2007; 98(21):216405.

[246] Pugh S. XCII. Relations between the elastic moduli and the plastic properties of polycrystalline pure metals. Philosophical Magazine. 1954; 45(367):823–843.

[247] Ranganathan S, Ostoja-Starzewski M. Universal elastic anisotropy index. Physical Review Letters. 2008; 101(5):055504.

[248] Zhou XW, Li TY, Cui Y, Fu YZ, Liu YZ, Zhu LK. In situ focused ion beam scanning electron microscope study of microstructural evolution of single tin particle anode for Li-ion batteries. ACS Applied Materials & Interfaces. 2019; 11:1733–1738.

[249] Miao NH, Sa BS, Zhou J, Sun ZM. Theoretical investigation on the transition-metal borides with Ta_3B_4-type structure: a class of hard and refractory materials. Computational Materials Science. 2011; 50:1559–1566.

[250] Verbrugge MW, Baker DR, Xiao XC, Zhang QL, Cheng Y-T. Experimental and theoretical characterization of electrode materials that undergo large volume changes and application to the lithium–silicon system. The Journal of Physical Chemistry C. 2015; 119(10):5341–5349.

[251] Maranchi JP, Hepp AF, Evans AG, Nuhfer NT, Kumta PN. Interfacial properties of the *a*-Si/Cu: active-inactive thin-film anode system for lithium-ion batteries. Journal of the Electrochemical Society. 2006; 153(6):A1246–A1253.

[252] Genser O, Hafner J. Structure and bonding in crystalline and molten Li–Sn alloys: a first-principles density-functional study. Physical Review B. 2001; 63(14):144204.

[253] Zhang PP, Ma ZS, Jiang WJ, Wang Y, Pan Y, Lu CS. Mechanical properties of Li–Sn alloys for Li-ion battery anodes: a first-principles perspective. AIP Advances. 2016; 6(1):015107.

[254] Shi JJ, Wang ZG, Fu YQ. Density functional theory study of diffusion of lithium in Li–Sn alloys. Journal of Materials Science. 2016; 51(6):3271–3276.

[255] Straumanis M, Yu L. Lattice parameters, densities, expansion coefficients and perfection of structure of Cu and of Cu–In α phase. Acta Crystallographica Section A. 1969; 25(6):676–682.

[256] Neugebauer J, Scheffler M. Adsorbate-substrate and adsorbate-adsorbate interactions of Na and K adlayers on Al(111). Physical Review B. 1992; 46(24):16067–16080.

[257] Boer FRD, Mattens WCM, Boom R, Miedema AR, Niessen AK. Cohesion in metals. Netherlands: North-Holland; 1988.

[258] Wang H, Hou B, Wang X, Xia S, Chew HB. Atomic-scale mechanisms of sliding along an interdiffused Li–Si–Cu interface. Nano Letters. 2015; 15:1716–1721.

[259] Kim MG, Sim S, Cho J. Novel core-shell Sn–Cu anodes for lithium rechargeable batteries prepared by a redox-transmetalation reaction. Advanced Materials. 2010; 22(45):5154–5158.

[260] Jelver L, Larsen PM, Stradi D, Stokbro K, Jacobsen KW. Determination of low-strain interfaces via geometric matching. Physical Review B. 2017; 96(8):085306.

[261] Chou C-Y, Hwang GS. Role of interface in the lithiation of silicon-graphene composites: a first principles study. The Journal of Physical Chemistry C. 2013; 117(19):9598–9604.

[262] Deng X, Chawla N, Chawla K, Koopman M. Deformation behavior of (Cu, Ag)–Sn intermetallics by nanoindentation. Acta Materialia. 2004; 52(14):4291–4303.

[263] Tamura N, Ohshita R, Fujimoto M, Fujitani S, Kamino M, Yonezu I. Study on the anode behavior of Sn and Sn–Cu alloy thin-film electrodes. Journal of Power Sources. 2002; 107(1):48–55.

[264] Xue LG, Fu ZH, Yao Y, Huang T, Yu AS. Three-dimensional porous Sn–Cu alloy anode for lithium-ion batteries. Electrochimica Acta. 2010; 55(24):7310–7314.

[265] Xing YL, Wang SB, Fang BZ, Feng YF, Zhang SC. Three-dimensional nanoporous Cu_6Sn_5/Cu composite from dealloying as anode for lithium ion batteries. Microporous and Mesoporous Materials. 2018; 261:237–243.

[266] Shen Z, Hu Y, Chen RZ, He X, Chen YL, Shao HF, Zhang XW, Wu KS. Split Sn–Cu alloys on carbon nanofibers by one-step heat treatment for long-lifespan lithium-ion batteries. Electrochimica Acta. 2017; 225:350–357.

[267] Polat DB, Lu J, Abouimrane A, Keles O, Amine K. Nanocolumnar structured porous Cu–Sn thin film as anode material for lithium-ion batteries. ACS Applied Materials & Interfaces. 2014; 6(14):10877–10885.

[268] Larcher D, Beaulieu L, MacNeil D, Dahn J. In situ X-ray study of the electrochemical reaction of Li with η'-Cu_6Sn_5. Journal of the Electrochemical Society. 2000; 147(5):1658–1662.

[269] Li L, Liu X, Wang S, Zhao W. Influence of surface structure on the capacity and irreversible capacity loss of Sn-based anodes for lithium ion batteries. ACS Sustainable Chemistry & Engineering. 2014; 2(7):1857–1863.

[270] Wang K-K, Gan D, Hsieh K-C. The orientation relationships of the Cu_3Sn/Cu interfaces and a discussion of the formation sequence of Cu_3Sn and Cu_6Sn_5. Thin Solid Films. 2014; 562:398–404.

[271] Wang K-K, Gan D, Hsieh K-C, Chiou S-Y. The microstructure of η'-Cu_6Sn_5 and its orientation relationships with Cu in the early stage of growth. Thin Solid Films. 2010; 518(6):1667–1674.

[272] Lee NTS, Tan VBC, Lim KM. First-principles calculations of structural and mechanical properties of Cu_6Sn_5. Applied Physics Letters. 2006; 88(3):031913.

[273] Watanabe Y, Fujinaga Y, Iwasaki H. Lattice modulation in the long-period superstructure of Cu_3Sn. Acta Crystallographica Section B. 1983; 39(3):306–311.

[274] Vaughey JT, Kepler KD, Benedek R, Thackeray MM. NiAs-versus zinc-blende-type intermetallic insertion electrodes for lithium batteries: lithium extraction from Li_2CuSn. Electrochemistry Communications. 1999; 1(11):517–521.

[275] Pang XY, Liu ZQ, Wang SQ, Shang JK. Effects of Bi segregation on the tensile properties of Cu/Cu$_3$Sn(100) interface. Microelectronics Reliability. 2011; 51(12):2330–2335.

[276] Zhang PP, Ma ZS, Wang Y, Zou YL, Sun LZ, Lu CS. Lithiation-induced interfacial failure of electrode-collector: a first-principles study. Materials Chemistry and Physics. 2019; 222:193–199.

[277] Wei Y, Hutchinson JW. Toughness of Ni/Al$_2$O$_3$ interfaces as dependent on micron-scale plasticity and atomistic-scale separation. Philosophical Magazine. 2008; 88(30–32):3841–3859.

[278] Pu WH, He XM, Ren JG, Wan CR, Jiang CY. Electrodeposition of Sn–Cu alloy anodes for lithium batteries. Electrochimica Acta. 2005; 50(20):4140–4145.

[279] Mammen N, Narasimhan S, de Gironcoli S. Tuning the morphology of gold clusters by substrate doping. Journal of the American Chemical Society. 2011; 133(9):2801–2803.

[280] Shao X, Prada S, Giordano L, Pacchioni G, Nilius N, Freund HJ. Tailoring the shape of metal Ad-particles by doping the oxide support. Angewandte Chemie International Edition. 2011; 50(48):11525–11527.

[281] Dai JH, Song Y, Yang R. Influence of alloying elements on stability and adhesion ability of TiAl/TiO$_2$ interface by first-principles calculations. Intermetallics. 2017; 85:80–89.

[282] Li WJ, Shao WZ, Chen Q, Zhang L, Han Y, Chen BA, Wang Q, Zhen L. Effects of dopants on the adhesion and electronic structure of a SnO$_2$/Cu interface: a first-principles study. Physical Chemistry Chemical Physics. 2018; 20(23):15618–15625.

[283] Fu Q, Colmenares Rausseo LC, Martinez U, Dahl PI, García Lastra JM, Vullum PE, Svenum I-H, Vegge T. Effect of Sb segregation on conductance and catalytic activity at Pt/Sb-doped SnO$_2$ interface: a synergetic computational and experimental study. ACS Applied Materials & Interfaces. 2015; 7(50):27782–27795.

[284] Lübke M, Ning D, Armer CF, Howard D, Brett DJL, Liu ZL, Darr JA. Evaluating the potential benefits of metal ion doping in SnO_2 negative electrodes for lithium ion batteries. Electrochimica Acta. 2017; 242:400–407.

[285] Ma YJ, Ma Y, Ulissi U, Ji YC, Streb C, Bresser D, Passerini S. Influence of the doping ratio and the carbon coating content on the electrochemical performance of Co-doped SnO_2 for lithium-ion anodes. Electrochimica Acta. 2018; 277:100–109.

[286] Guo H, Zhao H, Jia X, Li X, Qiu W. A novel micro-spherical $CoSn_2$/Sn alloy composite as high capacity anode materials for Li-ion rechargeable batteries. Electrochimica Acta. 2007; 52(14):4853–4857.

[287] Ke FS, Huang L, Wei HB, Cai JS, Fan XY, Yang FZ, Sun SG. Fabrication and properties of macroporous tin–cobalt alloy film electrodes for lithium-ion batteries. Journal of Power Sources. 2007; 170(2):450–455.

[288] He JC, Zhao HL, Wang J, Wang J, Chen JB. Hydrothermal synthesis and electrochemical properties of nano-sized Co–Sn alloy anodes for lithium ion batteries. Journal of Alloys and Compounds. 2010; 508(2):629–635.

[289] Groult H, El Ghallali H, Barhoun A, Briot E, Julien CM, Lantelme F, Borensztjan S. Study of Co–Sn and Ni–Sn alloys prepared in molten chlorides and used as negative electrode in rechargeable lithium battery. Electrochimica Acta. 2011; 56(6):2656–2664.

[290] Gul H, Uysal M, Çetinkaya T, Guler MO, Alp A, Akbulut H. Preparation of Sn–Co alloy electrode for lithium ion batteries by pulse electrodeposition. International Journal of Hydrogen Energy. 2014; 39(36):21414–21419.

[291] Deringer VL, Tchougréeff AL, Dronskowski R. Crystal orbital hamilton population (COHP) analysis as projected from plane-wave basis sets. The Journal of Physical Chemistry A. 2011; 115(21):5461–5466.

[292] Maintz S, Deringer VL, Tchougréeff AL, Dronskowski R. LOBSTER: a tool to extract chemical bonding from plane-wave based DFT. Journal of Computational Chemistry. 2016; 37(11):1030–1035.
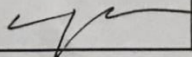
[293] Maintz S, Deringer VL, Tchougréeff AL, Dronskowski R. Analytic projection from plane-wave and PAW wavefunctions and application to chemical-bonding analysis in solids. Journal of Computational Chemistry. 2013; 34(29):2557–2567.

[294] Hao F, Fang DN. Reducing diffusion-induced stresses of electrode–collector bilayer in lithium-ion battery by pre-strain. Journal of Power Sources. 2013; 242:415–420.

[295] Yang FQ. Criterion for insertion-induced microcracking and debonding of thin films. Journal of Power Sources. 2011; 196(1):465–469.

[296] Jangid MK, Sonia FJ, Kali R, Ananthoju B, Mukhopadhyay A. Insights into the effects of multi-layered graphene as buffer/interlayer for a-Si during lithiation/delithiation. Carbon. 2017; 111:602–616.

[297] Basu S, Suresh S, Ghatak K, Bartolucci SF, Gupta T, Hundekar P, Kumar R, Lu T-M, Datta D, Shi Y. Utilizing van der waals slippery interfaces to enhance the electrochemical stability of silicon film anodes in lithium-ion batteries. ACS Applied Materials & Interfaces. 2018; 10(16):13442–13451.

Appendix

Appendix A: Contributions of author

[1] **Zhang PP**, Ma ZS, Wang Y, Zou YL, Lei WX, Pan Y, and Lu CS. A first principles study of the mechanical properties of Li–Sn alloys. RSC Advances. 2015;5(45):36022–36029.

Author	Conception & design	Modelling, simulations & data acquisition	Data processing & analysis	Interpretation & discussion	Manuscript writing, revision and finalisation	Final approval	Signature
Zhang PP	×	×	×	×	×	×	Zhang PP
Ma ZS	×		×	×	×	×	Ma ZS
Wang Y				×	×	×	Wang Yan
Zou YL				×		×	zou YL
Lei WX				×		×	Lei weixin
Pan Y				×		×	Pan Yong
Lu CS	×		×	×	×	×	

I acknowledge that these represent my contribution to the above result output

[2] **Zhang PP**, Ma ZS, Jiang WJ, Wang Y, Pan Y., Lu CS. Mechanical properties of Li−Sn alloys for Li-ion battery anodes: a first-principles perspective, AIP Advances. 2016;6:01510.

			I acknowledge that these represent my contribution to the above result output				
Authors	Conception & design	Modeling, simulations & data acquisition	Data processing & analysis	Interpretation & discussion	Manuscript writing, revision & finalisation	Final approval	Sign
Zhang PP	×	×	×	×	×	×	Zhang PP
Ma ZS	×		×	×	×	×	Ma ZS
Jiang WJ				×	×	×	Jiang WJ
Wang Y				×		×	Wang Y
Pan Y				×		×	Pan Yong
Lu CS	×		×	×	×	×	

[3]   **Zhang PP**, Ma ZS, Wang Y, Zou YL, Sun LZ, Lu CS. Lithiation-induced interfacial failure of electrode-collector: a first-principles study. Materials Chemistry and Physics. 2018;222:193–199.

I acknowledge that these represent my contribution to the above result output							
Author	Conception & design	Modelling, simulations & data acquisition	Data processing & analysis	Interpretation & discussion	Manuscript writing, revision & finalisation	Final approval	Signature
Zhang PP	×	×	×	×	×	×	_zhang PP_
Ma ZS	×		×	×	×	×	_Ma ZS_
Wang Y				×	×	×	_Wang Yan_
Zou YL				×		×	_zou YL_
Sun LZ				×		×	_L. Z Sun_
Lu CS	×		×	×	×	×	_(signature)_

[4] **Zhang PP**, Wang Y, Lei WX, Zou YL, Jiang WJ, Ma ZS, Lu CS. Enhancement effects of Co doping on interface properties of Sn electrode-collector: a first-principles study, ACS Applied Materials & Interfaces. 2019, accepted.

	I acknowledge that these represent my contribution to the above result output						
Author	Conception & design	Modelling, simulations & data acquisition	Data processing & analysis	Interpretation & discussion	Manuscript writing, revision & finalisation	Final approval	Signature
Zhang PP	×	×	×	×	×	×	Zhang PP
Wang Y			×	×	×	×	Wang Yan
Lei WX				×	×	×	Lei weixin
Zou YL				×		×	Zou YL
Jiang WJ				×		×	Jiang WJ
Ma ZS	×		×	×	×	×	Ma Zs
Lu CS	×		×	×	×	×	